ENERGY REDUCTION IN PUMPING LOW CONSISTENCY PULP FIBER SUSPENSIONS

by

Mazyar Jalayer

B.A.Sc, The University of British Columbia, 2007

A THESIS SUBMITTED IN PARTIAL FULFILLMENT OF
THE REQUIREMENTS FOR THE DEGREE OF

MASTER OF APPLIED SCIENCE

in

THE FACULTY OF GRADUATE STUDIES

(Mechanical Engineering)

THE UNIVERSITY OF BRITISH COLUMBIA
(Vancouver)

December 2011

Abstract

Liquid transport is a vital segment of the economy. Pumping systems – whether used at a pulp and paper mill to transfer pulp stock, to pump petroleum through cross country pipeline or to transport tailings from a mine processing plant to a disposal site – are often one of the largest consumers of electrical energy. This thesis studies energy reduction in pumping low consistency fibre suspensions. The methods and procedures described in this work are applicable to any process where pumps are utilized. The main focus is on centrifugal pumps, the most commonly used pump at processing plants. Two methods are developed to achieve energy reduction: redesign of the original equipment manufacturer (OEM) impeller and pump performance monitoring via thermodynamic method.

A novel methodology/process was developed for redesigning a more efficient impeller for existing pump installations. A computational fluid dynamics (CFD) process was developed for performance prediction of various impeller designs. The CFD process was validated using experimental pump loop results. Using OEM impeller geometry, design data and the redesign model, a series of eight optimal impellers were generated. The performances of these impellers were evaluated using the validated CFD process. The most efficient impeller design was selected for prototyping and experimental validation. A case study on Allis Chalmers PWO 6”x3”x14” pump showed that efficiency increase of 19.7% can be achieved with the redesign methodology.

The validity of thermodynamic method was also studied in low consistency fibre suspension service. Head and efficiency curves for a low consistency pulp and paper centrifugal pump were measured for various low consistency pulp suspensions (0.5%, 1.0%, and 1.5%). These curves were simultaneously determined using two different approaches: conventional magnetic flow meter and differential pressure measurements; and by utilizing suction and discharge static pressure and temperature data (the thermodynamic method). It is found that addition of up to 1.5% mass fraction of softwood Kraft pulp to water did not affect the accuracy of the efficiency measurement when using the thermodynamic method. The pump efficiency calculated by thermodynamic method is consistent with the “gold standard” flow-meter-based method for flow rates within 90 – 115% of BEP (±1.0% maximum discrepancy).

Preface

The work in Chapter 7.1: Redesign Model for the OEM Impeller is based on formulation and parameterization models which can be found in Chapter 3.3.2 of The Interaction between Geometry and Performance of a Centrifugal Pump, B Neumann, London: Mechanical Engineering Publications Limited, 1991, p 87 – 129 [**1**].

All experimental tests are conducted at University of British Columbia, Pulp and Paper Center pump loop and on an Allis Chalmers PWO 6”x3”x14” Pump with wear plate clrearance set at 0.020”.

The work in Chapter 8 is based on collaboration between Pulp and Paper Center and ATAP Infrastructure Management Inc. ATAP has the exclusive license to provide Yatesmeter pump performance testing in Western Canada.

Table of Contents

List of Tables

List of Figures

List of Acronyms

ABS	Acrylonitrile Butadiene Styrene
API	American Petroleum Institute
BC	Boundary Condition
BEP	Best Efficiently Point
CAD	Computer Aided Design
CFD	Computational Fluid Dynamics
DNS	Direct Numerical Simulation
FE	Flow Element
FEM	Fusion Deposition Modeling
LE	Leading Edge
MOV	Motor Operated Valve
NSERC	Natural Sciences and Engineering Research Council of Canada
OEM	Original Equipment Manufacture
PC	Polycarbonate
POM	Power Meter
POV	Pump out Vane
PPSF	Polyphenylsulfone
PS	Pressure Side
PT	Pressure Sensor
RANS	Reynolds-Averaged Navier-Stokes
RPM	Revolution per Minute
SS	Suction Side
TE	Trailing Edge
TT	Temperature Sensor
ULTEM	Polyetherimide
VFD	Variable Frequency Drive

Nomenclature

Unfortunately in the world of design and analysis of roto-dynamic pumps there is no commonly acceptable nomenclature. The nomenclature outlined here is constructed from various sources and standards as to the most accepted terms. The extensive list of symbols and nomenclatures are defined in this section.

Primary symbols:

a/a_o	Cascade Correction Factor
A_2	Passage Area at Outlet
A_o	Impeller Eye Area
A_x	Variable Area of Impeller Passage
b_1	Blade Width at Inlet
b_2	Blade Width at Outlet
C	True 3D Distance Along Camber Line
c	Absolute Velocity
C_D	Drag Coefficient
C_L	Lift Coefficient
C_{LA}	Hydrodynamic Pressure Coefficient
C_{LC}	Centrifugal Pressure Coefficient
c_{m1}	Meridional Component of Absolute Velocity At LE
c_{m2}	Meridional Component of Absolute Velocity At TE
$Const$	Constant Value/Number
C_{pf}	Heat Capacity of Cellulose Wood Fibre
c_{u1}	Circumferential Component of Absolute Velocity at LE
c_{u2}	Circumferential Component of Absolute Velocity at TE
D_1	Impeller Diameter at Inlet
D_2	Impeller Diameter at Outlet
D_h	Hub Diameter
D_H	Hydraulic Diameter

D_m	Mean Diameter of Impeller Vane at Inlet
D_o	Impeller Eye Diameter
D_x	Variable Diameter of a Point on a Streamline
ε	Surface Roughness Coefficient
EL	Elevation
F	Force
$f(\ldots)$	Function of …
Ft	Unit Feet
g	Gravity Constant
gpm	Unit US Gallon Per Minute
h	Enthalpy
H	Head
H_{loss}	Head Loss
h_o	Length of Streamline Projection on The Axial-Radial Plane
i'	Difference Between The True Flow Angle And Blade Angle
ID	Pipe Inside Diameter
L, l	Length
$l_{\phi r}$	Fractional Length of The Blade on The Φ-R Plane
l_{true}	Actual Blade Length
M	Distance Along Meridional Curve
M	Moment
M'	Radius Normalized Distance Along Meridional Curve
$M_{1\text{-}2}$	Blade Length Projected on The Meridional Streamline
n	Normal Vector
n	Rotational Speed
η	Efficiency
N_s	Pump's Specific Speed
P	Pressure

P	Power
P_c	Location of Maximum Camber Length
Q	Flow Rate
R	Radius or Radial Location
r	Radius or Hub/Tip Ratio
Re	Reynolds Number
R_{MS}	Radius of Curvature of The Mean Streamline
rpm	Unit Revolution Per Minute
R_T	Peripheral Section Radius of Curvature
s	Fractional Distance Along a Curve (0 To 1), Entropy
S_{xy}	Standard Error of The Fit
t_1	Thickness At LE
t_2	Thickness At TE
t_m	Blade Pitch
t_p	Student T Distribution
t_s	Maximum Camber
u	Peripheral or Circumferential Velocity or Velocity In X-Direction
U	Uncertainty
$\bar{u}$	Average Velocity in x-Direction
u'	Turbulence Velocity Fluctuation in x-Direction
v	Velocity or Velocity In y-Direction
V	Average Velocity in a Pipe
w	Relative Velocity or Velocity in z-Direction
w_{u1}	Circumferential Component of Relative Velocity at LE
w_{u1}	Circumferential Component of Relative Velocity at TE
X	X-Axis Distance
x	Ratio of The Mean Streamline Inlet Area to Impeller Outlet Diameter, or Fibre Mass Concentration

Y	Y-Axis Distance
$y(x)$	Curve Fit Function
$y+$	Dimensionless Distance from The Wall
Z	Axial Location
z	Number of Blades/Vanes
α	Angle Between Direction of Peripheral and Absolute Velocity
α_D	Diffusion Angle
α_T	Corrected Angle of Attack
β	Axial Blade Angle
β'	Flow Velocity
β_{CH}	Blade Chord Angle
β'_1	Flow Velocity at LE
β_{1B}	Tangential Blade Angle at LE
β_{1Ba}	Axial Blade Angle at LE
β'_2	Flow Velocity at TE
β_{2B}	Tangential Blade Angle at TE
β_{2Ba}	Axial Blade Angle at TE
γ	Slip Factor
ΔH	Differential Head
θ_x	Variable Angular Position of EL
ν	Kinematic Viscosity
ξ	Blockage Factor
ρ	Density
σ	Solidity, Standard Deviation
ϕ	Flow Coefficient
φ	Blade Wrap Angle or The Rotation Around Z Axis from X Axis Towards Y Axis
ψ	Head Coefficient
ω	Angular Speed

ω_s	True Dimensionless Specific Speed

Subscripts:

1	Inlet or LE
2	Outlet or TE
2i	Constant Entropy Based on Inlet Entropy
∞	Average
avg	Average
B	Blade
CH	Cord
d	Dynamic
DH	Hydraulic Diameter
disk	Disk
drag	Drag
f	Friction
fitt	Curve Fit
h	Hydraulic
imp	Impeller
loss	Losses
m	Meridional Component
max	Maximum
mech	Mechanical
min	Minimum
n	Normal Component
net	Net or Average
o	Isolated
OEM	Original Equipment Manufacture Impeller
opt	Optimal

p	Static
pump	Pump
Red	Redesign Impeller
R-θ	On R-θ Plane
shaft	Shaft
th	Theoretical
thermo	Thermodynamic Method
tot	Total
vol	Volume
w	Wake
x	X-Component
y	Y-Component
z	Z-Component
τ	Shear Stress

Acknowledgements

I would like to thank my family and friends for their love and support. I would also like to express my appreciation to my supervisors Dr. James Olson, Dr. Sheldon I. Green and Dr. Mark Martinez for their guidance and support on this thesis. I also would like to thank my colleagues and the staff at the Pulp and Paper Centre for their support especially George Soong for supporting me on the experiential trials.

Special thanks to Imad Abuyousef of ATAP Infrastructure Management Inc., for his assistance on the Yatesmeter testing.

This work is funded by the Natural Sciences and Engineering Research Council of Canada through the Collaborative Research and Development program and through the support of our partners: BC Hydro, Paprican, Catalyst Papers, Howe Sound Pulp and Paper, West Fraser Quesnel River Pulp, Canfor, Andritz, Arkema, Honeywell, WestCan Engineering, Advanced Fiber Technologies, Ontario Power Authority, CEATI international and ATAP Infrastructure Management. I would like to thank all of them for providing funding for this research.

Chapter 1: Introduction

Pumps are used widely in many industries to transfer process fluids from one point to another. Most processes in plants rely upon pumping systems for their daily operation. In the pulp and paper industry, pumps represent 31% [**2**] of the electricity used by the process. For this reason pumping systems are often one of the largest consumers of electrical energy at many plants. Increase in demand for energy intensive commodities is taxing on world's energy supply and our environment. The motivation in this study is to find ways to reduce equipment energy consumption.

Pumps can be classified by two types: positive displacement pumps and rotodynamic pumps. Positive displacement pumps displace the fluid directly by a mechanical action. However in centrifugal pumps, which are also known as rotodynamic pumps, kinetic energy is converted to pressure which conveys the fluid. Rotodynamic pumps can be sub-categorized into three types: axial, radial and mixed-flow. Many factors determine the types of pumps used in a particular application. This work is funded through partnership with BC Hydro and a consortium of pulp and paper companies. The primary focus is on energy reduction in pumping of low consistency fibre suspensions. For this reason the type of pump under study will be the radial centrifugal type. This type of pump accounts for the majority of pumps utilized by the industry [**3**]. The work herein is not just limited to pulp and paper industry but it is also applicable anywhere radial centrifugal pumps are utilized such as:

- Oil and gas plants
- Chemical processing plants
- Mining and mineral

There are two parts to this work: one is energy reduction by redesigning the original equipment manufacturer (OEM) impeller and the other is by performance monitoring. The redesign of the OEM impeller involves designing an impeller with higher efficiency for plant's current process conditions. Often an engineer sizes a pump based on conservative assumptions. During the sizing of the pump the vendor may apply a conservative safety factor for sizing. The plants process requirement may also change over a period of time as production varies. In any case, the installed pump maybe oversized or undersized for the

process conditions and it may not operate at its best efficiency point (BEP). The motivation in this is work is to replace existing installations with new and more efficient impellers which satisfy current process conditions. Existing, worn impellers can be replaced with more efficient impellers at a fraction of high-operating cost of low-performing OEM impeller.
By analyzing pump's performance, adjustments can be made to pump's operation and process conditions to reduce power consumption and optimize pump's performance. This is the motivation for the second part of this work, pump performance monitoring. In this part a relatively novel technique called the thermodynamic method is used to measure pumps performance. The thermodynamic method has been studied in great detail. This work will explore the application of the thermodynamic method to pumping of low consistency pulp suspensions.

1.1 Case Study: Allis Chalmers PWO Pump

All work in this study is performed on the Allis Chalmers PWO Pump. Figure 1.1 shows a picture of this pump, which is equipped with 14" open radial centrifugal impeller that has 2 vanes. The pump has a 6" suction and a 3" discharge nozzle. It is a fairly small size pump when compared with industry average. However, this size pump represents the average small size pumps used in the pulp and paper industry where the process fluid has a pulp consistency of up to 1.5%. The PWO pump has a low peak performance of about 59%. It is a very popular line of pump and has a track record of numerous installations at plants throughout North America. For this reason this pump is an ideal candidate for studying of energy reduction in low consistence pulp service.

1.2 Redesign of OEM Impeller

The work flow for the redesigned impeller is shown in Figure 1.2. Using laser scan data, the geometrical parameters is extracted from the impeller and a 3D parametric impeller model is built in CAD. The geometry of the impeller is discussed in more detail in Chapter 2.3. Using the 3D OEM impeller model and experimental data a CFD (Computational Fluid Dynamic) process is validated for performance prediction. Numerical calculation for performance prediction of the impeller is covered in Chapter 4.2. Using a redesign model, which will be the subject of Chapter 7.1, a series of optimal impeller designs are generated based on OEM

impeller hub and shroud profiles. These models are based on theoretical and empirical pump design formulas which are highlighted in Chapter 3. The series of optimal impeller designs are then evaluated using the validated CFD process and the most efficient impeller is selected for prototyped. The impeller design is then validated experimentally.

Figure 1.1: Allis Chalmers PWO Pump, 6”x3”x14” Paper and Pulp Process Pump

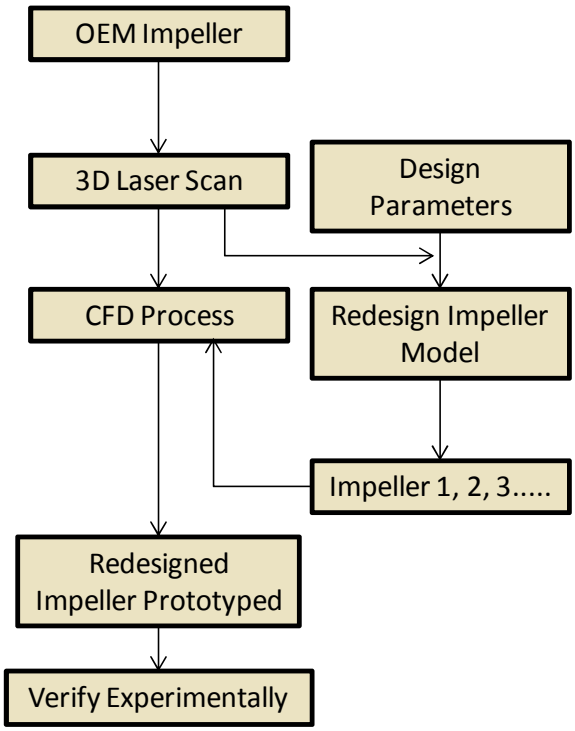

Figure 1.2: Redesign Work Flow Diagram

1.3 Literature Survey

The geometry of centrifugal impeller is studied in great detail in references [**1**], [**4**], [**5**], [**6**], [**7**] and [**8**]. Parameterization and specialized coordinate systems which are used to define turbomachinery components is best described in reference [**9**]. Pump hydraulics and fluid flow behaviors inside the pump is described in several books [**1**], [**8**], [**10**] and [**11**]. CFD calculation is discussed in several sources [**5**], [**12**], [**13**], [**14**], [**15**], [**16**], [**17**], [**18**], [**19**], and [**20**]. Two types calculation are utilized by these sources: component and stage calculation. The effect of turbulence model on accuracy of CFD performance prediction is evaluated by several sources, [**4**] and [**21**]. Preprocessing techniques and boundary condition (BC) types are described by Gülich [**8**].

Turbomachinery efficiency calculation from suction and discharge pressure and temperature data was first employed by Poirson [**22**] in 1914, where he tested the thermodynamic method on a water turbine. Since then, there have been numerous studies done on the accuracy of this method [**23**], [**24**] and [**25**].Merry and Thew [**26**] applied the thermodynamic method to an overhanging centrifugal pump. Routley [**27**] studied the thermodynamic method and its accuracy. The author of this work is unaware of any prior work regarding the application of the thermodynamic method to pumping of low consistency pulp suspension.

Chapter 2: Centrifugal Impeller Geometry

This chapter demonstrates the complex shape and geometry of centrifugal impeller. Specialized coordinate systems which are used to define turbomachinery are examined here to help the reader understand the shapes of impeller blades. Parameter definitions in this chapter are used in Chapter 3 for hydraulic analysis of impeller and in Chapter 7.1 for the impeller Redesign model.

2.1 Coordinate System

The following variables and equations are included to help describe the specialized coordinate systems used to define turbomachinery components such as the centrifugal impeller. The change in M, distance along meridional curve (hub or shroud), is equal to:

$$dM = (dMR \cdot dR + dZ \cdot dZ)^{1/2} \tag{2.1}$$

Where R is the radius or radial location and Z is the axial location.

$$M = \int_0^s dMds \tag{2.2}$$

s is fractional distance along a curve (0 to 1). True 3D distance along camber line, C, can be calculated from:

$$dC = (dX \cdot dX + dY \cdot dY + dZ \cdot dZ)^{1/2} \tag{2.3}$$

$$C = \int_0^s dCds \tag{2.4}$$

Figure 2.1 show the relationship between the wrap angle and blade angle. The radius normalized distance along meridional curve, M', can be calculated from:

$$dM' = \frac{dM}{R} \tag{2.5}$$

By trigonometry the axial blade angle can be formulated as:

$$\beta = \text{atan}\left(\frac{d\varphi}{dM'}\right) \tag{2.6}$$

φ is the blade wrap angle or the rotation around Z axis from X axis towards Y axis (right hand rule).

$$\varphi = \int_0^S d\varphi ds \tag{2.7}$$

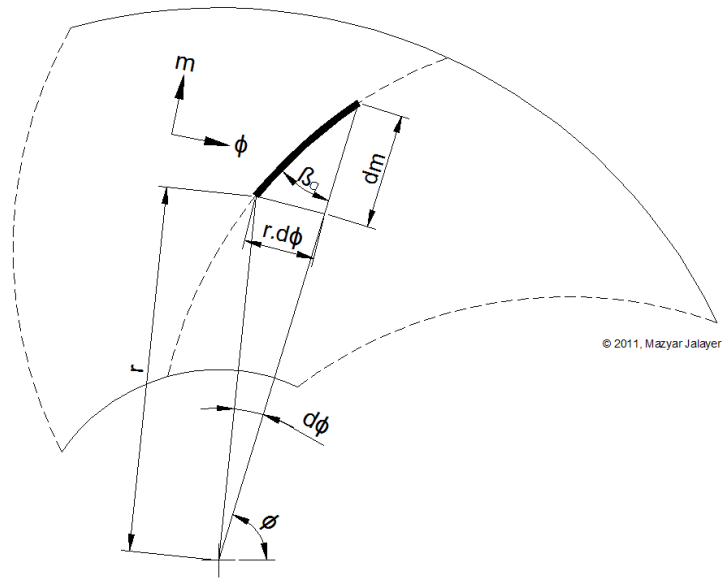

Figure 2.1: Wrap Angle Definition and the Relationship between Blade Angle

2.2 Single Blade Angle Curvature

The geometry of a centrifugal impeller is quite complicated. A fully radial impeller is much easier to comprehend and visualize. When the hub and shroud profiles are curved to form the inlet and the blade is extended into the inlet, the blade angles take on 3-dimensional (3-D) topology. Figure 2.2 show top view of a centrifugal radial impeller aligned with its meridional section. This type of geometry is referred to as single blade curvature since the curvature of blade at shroud is identical to that of the hub.

The meridional section is formed by taking the 3D passage boundaries (hub, shroud, inlet, and outlet) and collapsing them in the φ direction, forming a 2D passage outline on an axial-radial plane. The meridional profile is primarily determined by a set of curves (hub, shroud, inlet, and outlet).

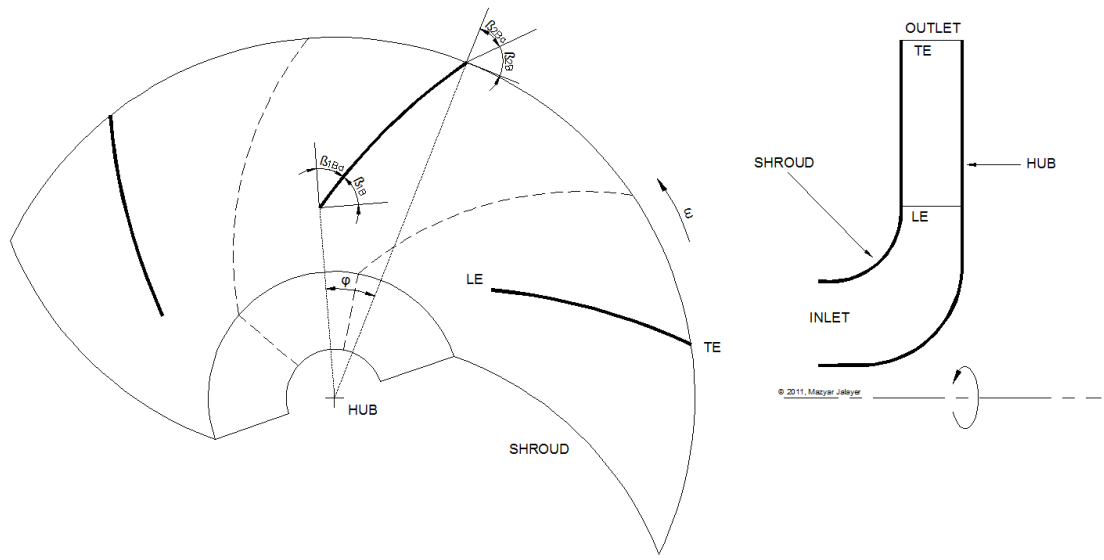

Figure 2.2: Single Blade Curvature

The impeller vane is bounded by hub and shroud curves as shown by the meridional profile. The blade at the leading edge (LE) has a tangential and axial angle β_{1B} and β_{1Ba}. At the outlet or the trailing edge (TE) the blade terminates at tangential and axial angle β_{2B} and β_{2Ba}. Since $\beta_{2B}+\beta_{2Ba}=90°$, unless otherwise stated, the blade angles in this work will refer to the tangential blade angle. The blade wrap angle, φ, is the angle at which the blade travels in the theta direction. The wrap angle can be calculated from the Equation (2.8).

$$\varphi(r) = \int_{r_1}^{r} \frac{1}{r' \cdot tan(\beta_a(r'))} dr' \tag{2.8}$$

The blade angle can change linearly from the LE to the TE or it can be a function meridional hub or shroud length. Linear blade profile can be described by Equation (2.9).

$$\beta_a(r) = \frac{\beta_2 - \beta_1}{r_2 - r_1}(r - r_1) + 90^{\circ} - \beta_1 \tag{2.9}$$

The fractional length of the blade on the φ-r plane can be determined from:

$$l_{\varphi r} = \int_{r_1}^{r_2} \left[1 + \left(r \cdot \frac{d}{dr}\varphi(r)\right)^2\right]^{1/2} dr \tag{2.10}$$

Using Mathcad the above equations can be used to plot the blade shape. Refer to Appendix A for Mathcad script program. It is interesting to see how the blade angle distribution can influence the shape, wrap angle as well as the length of blade.

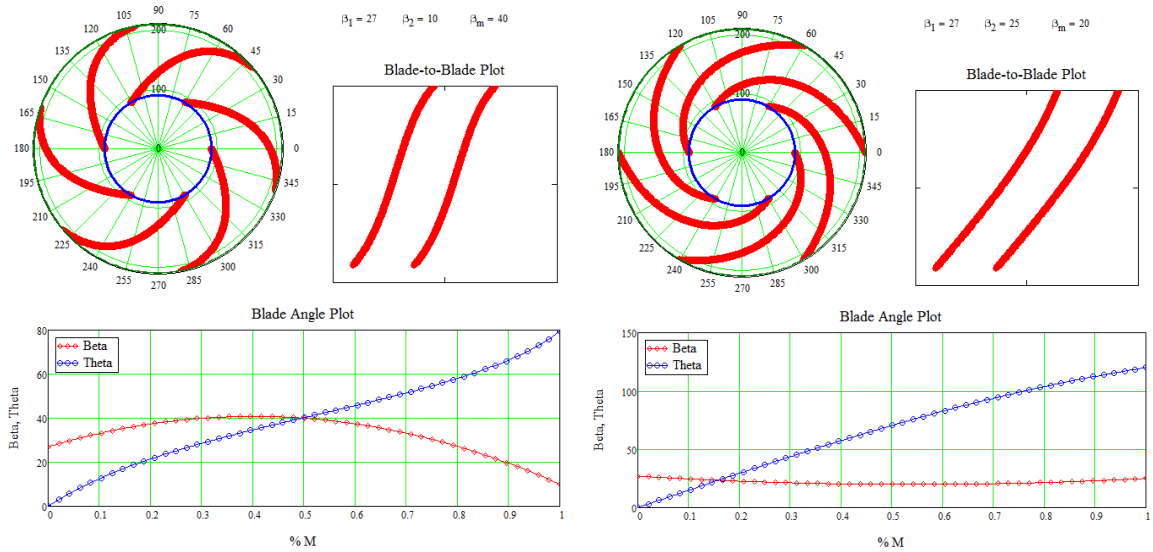

Figure 2.3: Mathcad Blade Shape Visualization

As it can be seen from Figure 2.3 the distribution of the blade angle over the meridional length can be used to shape fluid passageways inside the impeller. The blade angle distribution can affect the blade length, wrap angle and its shape. Here the blade angle distribution take on a simple quadratic fit. However blade distributions can take on any shape or function.

2.3 Double Blade Angle Curvature

Although fully radial geometry is quite simple visualize, in most centrifugal impellers the LE is extended into the inlet region where the hub and shroud profile curves are different. This can be seen from Figure 2.4. This impeller geometry is parameterized and will be utilized for this work onward. The geometry has been normalized by the impeller outer diameter D_2. Note that the hub and shroud blade curves do not align in the top view even though the β distributions are the same for both the hub and the shroud. Here the LE is defined at position 1 and the TE at position 2. The dash line from position 1 to 2 in the meridional and top view represents the mean streamline through the impeller.

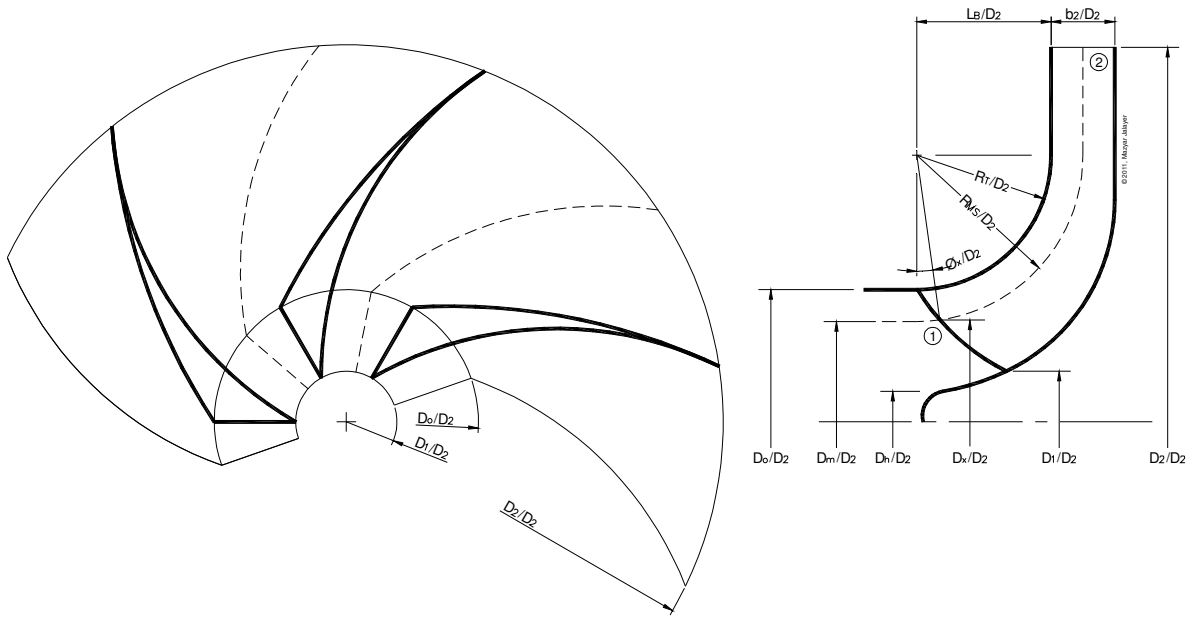

Figure 2.4: Double Blade Curvature Model

In order to relate mean streamline radius of curvature, R_{MS}, to the other geometrical parameters it can be assumed that:

$$R_{MS} = 0.5b_2 + R_T \tag{2.11}$$

Where the R_T is the shroud curvature radius and b_2 is the TE blade width. The ratio of hub diameter, D_h, to impeller eye diameter, D_o, is r. The ratio of mean streamline inlet diameter, D_x, to D_2 is y.

$$y = \frac{D_x}{D_2} = \frac{2R_{MS}}{D_2} + \left(2\frac{b_2 A_0(1-r^2)}{D_2 A_2(1+r^2)}\right)^{0.5} - \frac{2R_{MS}}{D_2}\cos(\emptyset_x) \tag{2.12}$$

A_0 is the area of the eye of the impeller. The ratio of the mean streamline inlet area to impeller outlet are is x.

$$x = \frac{A_x}{A_2} = \frac{\left(1 - \frac{A_0}{A_2}\right) R_{MS}\emptyset_x}{h_0} + \frac{A_0}{A_2} \tag{2.13}$$

h_0 is the length of streamline projection on the axial-radial plane (meridional profile).

$$\frac{h_0}{D_2} = 0.5 + \left(\frac{R_T}{D_2} + \frac{b_2}{2D_2}\right)\left(\frac{\pi}{2} - 1 - \emptyset_x\right) - 0.5\left(2\frac{b_2 A_0(1-r^2)}{D_2 A_2(1+r^2)}\right)^{0.5} \quad \textbf{(2.14)}$$

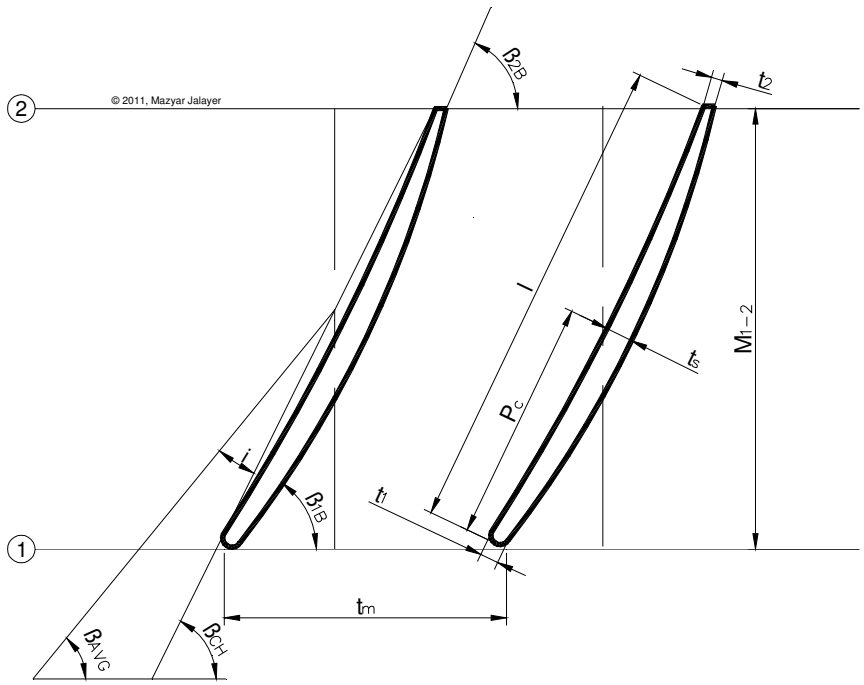

Figure 2.5: Blade-to-Blade Model

Figure 2.5 shows the blade-to-blade view of the impeller geometry. The average relative flow velocity, β_{AVG}, is defined as:

$$\beta'_{AVG} = \beta'_2 + \beta'_1 \quad \textbf{(2.15)}$$

β'_1 and β'_2 are true flow angle at inlet and outlet respectively which are difference from the blade true angle because of slippage and blockage. Chapter 3.2.2 will discuss the difference between the flow angle and blade angle in more detail. The blade chord angle is defined by the average of true blade angle:

$$\beta_{CH} = \frac{\beta_{2B} + \beta_{1B}}{2} \quad \textbf{(2.16)}$$

The difference between the β_{AVG} and chord angle, β_{CH}, is flow incidence against blade chord, i. The blade pitch can be defined as:

$$t_m = \frac{\pi D_m}{z} \tag{2.17}$$

z is the number of blades and D_m is the average impeller diameter. Thickness at leading edge and trailing edge is defined as t_1 and t_2. A dimensionless distance from hub to shroud (0 to 1) is defined as the span of the blade. The blade length projected on the meridional streamline can be defined by:

$$M_{1-2} = l \cdot \sin(\beta_{CH}) \tag{2.18}$$

The actual blade length can be defined by Equation (2.19):

$$\frac{l_{true}}{D_2} = \frac{h_0}{D_2} \cdot \frac{1}{\sin(\beta_{CH})} \tag{2.19}$$

Maximum camber length, t_s, is located from leading edge by P_c.

Chapter 3: Pump Impeller Hydraulics

This chapter describes pump impeller hydraulics and formulates the energy transfer inside impeller fluid passageways. Pump losses are examined and basic formulas which are used in Chapter 7.1 for the Redesign model are derived.

3.1 Absolute and Relative Fames of Reference

The flow in turbomachines such as pumps can be described in fixed coordinate called absolute flow or in rotating reference frame which is called relative frame. The flow in relative reference frame corresponds to a flow observed by a rotating observer. Hence a point on a rotating disk is stationary in relative reference frame, whereas in absolute frame of reference the point would be traveling in a circular path. If a particle travels radial outward on a rotating disk, it follows a straight path in the relative frame of reference. In the absolute frame of reference the particle would travel on a spiral path. Figure 3.1 shows the three velocities, peripheral velocity (ie. Circumferential speed) **u=ω*r**, the relative velocity **w**, and absolute velocity **c** which is obtained from vectorial addition. The bold notation here refers to quantities that have both magnitude and direction.

$$\boldsymbol{c} = \boldsymbol{u} + \boldsymbol{w} \tag{3.1}$$

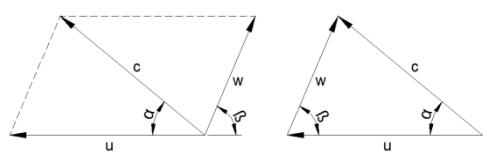

Figure 3.1: Velocity Triangles

3.2 One Dimensional Flow Calculation

The one dimensional (1-D) flow calculation for centrifugal pump will determine the main dimensions and vane angle of the impeller for a certain design duty point (flow, head and machine speed). In this calculation secondary flow and uneven velocity profiles inside the impeller are ignored and real flow is modeled by an idealized simple 1-D flow via streamline theory.

In a centrifugal pump the flow around the blade is evaluated in relative frame of reference. Therefore the relative velocities are important for the impeller where as the absolute

velocities are used to evaluate the volute or the diffuser. The concept of vector addition can be illustrated by Figure 3.2. Here the meridional component of absolute velocity, C_{m1}, will be introduced.

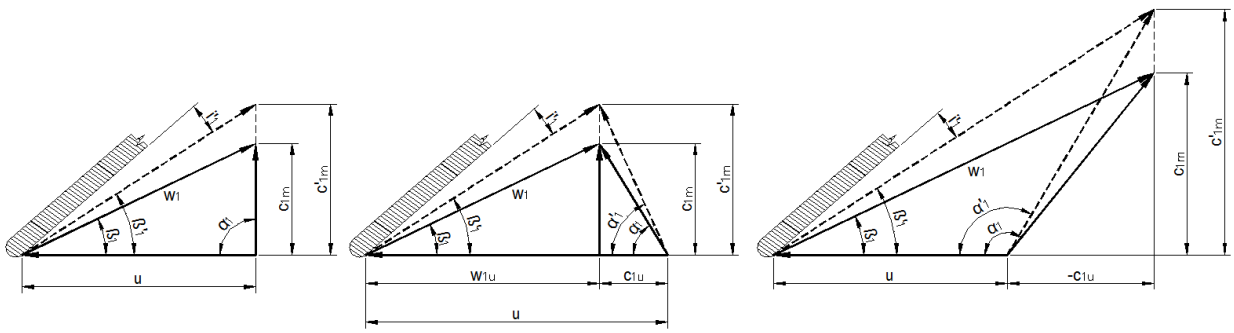

Figure 3.2: Non-Swirling, Pre-Rotation (Pre-Swirl), Counter-Rotation

Figure 3.2 demonstrates the velocity triangle at the inlet. The meridional velocity immediately upstream of the leading edge of the impeller blade is calculated from:

$$c_{m1} = Q_{imp}/A_1 \quad \text{Where} \quad A_1 = \frac{\pi}{4}[D_1^2 - D_h^2] \tag{3.2}$$

3.2.1 Inlet Flow Blockage

Immediately downstream of the leading edge the meridional velocity is increased by blockage factor, ξ, due to finite blade thickness which decrease the flow area.

$$c'_{m1} = \xi_1 \times c_{m1} \tag{3.3}$$

$$\xi_{1,2} = \frac{\pi D_{1,2}}{\pi D_{1,2} - \dfrac{z t_{1,2}}{\sin(\beta_{1B,2B})}} \tag{3.4}$$

It should be noted that the circumferential components of the absolute or relative velocities are not affected by blockage since angular momentum is conserved.

In most cases the flow to the impeller is usually axial (ie. α_1=90°). Therefore there is no circumferential component of absolute inlet velocity (c_{1u}=0). However, if inlet stator vanes (a device for pre-rotation) are installed or if the inlet part of pump casing generates a flow

where $\alpha_1 \neq 90°$, the circumferential component of absolute inlet velocity can be calculated from Equation (3.5).

Figure 3.2 shows the inlet velocity triangles where non-swirling $\alpha_1=90°$, pre-rotation (pre-swirl) $\alpha_1<90°$ and counter-rotation $\alpha_1>90°$.

$$c_{u1} = \frac{c_{m1}}{\tan(\alpha_1)} \tag{3.5}$$

The difference between the true flow angle and blade angle is known as incident.

$$i'_1 = \beta_{1B} - \beta'_1 \tag{3.6}$$

With certain flow conditions the flow angle is equal to blade angle which result in zero incident angle. This situation is known as "shock less entry". If the approach flow angle is below blade angle the stagnation point will be located on the pressure surface of the blade. If the inlet incident angle is negative the stagnation point will be located on the blade suction surface.

3.2.2 Slip Phenomenon and Flow Deflection

The angular moment which is generated by the impeller blades is the result of integral of pressure and shear distribution over the blade surface. For this reason there must be a greater pressure present on the pressure side of the blade than the suction side if a blade generates a force. Since pressure distribution on the impeller blade is result of velocity distribution around the blade, different flow fields must be present on the suction and pressure side. Therefore the flow is not able to follow the blade contour exactly. Work can only be transferred by deviation of flow field from the blade angle. This deviation is influenced by these mechanisms:

1. Velocity difference between the suction and pressure side of the blade.
2. Coriolis acceleration which is opposite to the direction of rotation. These accelerations cause secondary flow which conveys fluid flow from pressure to suction side of blade. This influences the flow angle.

Downstream of the trailing edge the difference between the static pressure at suction and pressure side of the blade attends to zero, therefore the free flow tends to take on different streamline curvature [**1**].

Figure 3.3 shows velocity distribution near the suction and discharge of impeller blade and secondary velocity profile at the trailing edge which is caused by Coriolis acceleration.

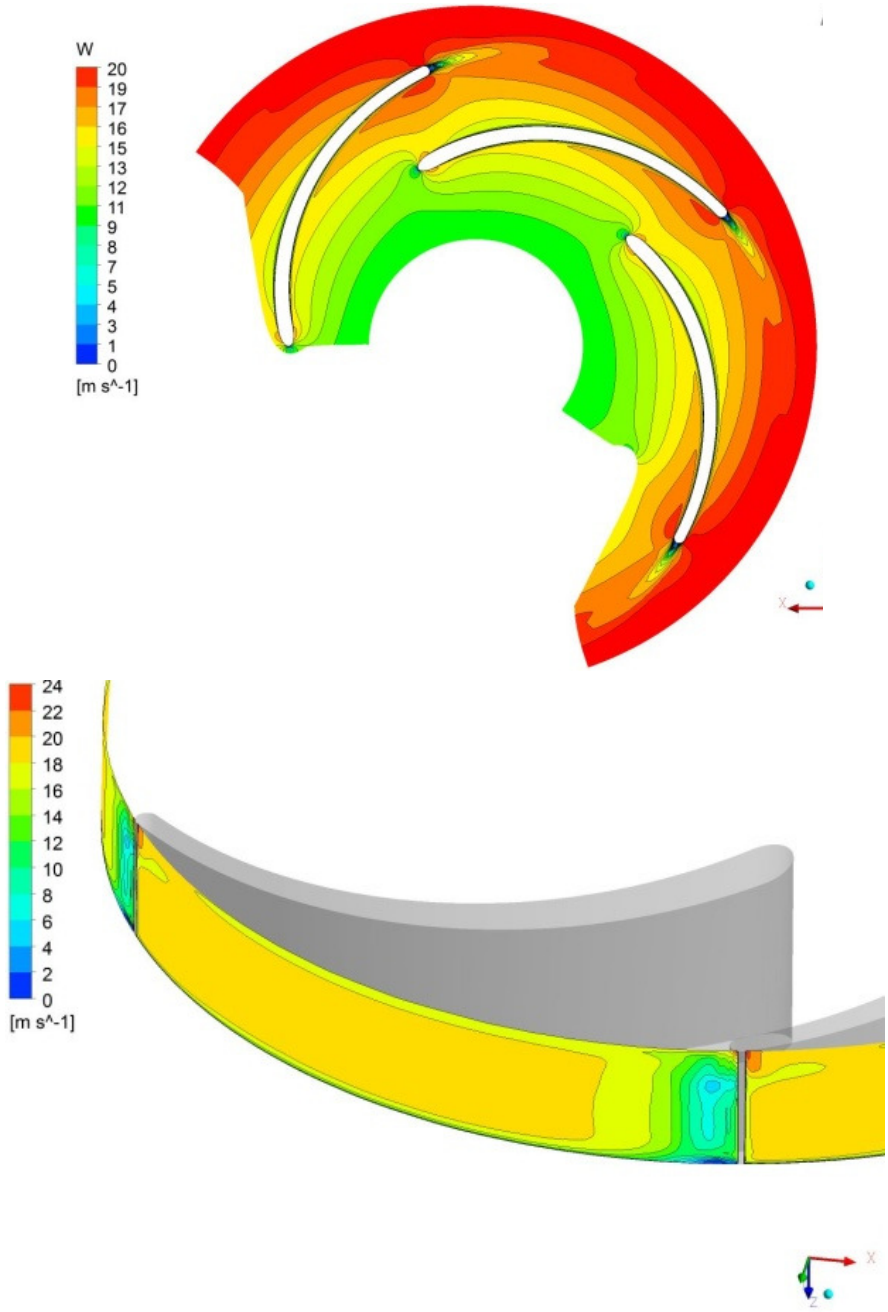

Figure 3.3: Velocity Distribution and Secondary Velocity Profile at TE

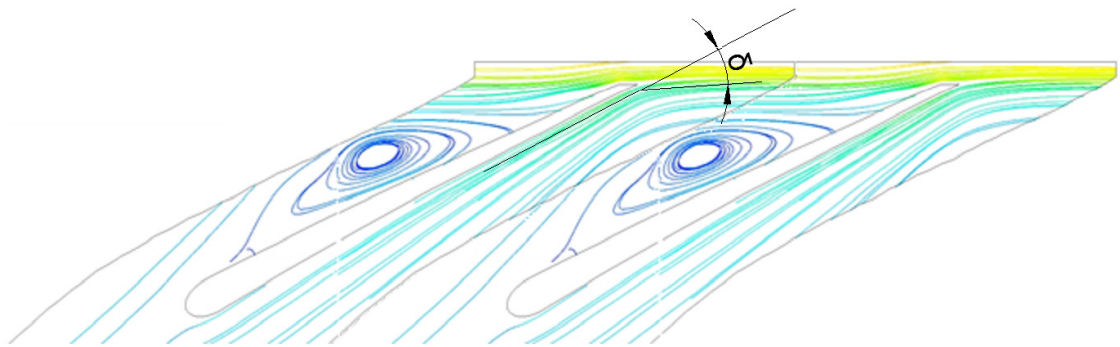

Figure 3.4: Slip Factor Visualization

For backward curved blades the flow angle deviates from the TE blade angle and this deviation of represented by the slip factor, γ. This phenomenon is show in the outlet velocity triangle, Figure 3.5. It should be noted that the effect of slip in radial blade (outlet blade angle is 90°) is entirely caused by the Coriolis acceleration [**8**]. This slip phenomenon can also be seen in

Figure 3.4 where 2D streamlines are shown in a Theta/Radial transformation plot (blade to blade plot).

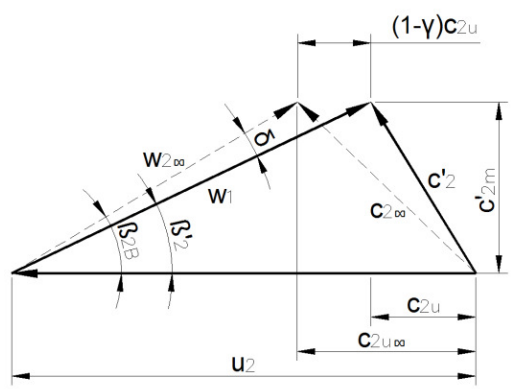

Figure 3.5: Slip Definition

Since the slip effect cannot be calculated by simple analytical means, empirical data have been used to calculate outlet flow angle for the 1-D streamline theory.

$$\gamma = \frac{c_{2u}}{c_{2u\infty}} = \frac{h_0 - \xi_2 \phi_2 \cot(\beta_{2B})}{1 - \xi_2 \phi_2 \cot(\beta_{2B})} \tag{3.7}$$

Table 3.1 shows slip data from Neumann [**1**]. The slip factor depends on both blade angle and the number of blades.

β_{2B}	z (Number of Vanes)								
	2	3	4	5	6	7	8	9	10
10	0.687	0.774	0.825						
11	0.676	0.76	0.812						
12	0.664	0.7445	0.799						
13	0.654	0.733	0.788						
14	0.644	0.723	0.779						
15	0.636	0.714	0.769	0.801	0.8217	0.851	0.864	0.879	0.8925
16	0.627		0.761						
17	0.618		0.754						
18	0.6115		0.747						
19	0.635		0.741	0.7775					
20	0.597	0.681	0.735	0.773	0.801	0.865	0.842	0.857	0.871
21	0.591	0.677	0.73	0.7685	0.7965	0.822	0.8385	0.855	0.868
22	0.5845	0.669	0.725	0.7645	0.7925	0.8185	0.8355	0.85	0.865
23	0.5787	0.6645	0.7205	0.76	0.7885	0.815	0.8325	0.848	0.862
24	0.573	0.6595	0.716	0.7565	0.785	0.8115	0.83	0.845	0.859
25	0.568	0.655	0.712	0.7525	0.782	0.808	0.827	0.843	0.8565
26				0.749	0.7785	0.805	0.8245		
27				0.745	0.7755	0.8025			
28				0.7415	0.7725	0.799			
29					0.77	0.7965			
30				0.7355	0.767	0.794	0.815	0.8315	0.845
31					0.765	0.7915			
32					0.7635	0.789	0.811		
33					0.76	0.787	0.809		
34					0.7575	0.7845	0.807		
35					0.7555	0.7825	0.805	0.823	0.836
36					0.7535	0.7805	0.803	0.8205	0.834
37					0.7515		0.8015		0.832
38							0.799	0.817	0.831
39							0.7975	0.815	0.8295
40						0.773	0.7965	0.814	0.828
41							0.796	0.813	0.8265
42							0.7935	0.8115	0.8245
45						0.765	0.7895	0.807	0.821
50						0.758	0.7825	0.801	0.8155

Table 3.1: Slip Factors

3.2.2.1 Profiling the Trailing Edge

Profiling the trailing edge effect the amount of slip and consequently the head and efficiency of the pump [**8**]. Profiling can be used where large differential pressure distributions exist on the suction and discharge side at the tailing edge. Figure 3.6 show various possibilities for profiling the trailing edge.

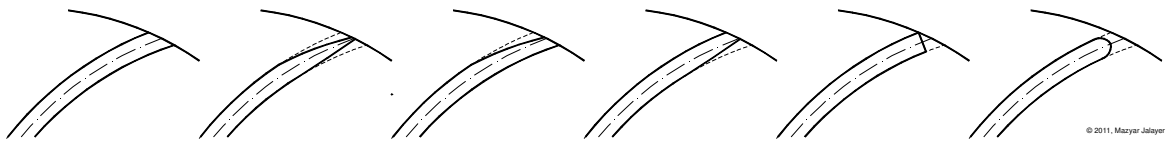

Figure 3.6: Profiling Trailing Edge

3.2.3 Energy Transfer and Impeller Work

To calculate the energy transfer from pump's impeller to the fluid, conservation of momentum is applied in Equation (3.8).

$$(P_1 + \rho c_1^2)A_1\mathbf{n}_1 + (P_2 + \rho c_2^2)A_2\mathbf{n}_2 = \mathbf{F}_{vol} + \mathbf{F}_w + \mathbf{F}_\tau \quad \textbf{(3.8)}$$

Figure 3.7 shows the control volume which is selected for calculation of moment acting on the blade $\mathbf{M} = \mathbf{M}_{loss} + \mathbf{M}_{imp}$

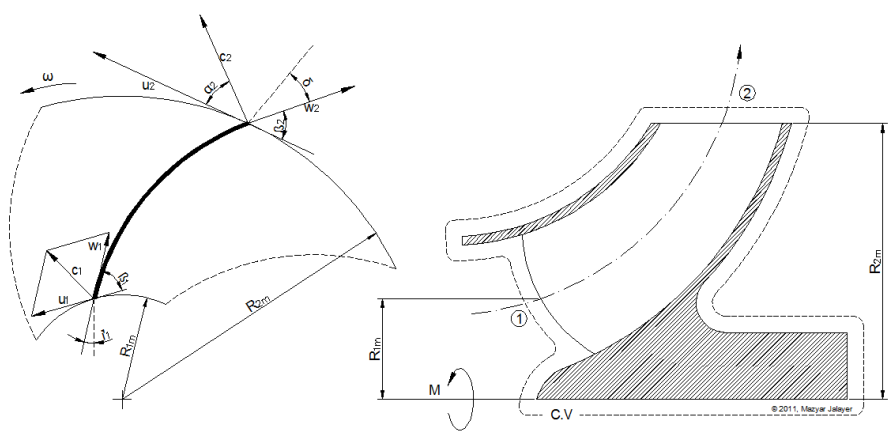

Figure 3.7: Impeller 1-D Energy Balance

Where M_{loss} is the moment which is caused by viscous shear stresses and M_{imp} is the moment acting on the impeller blade. The flow through the impeller, Q_{imp}, has an angular momentum of $\rho Q_{imp} R_{1m} c_{1u}$ at the inlet section 1. At the outlet (section 2), flow leaves with an angular momentum of $\rho Q_{imp} R_{2m} c_{2u}$. Turbulent shear stresses are present from section 1 to 2 since the control surface is perpendicular to $c_{1,2}$. These shear stresses generally produce a moment M_t. However, since the impeller is running at its BEP where there is no recirculation in the fluid passageways, this moment is neglected according to streamline theory [**1**].

The static pressure at 1 and 2 positions do not generate any forces in the circumferential direction. Therefore they are not incorporated in the momentum balance. Also the radial velocity components do not contribute to the angular momentum which acts on the surface of blade. Hence only the circumferential component of the velocity contributes to the moment generated [**8**].

$$M_{imp} = \rho Q_{imp}(R_{2m}c_{2u} - R_{1m}c_{1u}) \tag{3.9}$$

Here M_{imp} is the moment or torque which must be applied to generate the flow through the impeller. The corresponding power can be found by multiplying the moment by the rotational speed (angular velocity), ω, of the impeller.

$$P_{imp} = M_{imp}\omega = \rho Q_{imp}(u_{2m}c_{2u} - u_{1m}c_{1u}) \tag{3.10}$$

From Equation (3.10) and Figure 3.2 it can be seen that pre-swirl reduces blade momentum and power consumption whereas counter-swirl increases power [**10**].

3.2.4 Theoretical Head

The impeller power derivation gives rise to Euler's Equation (3.11). To find the hydraulic efficiency of the pump the actual head is divided by theoretical head of the impeller (which is calculated from 1-D streamline theory). This hydraulic efficiency includes all hydraulic losses from impeller inlet to the outlet.

$$H_{th} = \frac{u_{2m}c_{2u} - u_{1m}c_{1u}}{g} \tag{3.11}$$

$$\eta_h = \frac{\Delta H_{tot}}{H_{th}} \quad \textbf{(3.12)}$$

In a real pump (3D-flow), recirculations are present at partload. Therefore the 1-D streamline theory only applies to pumps operating without recirculation. This phenomenon is only achieved with pumps with infinite number of blades. Therefore, as one might suspect, as the number of impeller vanes increase the efficiency of the impeller also increases respectively. Another way to formulate the theoretical head of pump is from geometrical relationship of the velocity triangles.

$$\mathbf{u} \times \mathbf{c_u} = 0.5(u^2 + c^2 - w^2) \quad \textbf{(3.13)}$$

With this reformulation we can see that the theoretical head consist of three components: centrifugal u_2-u_1, deceleration of relative velocity w_1-w_2 and acceleration of the absolute velocity c_2-c_1. The Euler's equation can be expressed alternatively as:

$$H_{th} = \frac{u_{2m}c_{2u} - u_{1m}c_{1u}}{g} = \frac{u_2(u_2 - u_1)}{g} + \frac{u_2(\Delta w_u)}{g} - \frac{u_2 c_{2u}}{g} \quad \textbf{(3.14)}$$

Let us consider that at design point c_{u1}=0 (shockless entry, non-swirling), we can express the theoretical head as combination of the centrifugal head H_C and hydrodynamic head H_A, the first and second term in Equation (3.14) respectively. This breakdown provides a clear understanding of work and energy transfer inside the pump's impeller [**1**]. If u_2 is much larger than u_1 the hydrodynamic head will be small and negligible. This type of flow would correspond to impeller geometry with narrow inlet and large outlet diameter D_2. These types of impellers have low specific speed (Ns). Whereas impellers with u_2=u_1 generate head mostly from the second term and have relatively high specific speed. Hence these types of pumps are normally called axial machines. Pumps which display contribution from both centrifugal and hydrodynamic head are called mix flow machines.

Figure 3.8 show the type of geometry which result in centrifugal, axial and a combination of both centrifugal and axial head.

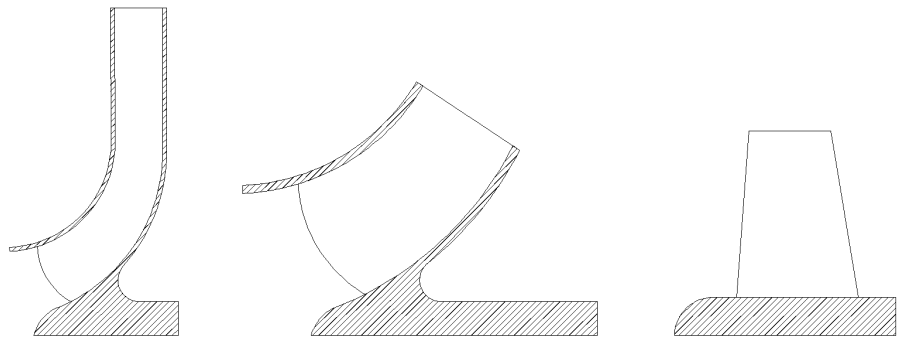

Figure 3.8: Radial, Mix and Axial Impeller

The specific speed of a pump can be calculated from the Equation (3.15). Here Q is the flow rate in gallon per minutes (gpm); the head is in feet (ft) and the machine's rotational speed is in revolution per minutes (rpm).

$$N_s = n\frac{Q^{1/2}}{H^{3/4}} \tag{3.15}$$

The true dimensionless specific speed of a pump can be calculated from the following equation, where any units can be utilized.

$$\omega_s = \frac{\omega Q^{1/2}}{(gH)^{3/4}} \tag{3.16}$$

3.3 Pump Losses

3.3.1 Hydraulic Losses

Hydraulic losses take place inside both the pump's impeller and the diffuser/collector (volute). These losses are generated through friction and vortex dissipation. Hydraulic losses are a combination of skin friction, shock, recirculation and mixing losses. Skin friction is result of shear stresses in the boundary layer of impeller's wetted surfaces. The Reynolds number and surface roughness are important in the viscous sub layer and attached flows. Therefore, friction losses are function of friction factor which is function of local Reynolds number and surface roughness. Friction is also directly proportional to square of the local average velocity and passage length.

$$h_f = f\frac{v^2}{2g}\frac{l}{D_H} \tag{3.17}$$

It is important to note that friction, Reynolds number and surface roughness has less impact in decelerated [**28**] or separated flows. In decelerating flow, flow is usually non-uniform and the exchange of momentum between the streamlines increase due to eddies. Larger eddies tend to breakup into smaller turbulences and then dissipate out by causing slight molecular movement (energy transfer to fluid) which in turn heats up the fluid slightly (transfer into not usable energy) [**8**]. This increase in temperature is different from the isentropic temperature rise which is cause by increasing the fluid pressure. This temperature raise will be further discussed in Chapter 8.

Dynamic losses are proportional to the square of the velocity and can be modeled as:

$$h_D = Const.\frac{v^2}{2g} \tag{3.18}$$

In order to minimize losses inside the impeller, non-uniform velocities must be minimized. This is done by reducing the blade loading. Incident flow can generate a deceleration zone and in some cases flow may separate. These types of losses are named shock losses. Local recirculation zones are caused by separation and zones of stalled fluid. The stalled fluid reduces the flow cross sectional area and accelerates the fluid to form a 'jet'. Large dynamic losses result from jet flow through impeller passageways in the vicinity of recirculation zone. Mixing losses is also apparent when the jet inters the diffuser. Figure 3.9 demonstrates this phenomenon. This Figure shows a plot of blade-to-blade streamline velocity for the OEM impeller. Refer to Chapter 6.4 for complete result of Component Calculation. The jet like flow and zone of stall fluid is demonstrated in this figure.

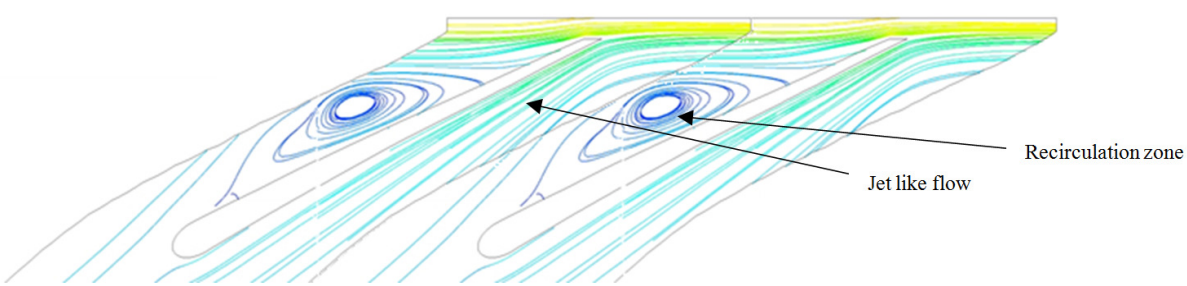

Figure 3.9: Zone of Stall Fluid and Jet like Flow

3.3.1.1 Impeller Friction Losses

Although the flow inside the impeller vanes is very complex, for simplicity it can be model as duct with variable cross section.

$$h_f = f\frac{l}{D_H}\frac{{w_{avg}}^2}{2g} \tag{3.19}$$

Where f=f(Re,ε)

$$f = 0.25\left[\log\left(\frac{4.52}{Re}\cdot\log\left(\frac{Re_{DH}}{7}\right)+\frac{\varepsilon}{3.7}\right)\right]^2 \tag{3.20}$$

The Reynolds number and roughness coefficient can be calculated from:

$$Re_{DH} = \frac{w_{avg}D_H}{\upsilon},\ \ \varepsilon = \frac{\varepsilon\prime}{D_H} \tag{3.21}$$

The average relative velocity can also be determined from velocity vectors [**1**], [**29**].

$$\frac{{w_{avg}}^2}{u_2^2} = \frac{{c_{m,avg}}^2}{u_2^2} + \frac{{w_{u,avg}}^2}{u_2^2} = \frac{{\phi_2}^2}{4}\left[\frac{\xi_1}{\frac{A_1}{A_2}}+\xi_2\right]^2 + \frac{1}{4}\left[1-\psi_2+\frac{D_1}{D_2}\right]^2 \tag{3.22}$$

The outlet head and flow coefficient can be calculated by non-dimensionalizing the circumferential and meridional component of absolute velocity with impeller outlet tip speed accordingly [**8**].

$$\frac{H_{th}}{u_2^2/(2g)} = \frac{c_{2u}}{u_2} = \psi_2 \tag{3.23}$$

$$\phi_2 = \frac{{c'}_{2m}}{u_2} \tag{3.24}$$

The hydraulic diameter varies along the fluid streamline. Therefore a weighted average is calculated based on pump geometry [**1**].

$$D_H = \frac{D_{H1} + 2D_{Havg} + D_{H2}}{4} \tag{3.25}$$

Hydraulic diameter at inlet and outlet, D_{H1}, D_{H2} can be calculated based on the geometry defined in Figure 2.4. This formula is derived from hydraulic diameter definition which is 4*area/wetted perimeter

$$D_{H1,2} = \frac{4A_{1,2} \cdot \sin(\beta_{1,2B})\, \xi_{1,2}}{\pi D_{1,2} \cdot \sin(\beta_{1,2B}) / \xi_{1,2} \cdot z} \tag{3.26}$$

Neumann [**1**] formulated the average hydraulic diameter to be:

$$\frac{D_{Havg}}{D_2} = \left[\frac{\pi b_2}{2zD_2}\right]^{0.5} \cdot \left[\frac{D_2 A_1}{D_1 A_2}\left(\frac{D_1}{D_2}\sin(\beta_{1B}) - \frac{t_1 z}{\pi D_2}\right) + \left(\sin(\beta_{2B}) - \frac{t_2 z}{\pi D_2}\right)\right]^{0.5} \tag{3.27}$$

3.3.1.2 Impeller Dynamic Losses

The dynamic losses which take place inside the impeller can be categorized into three types: inlet shock losses, wake losses and blade drag losses.

3.3.1.2.1 Leading Edge Shock Losses

The shock losses at the design point are small and negligible if the flow is aligned with blade angle. Shock losses tent to increase at partload. Due to highly complex flow through the inlet section of the impeller these losses cannot be estimated analytically.

3.3.1.2.2 Wake Losses

Whenever flow passes over a blunt body (a body with finite thickness) such an impeller blade, losses in flow occur due to wake shedding at the trailing edge. Neumann's [**1**] estimation for wake loss can be calculated from Equation (3.28).

$$\frac{h_w}{H_{th}} = (\xi_2 - 1)^2 \frac{{\xi_2}^2 {\phi_2}^2}{2{\psi_2}^2} \tag{3.28}$$

3.3.1.2.3 Blade Drag Losses

The blade drag losses can be calculated from average flow velocity and average blade angle.

$$h_{drag} = C_D \sigma \frac{{w_{avg}}^2}{\sin(\beta_{avg})} \frac{1}{2g} \tag{3.29}$$

Where C_D is the drag coefficient and σ is the solidity.

$$\sigma = l/t_m \quad \textbf{(3.30)}$$

For NACA 4-digit blade, the drag coefficient can be calculated from:

$$C_D = C_{D\,min} + d_2 \mathrm{X}^2 + d_3 \mathrm{X}^3 + d_4 \mathrm{X}^4 \quad \textbf{(3.31)}$$

Where d_2=0.0127, d_3=0.2*Camber/l, d_4=0.0086 and $\mathrm{X} = \frac{C_{LO} - C_{L\,opt}}{C_{L\,max} - C_{L\,opt}}$ **(3.31)**

$C_{D\,min}$ is the minimum drag coefficient and C_{LO} is the lift coefficient for a NACA airfoil, $C_{L\,opt}$ is optimal lift coefficient at minimum drag and $C_{L\,max}$ is the maximum lift coefficient [**1**].

$$C_{D\,min} = \left(\frac{5e10^6}{Re}\right)^{0.11} \left[0.0052 + 0.023m'\left(1 + 100m'^2\right) + 0.07\left(\frac{t_s}{l}\right)^2 + 1.67m'^2 p_c^3\right] \quad \textbf{(3.32)}$$

$$C_{L\,opt} = m'[109 - 14.1\log(Re)] \cdot \left[1 - 4\left(\frac{t_s}{l}\right)\right] \quad \textbf{(3.33)}$$

$$m' = 0.25\tan(\beta_{2B} - \beta_{CH}) \quad \textbf{(3.34)}$$

For NACA 65 p_c=0.5 and $C_{L\,max}$=1.1

3.3.2 Secondary Losses

Secondary losses inside the impeller consist of disk friction, volumetric losses and mechanical losses.

3.3.2.1 Disk Friction Losses

When a disk or a cylinder rotates in fluid, shear stresses due to local friction coefficient act on is disk's surface. Generally power consumption due to disk friction can be determined from Equation (3.35).

$$P_{disk} = const \cdot n^3 \cdot D_2^5 \quad \textbf{(3.35)}$$

The constant of proportionality is a function of surface roughness and fluid viscosity.

3.3.2.2 Volumetric Losses

Volumetric losses take place between the rotating and stationary components of the pump. In an open or semi-open impeller these losses take place between the impeller and side plate. Other volumetric losses can result from mechanical seals, glands and balance devices. Indeed there is a definite tradeoff between disk friction and volumetric losses. Since disk friction which takes place between wear plate (side plate) and impeller increases with decrease impeller shroud clearance, the lower the leakage the greater the disc friction.

3.3.2.3 Mechanical Losses

Mechanical losses are external losses which are associated with the power loss that takes place between sliding surfaces such bearing or seals. This type of losses will not be discussed in this work and do not impact the efficiency of the impeller.

3.4 Similarity Characteristic

As it was stated earlier turbulent flow inside complex passageway (vanes of pump) cannot be described accurately by analytical means. However these flows can be treated with similarity laws where dimensionless coefficients calculated from model test results can be applied to geometrically similar prototype to predict important flow parameters such as power, head and flow rate. The similarity laws for pumps can be derived from velocity triangles where the inlet and outlet velocities can be non-dimensionalized by circumferential velocity u_1 and u_2. Therefore we can define two flow coefficients as:

$$\phi_1 = \frac{c'_{1m}}{u_1} \tag{3.36}$$

$$\phi_2 = \frac{c'_{2m}}{u_2} \tag{3.37}$$

From the velocity triangle it can be seen that ϕ_1 and ϕ_2 are identical regardless of its geometrical scale.

3.5 Influence of Roughness and Reynolds Number

The energy losses in a pump depend on the flow Reynolds number and the surface roughness similar to a fluid flow in a pipe. For this reason pump efficiency cannot be simply scaled

from a model to a prototype pump. The effect of Reynolds number and surface roughness on the efficiency of the pump is discussed in great detail by Gulich [**30**].

3.6 Minimization of Impeller Losses

Hydraulic losses account for most of the efficiency reduction in the centrifugal impeller. To minimize the losses inside the pump impeller, the vane geometry must be optimized to reduce losses. As it can be seen from the definition of friction loss, long blades cause excessive friction losses because of increase in wetted surface area. On the other hand, shorter blade length can cause mixing losses because the fluid is not guided well inside the passage. By the same token, the number of blades can affect losses as well. Fewer numbers of blades would mean that the flow is not guided well. With reduction of number of blades the dead space in impeller passageway increases causing recirculation losses. Too many vanes can block the fluid flow by reducing the available flow area. Regions of flow separation and zones stalled fluid can cause uneven pressure distributions on the suction and pressure side of the blade. Too many blades can also lead to increase in wetted surface area and hence increase in both friction and drag. Both disk friction and flow friction are function of surface roughness. Smooth surfaces, such as coating, can reduce resistance caused by friction and viscosity [**31**].

The impeller hydraulic efficiency can be calculated from Equation (3.38). The impeller final efficiency is then calculated from Equation (3.39).

$$\eta_{h,imp} = 1 - \left(\frac{h_f}{H_{th}} + \frac{h_w}{H_{th}} + \frac{h_{drag}}{H_{th}}\right) \tag{3.38}$$

$$\eta_{imp} = \eta_{h,imp} \cdot \eta_{Disk} \tag{3.39}$$

$$\eta_{pump} = \eta_{imp} \cdot \eta_{vol} \cdot \eta_{mech} \tag{3.40}$$

3.7 Airfoil Theory

Figure 3.10 shows blade loading forces. If the pressure generated by total head of pump is located at the middle of blade, the pressure coefficient associated with axial and centrifugal head can be utilized similar to those of airfoils. The derivation for these coefficients can be found in Appendix IV of reference [**1**].

$$C_{LA} = \frac{2t_m \cdot w_u \cdot D_2}{l \cdot w_{avg} \cdot D_m} \tag{3.41}$$

$$C_{LC} = \frac{2t_m \cdot \gamma \cdot D_2 \cdot (u_2 - u_1)}{l \cdot w_{avg} \cdot D_m} \tag{3.42}$$

$$C_L = \frac{2t_m \cdot c_{u2} \cdot D_2}{l \cdot w_{avg} \cdot D_m} \tag{3.43}$$

The centrifugal lift coefficient, C_{LC}, and the axial lift coefficient (which is contributed from the blade shape), C_{LA}, are lower than total lift coefficient, C_L. Therefore the balance of the coefficients can be derived from:

$$C_L = C_{LC} + C_{LA} \tag{3.44}$$

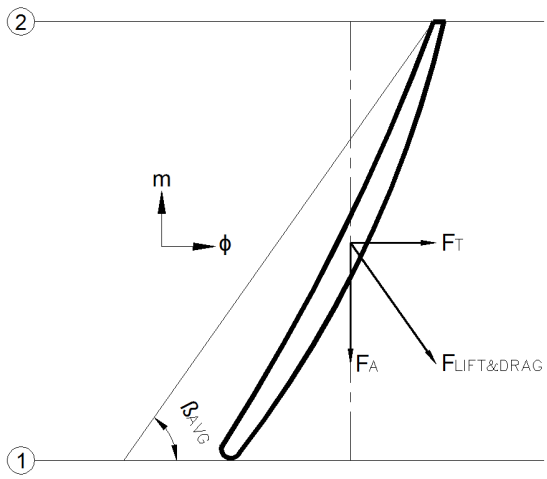

Figure 3.10: Component of Force Vector Acting on the Blade

If the pressure from the impeller blades is developed in absent of hydrodynamic loading (C_{LA}), then the blades will be characterized by high number of blades and low blade angle which would result in high slip coefficient [**8**]. Such blade geometry would result in long blade length, high friction losses and mixing losses in the diffuser/collector due to high slip. To minimize impeller losses the optimal designs usually have some degree of hydrodynamic loading. The hydrodynamic loading criterion presented here permits the use of airfoil theory to drive a series of optimal blade geometries which consists of (the number of blades and blade outlet angle) based on a particular Hub and Shroud curves. This will be the topic of discussion for chapter 7.1.

3.7.1 Correction for Radial Cascade

The lift and drag data which are listed for various airfoil profiles are represented for an isolated foil. The effect of thickness and adjacent blades in a redial cascade has to be taken into account. For this reason a correction factor (a/a_o) will be introduced here.

For a solidity factor $1/\sigma<0.6$ Wislecenus [**32**] suggested the fallowing formula:

$$\frac{a}{a_o} = \frac{2}{\pi \cdot \sigma \cdot \sin(\beta_{CH})} \tag{3.45}$$

The effect of blade thickness displaces the lift characteristic towards higher incidence. Neumann [**1**] proposed Equation (3.46) for correction of angle of attack due to finite blade thickness in a radial cascade.

$$\Delta\alpha = const \cdot \sigma \cdot \cos(\beta_{CH}) \tag{3.46}$$

Where the corrected angle of attack, α_T, is sum of $\Delta\alpha$ and α (the angle of attack for isolated foil).

Chapter 4: Performance Prediction and Numerical Calculation

This chapter describes various challenges associated with numerical calculation of centrifugal impellers and pumps. Techniques for modeling the flow through the impeller passage are discussed in detail. Two types of flow calculation will be discussed: component calculation and stage calculation. Complex fluid flow behavior is examined and shortfalls of various turbulence models are discussed. Grid generation and appropriate boundary conditions are also examined. Post processing methods which are used to calculate pump performance are formulated. Chapter 6 will apply these methods and processes to the numerical assessment of OEM impeller. Together with experimental results of Chapter 5, the Computational Fluid Analysis (CFD) process is validated.

4.1 Introduction

Real 3 dimensional (3D) fluid flows such as the one inside the impeller passageways are described by partial differential equations which cannot be solved analytically without over simplification. Numerical method allows solving of these equations by dividing the fluid domain into small cells called grid or mesh. The application of numerical methods to pump geometry will be the discussion of this chapter.

Since flow visualization in confined spaces such as a pump's fluid passageway is challenging and expensive, numerical calculation provides an effective tool for design and analysis of pumps [**33**], [**34**]. The numerical method can be used to minimize hydraulic losses and to calculate head and flow at design and partload.

4.2 Numerical Method Based on Navier-Stokes Equations

In order to present some of the limitations associated with numerical methods the Navier-Stokes equations shown in this section. For a 3D incompressible fluid flow with velocity u, v, and w which correspond to the component of relative velocity in Cartesian coordinate system where the fluid domain rotates around the Z-axis, the conservation of momentum for the X direction can be written as [**35**]:

$$\frac{\partial u}{\partial t} + u\frac{\partial u}{\partial x} + v\frac{\partial u}{\partial y} + w\frac{\partial u}{\partial z} + \frac{1}{\rho}\frac{\partial p}{\partial x} - \omega^2 x + 2\omega v$$
$$= \mu\left(\frac{\partial^2 u}{\partial x^2} + \frac{\partial^2 u}{\partial y^2} + \frac{\partial^2 u}{\partial z^2}\right) + \frac{1}{\rho}\left(\frac{\partial \sigma'_x}{\partial x} + \frac{\partial \tau'_{xy}}{\partial y} + \frac{\partial \tau'_{xz}}{\partial z}\right) \quad \textbf{(4.1)}$$

Here, only the X component of momentum equation is shown. The three momentum equations and the continuity equation give a system of four equations and four unknown (u, v, w, p).

$$\frac{\partial u}{\partial x} + \frac{\partial v}{\partial y} + \frac{\partial w}{\partial z} = 0 \quad \textbf{(4.2)}$$

This equation is written for rotating impeller or relative non-rotating domain such as pumps inlet, collector or diffuser. Gravity is neglected here since the domain is small. For larger pumps, however, the effect of gravity cannot be neglected. On the left hand side of the equation effect of pressure and body forces such as centrifugal and Coriolis acceleration in a rotating system can be seen. The right hand side contains the effect of viscosity (molecular) and losses due to turbulent exchange of momentum. If the second term on the right hand side is neglected (small), Navier-Stokes equation for laminar flow is derived.

These sets of equations are complete to calculate turbulent flow inside the pump. However, direct numerical simulation (DNS) of a pump is computationally expensive and requires a very fine grid since DNS requires number of element on the order of $Re^{9/4}$ [**36**].

By replacing the velocity with a summation of a time-average velocity and its turbulence fluctuation, Equation (4.3) can be given as 'Reynolds average Navier-Stokes equation' (RANS).

$$u = \bar{u} + u' \quad \textbf{(4.3)}$$

Since turbulence fluctuation velocities u', v' and w' are unknown, the four equation (3 momentum and one continuity) cannot be solved directly. Empirical equations (closure equations) can be used to solve the four partial differential equations. These empirical equations are essentially referred to as turbulence models. Therefore one of the main uncertainties associated with numerical analysis of turbomachinery is pertaining to selection of the turbulence model and values of turbulence 'tunable' parameters.

4.3 Turbulence Models

All turbulence models are empirically derived from experimental tests done on a particular geometry and fluid flow. Since the fluid flows in different geometries are not the same, there exists no universal turbulence model which can describe the fluid flow for all application. Therefore it is necessary to select a suitable turbulence model for calculation and validate the computational result with experimental test result.

Some turbulence models employ the concept of eddy viscosity and in some case the eddy viscosity replaces the molecular viscosity altogether. Eddy viscosity is determined by flow features where as molecular viscosity is physical material property.

For identifying the turbulence model that best describes the fluid flow inside a pump's impeller it is important to identify the types of fluid flow. The list below identifies the characteristic of fluid flow inside the pump.

- Accelerating and decelerating flow
    - Accelerating flow arises at the inlet of the impeller where the flow area decreases upstream of the inlet. Decelerating flow developed downstream of the LE where the flow area increases. Figure 4.1 shows the accelerating and decelerating flow inside impeller fluid passageways. In the decelerating flow the boundary layer grows and shear stress drop. At some point flow separates from the wall which results in recirculation or zone of stall fluid. It is important to select an appropriate turbulence model that can predict the amount and onset of separation accurately.
- 3D-Boundary layer
- Swirling flow
- Secondary flows
    - These are caused by two effects: Coriolis acceleration which is opposite to direction of rotation and transports the fluid towards the pressure side of the blade, and secondary flows which arise from the fact that fluid passageways are not circular.
    - The fluid passageway inside the impeller resembles a square channel. In a square channel the velocity distribution is not rotational symmetric (axisymmetric). For this reason the wall shear stresses change over the surface

of channel which results in secondary flows. Figure 4.2 shows these secondary flows. These secondary flows are described in detail in reference [**34**]

- Flow with curved streamline
- Rotational flow
- Flow with strong velocity gradient

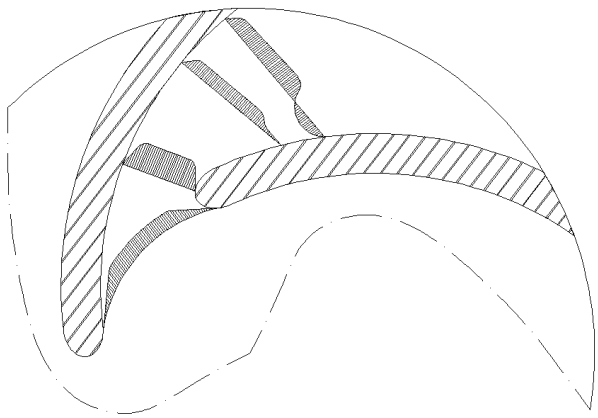

Figure 4.1: Flow Separation Inside Pump Impeller Fluid Passageways

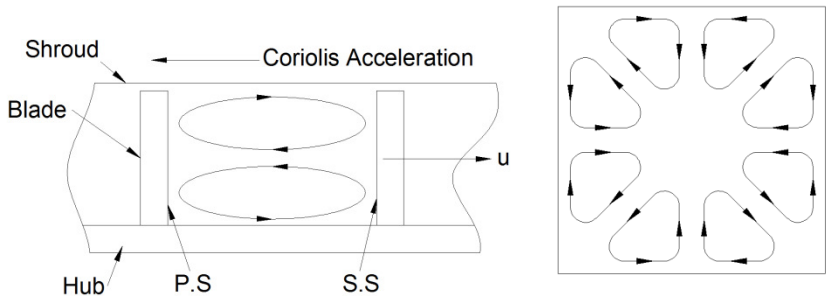

Figure 4.2: Secondary Flows due to Coriolis Acceleration (Right) and 3D Boundary Layer (Left)

4.3.1 Standard k-ε Model

The standard k-ε model is currently the most used turbulence model for CFD calculation. It is based on the turbulence kinetic energy and the dissipation rate of turbulence fluctuation. This model is extremely weak at modeling fluid flow associated with centrifugal pumps (curve flow path, secondary flow, separations). In spite of its disadvantages; this model is readily used to predict fluid flow in turbomachinery since the solution can easily converge [**20**] .

With the k-ε model the calculation of losses becomes unreliable. Also locations of serrations are not recognized or are underestimated. This affects the calculation result for efficiency.

4.3.2 k-ω Model

This model works best for strong pressure gradients, and captures the flow near the walls with high degree of accuracy when compared with k-ε. One of the advantages of the k-ω formulation is the near wall treatment for low-Reynolds number computation [**38**].

4.3.3 Shear Stress Transport Model

This model uses k-ε model for core flow and k-ω near the walls. Also the eddy viscosity is modified so that shear stresses are limited due to pressure gradients. This model is by far the most robust turbulence model that can be deployed for numerical investigation of impeller. This model is highly accurate at predicting the onset and the amount of flow separation under adverse pressure gradients [**39**].

4.4 Simulation Types

There are two types of flow simulation for centrifugal pumps: component calculation and stage calculation. In component calculation individual component such as inlet, impeller, collector and diffuser are individually analysis. Whereas stage calculation involves calculation of entire stage: inlet, impeller and the volute.

4.4.1 Steady Component Calculation (Impeller)

The steady component calculation of impeller consist of a periodic domain since the entire impeller domain is cyclic symmetric. Therefore to save computational time, periodic boundary conditions (BCs) are introduced between the vanes at mid pitch. Figure 4.3 demonstrate the mid pitch periodic BC. The component calculation results in theoretical impeller head, $H_{th,m}$ (which is the total pressure rise) and static pressure rise H_p. The hydraulic efficiency of the pump can then be calculated from $H_p/H_{th,m}$. This individual calculation of impeller cannot give the head or the efficiency of the pump, since the losses in the collector are not taken into account. Also strong interaction between the rotator/stator is ignored. These interactions play an important role in determining the true performance of the

pump especially at partload. Despite its shortfalls, the component calculation is computationally less expensive than other calculations. It can be used to predict the pump performance at BEP.

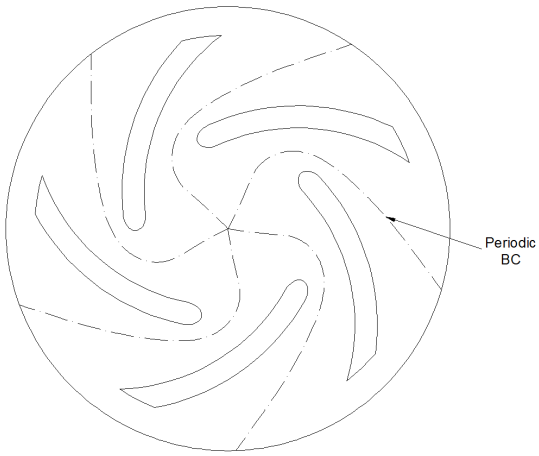

Figure 4.3: Periodic Boundary Condition

4.4.2 Steady Stage Calculation (Complete Pump)

Since the volute/collector/diffuser lack rotational symmetry, the fluid flows inside each impeller fluid passageway are not identical because of strong rotor/stator interaction. This is especially true near the volute cut water (tongue). Stage calculation of inlet domain along with impeller and collector/diffusers is the most realistic simulation of centrifugal pump. The stage calculation allows accurate calculation of interaction between the impeller and volute, especially the exchange of momentum between the main flow and recirculating fluid inside the pump. At very low flow rates, particularly at shutoff head, the effect of inlet stator vanes or ribs which induce pre-swirl and its interaction with recirculating fluid can only be correctly modeled with stage calculation [**8**].

For the component calculation of impeller, none convergence is a problem at near shutoff head (simulating deadheading of the pump). This is because recirculation can sometime extend into the inlet of the outlet domain. However, in stage calculation, recirculation will not be a problem for convergence since the circulating flow can extent into the collector domain and by the time it reaches the outlet boundary it will have vanished.

The flow inside the pump is highly unsteady and pulsating because the head, flow and shaft power strongly depend on the rotator/stator fluid interaction. These quintiles are function of rotational offset angle between the volute cut water and the impeller vanes. Figure 4.4 shows the rotational offset between four vane impeller and the volute. In order to obtain the overall performance of a pump, the performance for a set of offset angle ranging from 0° to 360°/z has to be obtained and averaged.

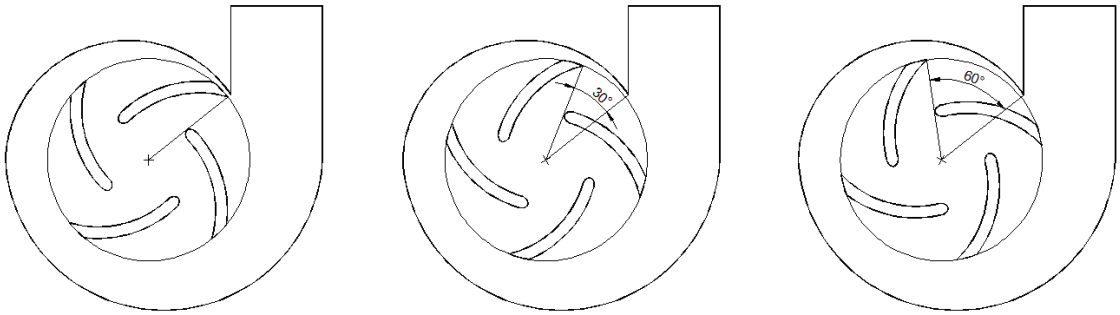

Figure 4.4: Angular Position of Impeller and Flow Calculations

Since the calculation for the rotor (impeller) is done in relative (rotating) frame of reference and the stator (volute) is in absolute (stationary) frame of reference, a mixing plane or a frozen rotor model is used. This mixing plane or the frozen rotor interface is introduced between the impeller outlet and the volute inlet. In the mixing plane the circumferential average velocity and pressure are used as inlet boundary condition for volute/corrector. Whereas for the frozen rotor the 3-D velocity profile and pressure profile for the impeller outlet is used for the boundary condition of volute/collector inlet.

There are many types of domain interface models. Two main types of model are utilized by ANSYS CFX. Explanation of these models can be found in reference [**40**].

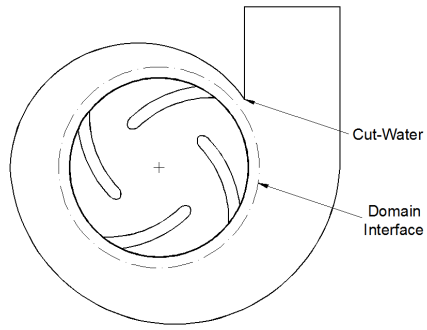

Figure 4.5: Domain Interface

Figure 4.5 shows a domain interface between the impeller and the volute (mixing plane or frozen rotor model), as a dash line. The dark circular line represents the radial extent of the impeller vanes. It is good practice to extend the domain interface halfway between the cut water and the blade TE [**35**].

4.4.3 Unsteady Calculation of a Complete Machine

The flow inside the pump is fundamentally unsteady because of rotor stator interaction as was discussed in the above. The most accurate flow simulation of pump involves unsteady calculation of a complete machine. This is done by calculation of sliding mesh over approximately 10+ revolution of impeller [**41**]. Similar to steady calculation the performance of the pump is obtained by averaging the head, flow and calculated shaft power over one periodic angle (0° to 360°/z).

The transient rotor/stator simulation models the transient flow behavior. In this calculation a sliding domain interface is used to allow rotation of the impeller component with respect to the collector. This type of calculation is robust and highly accurate. The disadvantage is that it is computationally expensive and large amount of data storage is required [**42**].

4.5 Grid Generation

High quality mesh is one of the most important requirements for CFD of centrifugal impeller. Coarse mesh can adversely affect the results. If the viscous sublayer is captured by only few cells, the wall shear stresses which have direct impact on hydraulic losses are inaccurate,

resulting in over and or under perdition of pumps performance. Equally important is the shape and proportion of the cells. This aspect of element shape and proportion is crucial for block type mesh more so than a domain which is constructed from tetrahedron cells (unstructured mesh).

Two types of mesh exist for pump impeller and volute: block structured and unstructured mesh. Unstructured mesh is relatively simple to apply to any complex geometry. However, they tend to use more elements and twice as many nodes to produce the same quality of calculation result when compared with a block structure domain. Block structure domain requires substantial time and effort to construct. However, calculation with this type of mesh converges faster and more efficiently.

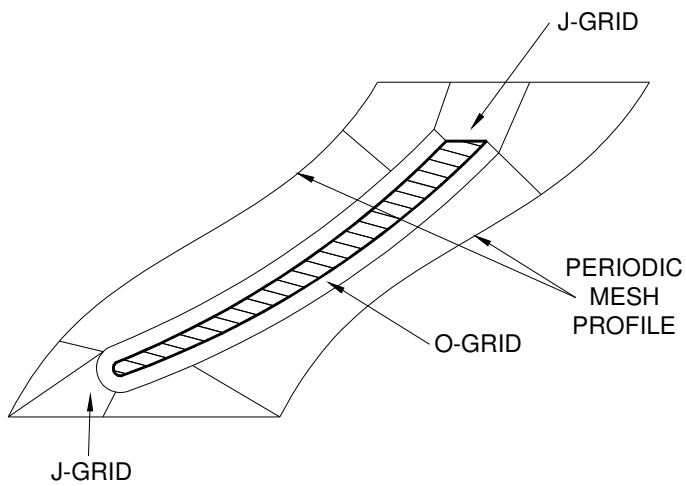

Figure 4.6: Structured Mesh Topology

It is important to note that for block mesh the elements or the grid has to be constructed in a way that the gridlines are perpendicular to the walls. This makes the meshing of curved domain, such as the one associated with two vane impeller with large wrap angle very difficult. In order to capture the fluid flow in the viscous sub layer, the grid must be orthogonal to blade structure by deploying O-grid around the mesh. O-grid produces excellent boundary layer resolution. The thickness of the O-grid can be set to a value (t_{OGrid}) times the blade thickness. Figure 4.6 shows a generic topology of single blade passage in the blade-to-blade transformation. J-Grid is deployed to transition the mesh from inlet/outlet to

orthogonal O-grid mesh at the LE and TE. The O-grid grows in sized from the blade wall to the surrounding H-grid. L-grid is sometime used to optimize the grid.

The grid should be monitored for quality based on these criteria which are identified by various solvers such as CFX or FLUENT.

- Maximum Face Angle
- Minimum Face Angle
- Connectivity Number
- Element Volume Ratio
- Minimum Volume
- Edge Length Ratio

4.5.1 Near Wall Treatment

Since velocity and its turbulence fluctuation approaches to zero close to the solid surface (on hub, shroud and around the blade), it is necessary to provide fine grid resolution near these surface in order to resolve the flow down to the viscous sublayer

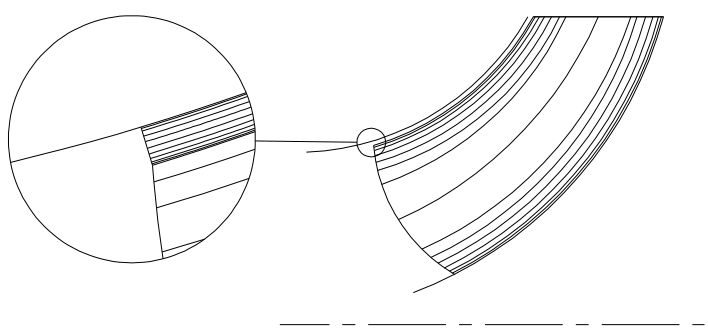

Figure 4.7: Blade to Shroud Clearance Modeling

$$y^+ = \frac{y \cdot V_\tau}{\nu} \text{ where } V_\tau = \sqrt{\frac{\tau_w}{\rho}} \quad \textbf{(4.4)}$$

Figure 4.7 shows the span wise distribution of elements and element size near the wall for shroud and hub surfaces. In order to capture the boundary layer at the hub and shroud, appropriate element growth rate and dimensionless distance from the wall (y+) must be

selected. Furthermore, the number of element and size at the shroud clearance is very important in determining the losses due to disk friction and for correct modeling of volumetric losses of an open impeller. At this location large numbers of small elements are required. With addition of shroud tip clearance, sometime the domain number of elements can increase by as much as 30%. The drawback for blade/shroud clearance is that the model will become computationally expensive.

4.6 Boundary Conditions

All the variables in the transport equations require boundary conditions (BCs) at the borders of the calculation domain. If the BCs are not modeled properly, the solution might not converge or performance prediction will be erroneous.

4.6.1 Inlet

At the inlet either total pressure, static pressure, mass flow rate or velocity distribution profile which is given by x, y, z component should be specified. Since the velocity distribution or flow angle is not known, mass flow and average pressure (static/total) at the inlet can be specified. Turbulence parameters such as turbulence level, length scale or the ratio of eddy viscosity to molecular viscosity must be specified at the inlet. Generally, the higher the turbulence level, the higher the exchange of momentum in the flow. In centrifugal impeller turbulence intensity level of 5% has been in agreement with experimental result [**5**], [**14**].
It should be noted that if pressure difference is specified at the inlet and outlet, convergence might become problematic at part load and off design conditions because of flatness of the head/flow curve.

Also inlet BC becomes problematic at part load due to extension of recirculation zones from the computation domain into the inlet. Inlets and outlets are strictly one-way flow BC. Therefore care must be taken to specifying velocity components for these boundaries. To solve this problem the following can be done:

- By moving inlet/outlet to a region away from recirculation zones by, perhaps, extending the flow domain further upstream or downstream.

- By using an opening to describe subsonic flow where simultaneous inflow and outflow may occur.
- If the volute domain is coupled with impeller domain by means of a mixing layer, the collector and diffuser could act to remedy this problem.

4.6.2 Outlet

The condition of outlet represents the result of the calculation. At the outlet the pressure and velocity distributions can establish themselves. This means that either the pressure or velocity distribution should be specified at the outlet. If the average static pressure at the outlet is specified, then the velocity distribution is calculated by the numerical code. If, however, the flow rate is specified, then the magnitude of flow and the flow direction should be specified at the outlet.

4.6.3 Periodicities

In order to save computational time often one segment of impeller is analyzed in the component calculation. For this reason periodic BCs should be specified mid-pitch between two vanes. The code will perform calculation so that pressure and velocity are identical at corresponding nodes at these boundaries.

4.6.4 Blade, Hub and Shroud

The blade, hub and shroud are wetted surfaces and should be treated as walls with no slip boundary conditions

4.7 Post-Processing and Performance Calculation

Without post processing the numerical data from the CFD code, the data cannot be easily analyzed to allow conclusion for analysis. The goal of post processing of the calculation is to generate hydraulic contours, average velocity, pressure and loads/moments at specific locations. These averages allow evaluation of head, flow rate, power which can be used to calculate pump efficiency, which is ultimately the optimization parameter.

Graphical presentation of flow fields on meridional control surface and other control surfaces allow visualization of recirculation zones, stall phenomenon and secondary flows. Blade loading curves at various spanwise locations allow assessment of hydrodynamic loading. There are two types of averaging: mass average and area average. Mass average is used to satisfy the conservation equations which are discussed in chapter 4.2. Area average is used to quantify flow through the impeller, leakage though impeller/wear plate gap or flow through the entire machine.

4.7.1 Global Quantities

These equation describe the global calculation for important optimization parameters: theoretical head ψ_{th}, total pressure rise ψ_{imp} and hydraulic efficiency $\eta_{h,imp}$. The over-bars in Equations (4.5) and (4.6) represent mass average and the subscript 1 and 2 represent the streamwise location at inlet and outlet control surfaces. The streamwise location can ranges from 1 to 2 for the first component (impeller), 2 to 3 for the second (volute).

$$\psi_{th} = 2\left(\frac{\overline{(u_2.c_{2u})}}{u_2^2} - \frac{\overline{(u_1.c_{1u})}}{u_1^2}\right) \tag{4.5}$$

$$\psi_{imp} = \frac{2\left(\overline{p_{tot,2}} - \overline{p_{tot,1}}\right)}{\rho u_2^2} \tag{4.6}$$

$$\eta_{h,imp} = \frac{\psi_{imp}}{\psi_{th}} \tag{4.7}$$

The global flow rate in the pump can be determined from area average over control surface 1 or 2. Where c_n is the normal component of absolute velocity normal to control surface at inlet and outlet and N is number of component (if full machine is modeled, N=1).

$$Q_{net} = \sum_{A_{1,2}} c_n dA \cdot N \tag{4.8}$$

The static pressure rise:

$$\psi_{p,imp,pump} = \frac{2\left(\overline{p_{stat,2,3}} - \overline{p_{stat,1}}\right)}{\rho u_2^2} \tag{4.9}$$

Where, ‘imp’ implies impeller component calculation and ‘pump’ implies stage or complete machine calculation. The static and total flow energies can be calculated from Equations (4.10) and (4.11):

$$P_p = \psi_p \cdot Q_{net} \cdot \frac{\rho u_2^2}{2} \tag{4.10}$$

$$P_{tot} = \psi_{tot} \cdot \frac{P_p}{\psi_p} \tag{4.11}$$

Shaft power can be calculated from Equation (4.12):

$$P_{shaft} = \left| \sum_{A_{wall}} \left(F_x \cdot c_x + F_y \cdot c_y + F_z \cdot c_z \right) \right| \cdot \omega \tag{4.12}$$

A_{wall} is the calculated wall region at the Hub, Shroud, and Blade.

Static and total efficiency can then be calculated by:

$$\eta_p = \frac{P_p}{P_{shaft}} \tag{4.13}$$

$$\eta_{tot} = \frac{P_{tot}}{P_{shaft}} \tag{4.14}$$

4.7.2 Flow Visualization

Blade-to-blade plots can be used to visualize the flow patterns at constant span along the blade. Figure 4.8 is an example of blade-to-blade plot of velocity contours. Blade-to-blade plots can be constructed from a control surface at a constant span wise direction (0-1) along the blade. Blade-to-blade plots can be views in both x,y,z Cartesian coordinate system or in the blade-to-blade view which is a transformation from Cartesian coordinate system to M’, φ coordinate system.

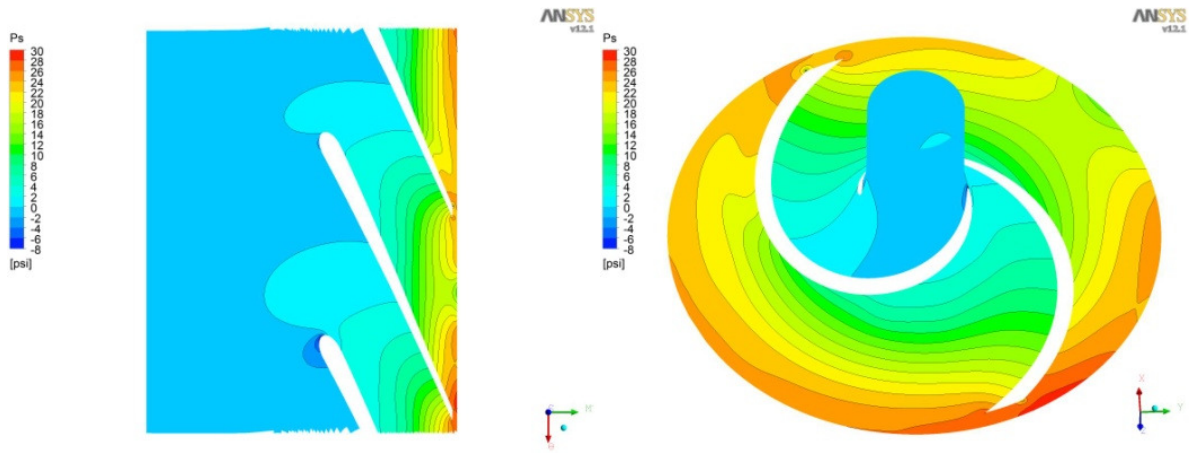

Figure 4.8: Pressure Field Visualization, Blade-to-Blade (left) and 50% Spanwise Cut surface (Right)

Meridional control surface is used to visualize meridional velocity. Meridional control surface is generated by taking the 3D passage boundaries and collapsing it in the Theta direction, forming a 2D passage outline on an axial-radial plane [**35**].

3D streamline plots can be used to track fluid particles in the impeller and locate or visualized recirculation zones or zones of stall fluid. 2D streamline on blade-to-blade spanwise surface can be used to visualize the degree of flow incident at LE or TE of the blade.

4.8 Numerical Uncertainties and Sources of Errors

4.8.1 Modeling Errors

Modeling errors are uncertainties in the physical model. Assumption such as roughness, true geometry of the impeller and turbulence models can result in modeling errors. Assumptions in the model such as incompressible one-phase flow can cause significant modeling errors if cavitation and two-phase flow are present.

4.8.2 Model Simplification

Because of limitation of computer resources models must be simplified to reduce computational time. These simplifications can result in model simplification errors. An example of model simplification error can arise when geometrical features such as fillets are ignored in the model.

4.8.3 Numerical Errors

There are two types of numerical errors: discretization errors and solution errors. Discretization error is the difference between the exact solution of the equation which is solved and the discretized equations. This type of error is normally determined by the order of the discretization. The solution error is the difference between the numerical solution and the actual solution obtained. Solution error consists of residuals and rounding errors. Numerical discretization errors can be quantified using the Richardson Extrapolation method [**36**].

Chapter 5: Experimental Measurement of Pump's Performance

This chapter discusses the experimental procedures and setup which have been developed for performance measurement of the OEM impeller as well as the Redesigned impeller. Two methods are used to measure the pumps performance: conventional flow base method and the thermodynamic method. The thermodynamic method will be discussed in Chapter 8. Uncertainty analysis is used to evaluate the error in the experimental results. Performance curves for both the OEM and Redesigned impeller are shown in this chapter.

5.1 Experimental setup

Figure 5.1 shows the process flow diagram for the pump loop. The loop consist of two 4,000 L storage tanks (TK-001 and TK-002), suction and discharge pressure sensors (PT-001 and PT-002), an Allis Chalmers PWO Pump 6"x3"x14" Paper and Pulp Process Pump (P-001), a magmatic flow meter (FE-001) and discharge motor operated valve (MOV-002). The pump is coupled to a TECO Westinghouse OPTIM He Plus motor and is power by a variable frequency drive (VFD). The motor power is measured by a BC Hydro power meter which measures real power (P_M), reactive power, complex power, apparent power, and phase of Current.

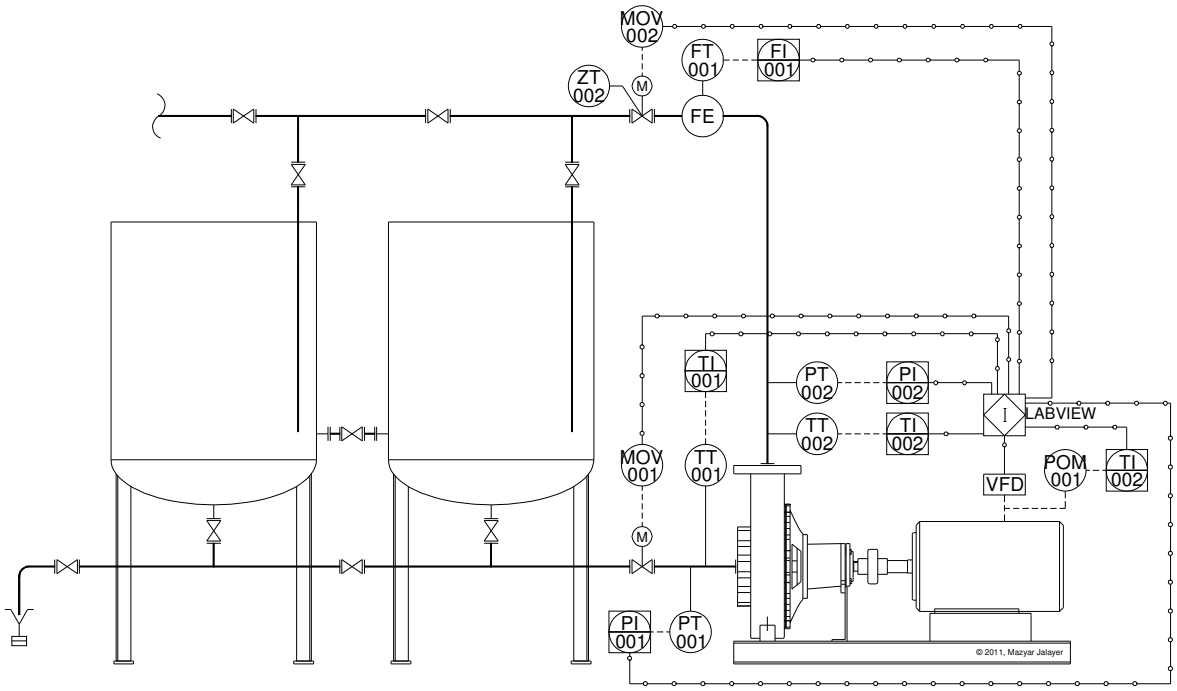

Figure 5.1: Pump Loop Piping and Instrumentation Diagram

All measurements and control are done in Labview software. The program allows automatic push-button pump curve generation.

5.2 Pump Efficiency Determination from Pressure and Flow Rate

Figure 5.2 shows a control volume around the pump. Total differential head of the pump (ΔH_{tot}) is a combination of static head (H_p), dynamic velocity head (H_d), and elevation of pressure sensors (El), is subtracted from the inlet (1) and outlet (2). This is shown in Equation (5.1).

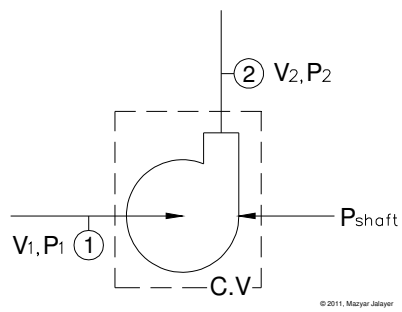

Figure 5.2: Control Volume for 1-D Energy Balance (Flow-based Method)

$$\Delta H_{tot} = \left(H_d + H_p + El\right)_{|2} - \left(H_d + H_p + El\right)_{|1} \tag{5.1}$$

The static and dynamic heads at inlet and outlet can be represented by Equations (5.2) and (5.3) respectively.

$$H_p = \frac{p}{\rho g} \tag{5.2}$$

$$H_d = \frac{V^2}{2g} \tag{5.3}$$

P is the pressure and V is the average velocity. The differential total head can be represented by measured process condition at the inlet and outlet.

$$\Delta H_{tot} = \left[\frac{p_2}{\rho \cdot g} + \left(\frac{Q}{0.25 \cdot \pi \cdot ID_2}\right)^2 \cdot \frac{1}{2g}\right] - \left[\frac{p_1}{\rho \cdot g} + \left(\frac{Q}{0.25 \cdot \pi \cdot ID_1}\right)^2 \cdot \frac{1}{2g}\right] + \Delta EL \tag{5.4}$$

Here the friction loss from the pump's inlet to its outlet is ignored because it is very small and negligible. The shaft power is obtained from motor efficiency and motor input power which is measured from POM-001.

$$P_{shaft} = \eta_{motor} \cdot P_{motor} \tag{5.5}$$

The pumps hydraulic power is obtained from:

$$P_h = \Delta H_{tot} \cdot Q \cdot \rho \cdot g \tag{5.6}$$

And the pump's efficiency can be calculated form Equation (5.7).

$$\eta_{pump} = \frac{P_h}{P_{shaft}} \tag{5.7}$$

The pump's total head coefficient can be calculated by non-dimensionalizing the total head by the circumferential velocity head:

$$\psi_{pump,tot} = \frac{2g \cdot \Delta H_{tot}}{{u_2}^2} \tag{5.8}$$

Where the outlet circumferential velocity can be calculated from:

$$u_2 = \frac{D_2}{2}\omega \tag{5.9}$$

Similarly the static head coefficient can be calculated from:

$$\psi_{pump,p} = \frac{2g \cdot (\Delta H_p + \Delta EL)}{{u_2}^2} \tag{5.10}$$

5.3 Pressure Calibration

The suction and discharge pressure sensors were calibrated using a mobile pressure calibration device which applies a fix known pressure to the sensor and the voltage is measured and a plot of voltage versus pressure is used to define a calibration fit. Figure 5.3 show the calibration equations for suction and discharge pressure sensor.

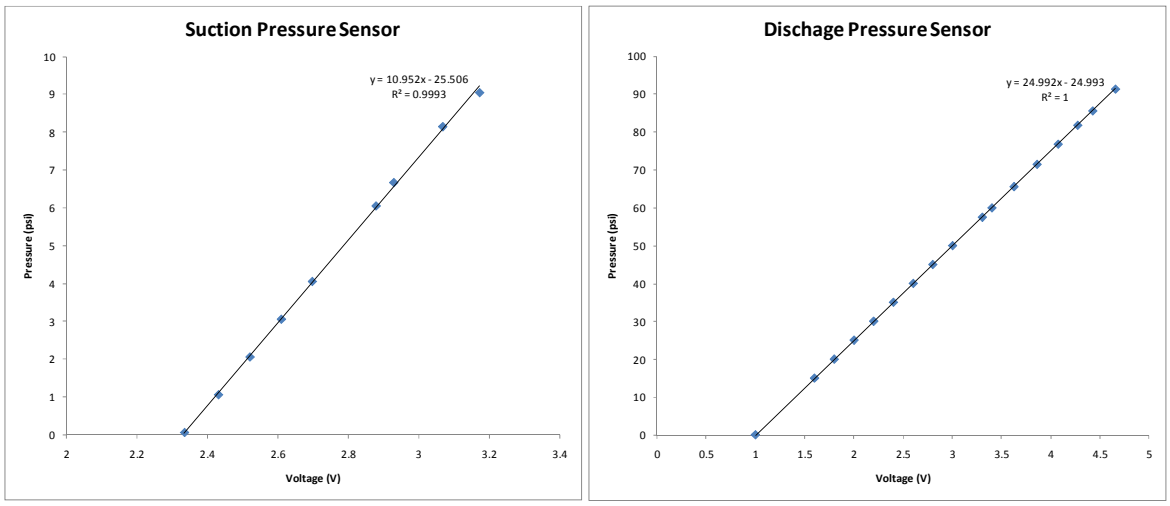

Figure 5.3: Calibration Curves for Suction (Left) and Discharge (Right) Pressure Sensors

5.4 Error analysis

The uncertainty in calibration curve fitting can be obtained using standard error of the fit:

$$S_{xy} = \sqrt{\sum_{i=1}^{n} \frac{(y_i - y(x))^2}{n - (m+1)}} \tag{5.11}$$

Here n is the number of measurement used in the calibration and m is number of variables (in this case 2 for linear fit). For negligible random errors in the independent variable x, a confidence interval of curve fit (y(x)) due to random scatter about the fit, is estimated from:

$$U_{fitt} = \pm t_{p=95\%} \frac{S_{xy}}{\sqrt{n}} \tag{5.12}$$

The uncertainties associated with each measured valuable (p_1, p_2, Q, P_m), is estimated from standard deviation of measured sample.

$$U_{p1,p2,Q,P} = \pm t_{p=95\%} \frac{\sigma_{p1,p2,Q,P}}{\sqrt{n}} \tag{5.13}$$

The accumulated total uncertainty is then calculated from:

$$U_{Tot,(p1,p2,Q,P)}{}^2 = U_{fitt}{}^2 + U_{p1,p2,Q,P}{}^2 \tag{5.14}$$

The uncertainty for total differential head is then calculated from propagation of error.

$$U_{\Delta H}{}^2 = \left(\frac{\partial \Delta H}{\partial p_1} U_{Tot,p1}\right)^2 + \left(\frac{\partial \Delta H}{\partial p_2} U_{Tot,p2}\right)^2 + \left(\frac{\partial \Delta H}{\partial Q} U_{Tot,Q}\right)^2 \quad \textbf{(5.15)}$$

Similarly the uncertainty for the efficiency is estimated from efficiency function.

$$U_{\eta}{}^2 = \left(\frac{\partial \eta}{\partial p_1} U_{Tot,p1}\right)^2 + \left(\frac{\partial \eta}{\partial p_2} U_{Tot,p2}\right)^2 + \left(\frac{\partial \eta}{\partial Q} U_{Tot,Q}\right)^2 + \left(\frac{\partial \eta}{\partial P} U_{Tot,P}\right)^2 \quad \textbf{(5.16)}$$

5.5 Pump Performance

This section shows the results for pump performance monitoring based on flow measurement. Both the OEM and the Redesigned impeller are tested. For development of the OEM impeller, please refer to Chapter 7.1.

5.5.1 Performance of Existing OEM Pump

The head and Efficiency curves for OEM impeller are shown on Figure 5.4. BEP is around $\phi_{OEM} = 0.032$, $\psi_{OEM} = 0.78$ and $\eta_{OEM} = 59.2\%$ which corresponds to flow rate of ~400 gpm and total head of ~70 ft of water. The error bars in the figure are based on experimental error analysis which was discussed in section 5.4. The error bars show the level of uncertainly in the data.

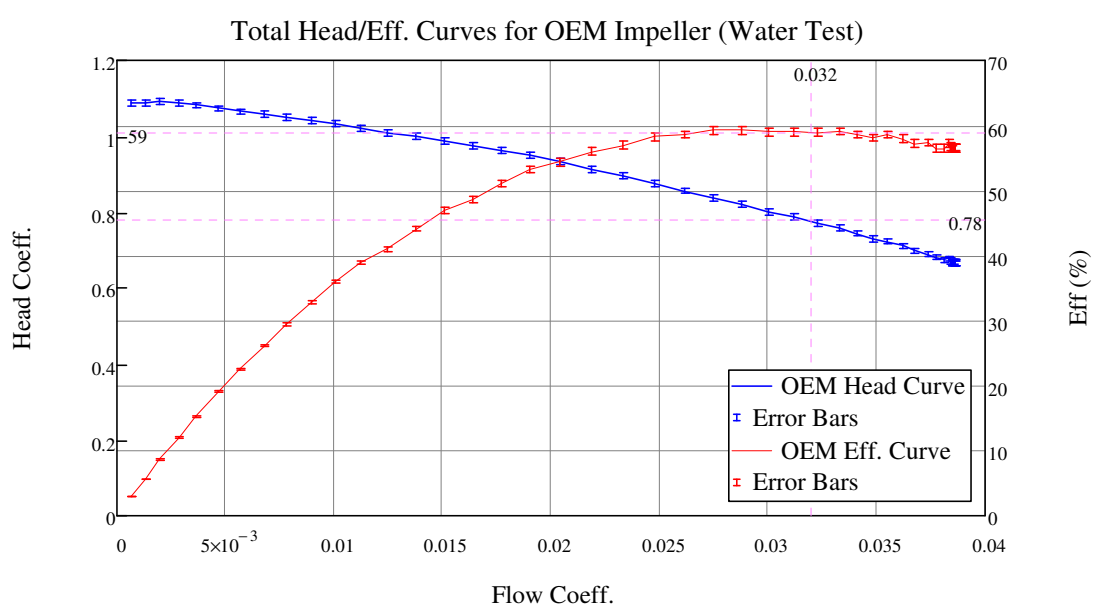

Figure 5.4: Pump Loop Performance Curves (OEM Impeller)

5.5.2 Performance of Redesigned OEM Impeller

The head and Efficiency curves for the redesigned impeller are shown on Figure 5.5. BEP is around $\phi_{Red} = 0.036$, $\psi_{Red} = 0.89$ and $\eta_{Red} = 78.8\%$ which corresponds to flow rate of ~450 gpm and total head of ~78 ft of water. The error bars in this figure are based on experimental error analysis which was discussed in section 5.4. The error bars show the level of uncertainly in the data.

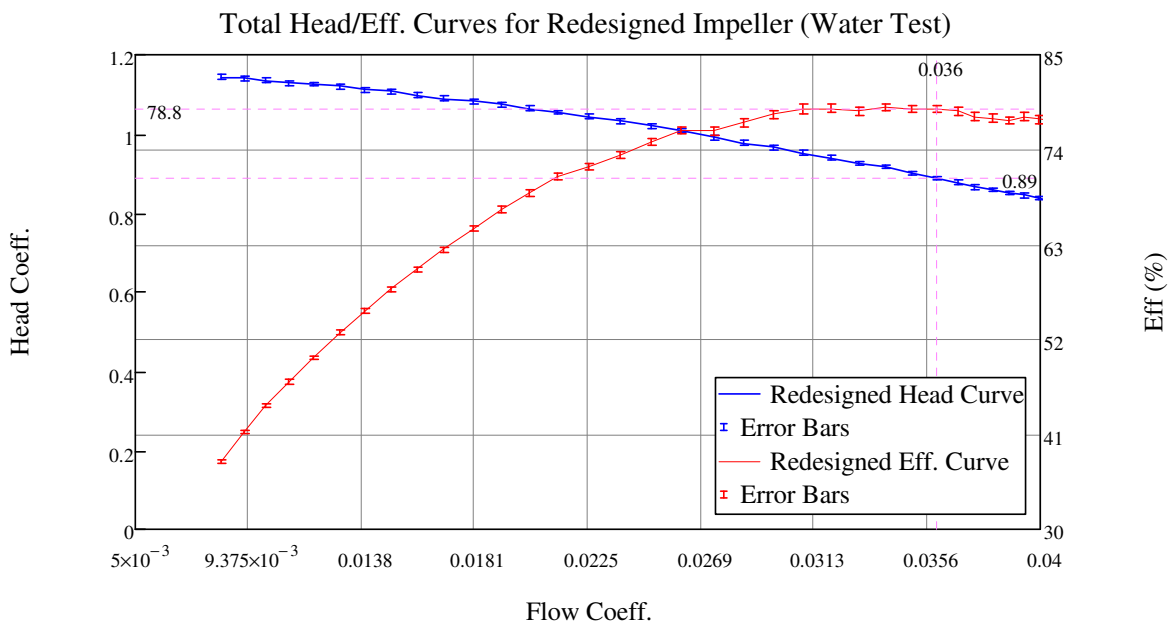

Figure 5.5: Pump Loop Performance Curves (Redesigned Impeller)

Chapter 6: Numerical Validation

This chapter discusses the procedures and methods for numerical calculation and validation of the CFD process. The CFD process is used to evaluate individual performances for the series of impeller that are developed with the Redesign model. Grid convergence is evaluated by varying structured grid control parameters. A residual sensitivity study is performed to evaluate the sensitivity of numerical solution to solver residual target. The robustness of both the component and stage calculations is evaluated with experimental pump loop data.

6.1 Geometry

Figure 6.1 show a 3D surface model of the OEM impeller which is constructed from 3D laser scan data. Because of the complexity associated with the blade shape, hub and shroud profiles, the geometrical data that can be measured directly from the impeller model is limited.

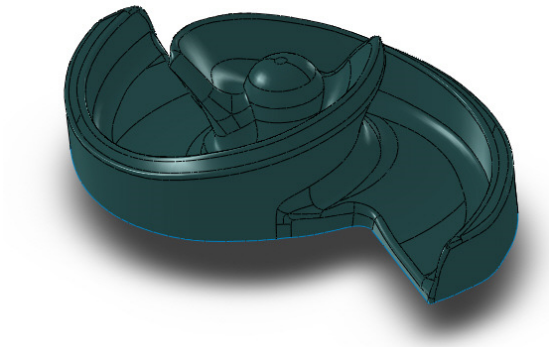

Figure 6.1: 3D Model of OEM Impeller Laser Scan Data

The OEM impeller is 14in in diameter and has two vanes. The wrap angle ($\varphi_{R,\theta}$ = 280°) can be measured in CAD relatively easily. However the blade angle and its distribution along the hub or shroud profile cannot be measured by simple means. For this reason, specialized software (ANSYS BladeGen) which is used for design of turbomachinery is utilized. This is done by importing the 3D curves from the CAD model to BladeGen. The geometry of the impeller after import into the software is shown in Figure 6.2.

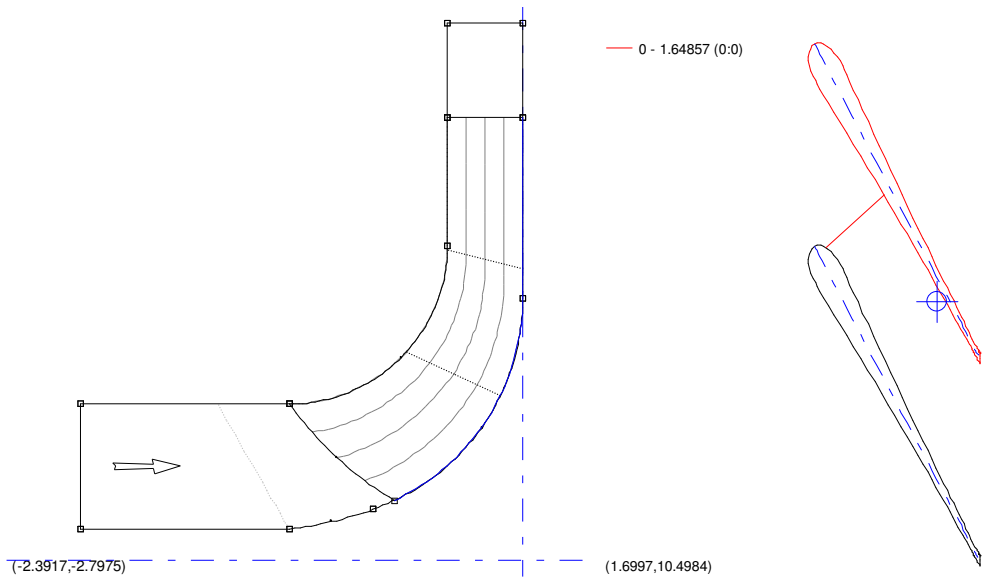

Figure 6.2: Meridional Curve (Left) and Blade-to-Blade (Right) for OEM Impeller

The meridional profile is calculated by collapsing hub and shroud profiles onto the R-θ plane. The blade-to-blade shows that the blade has a constant beta angle of 27.7°.

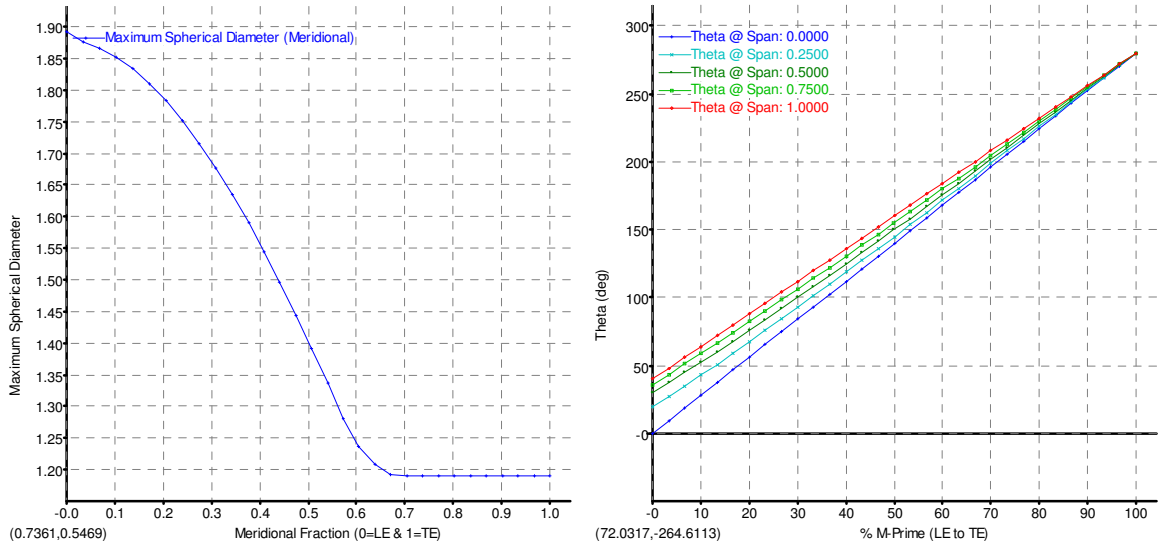

Figure 6.3: OEM Impeller Maximum Spherical Diameter (Left) and Theta Distribution Curves (Right)

The program is able to generate a series of plots showing the change in wrap angle distribution at different location along the blade spanwise direction. The blade has an offset angle of about 46° at the shroud. This angle is used to accommodate the extension of LE into the inlet region.

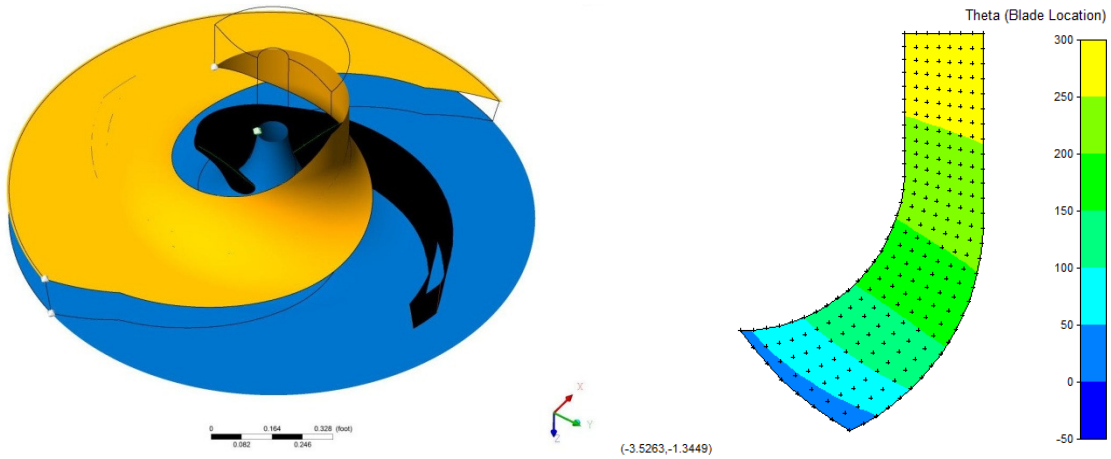

Figure 6.4: OEM impeller 3D-Parametric Model (Left) and Theta Spanwise Distribution Plot (Right)

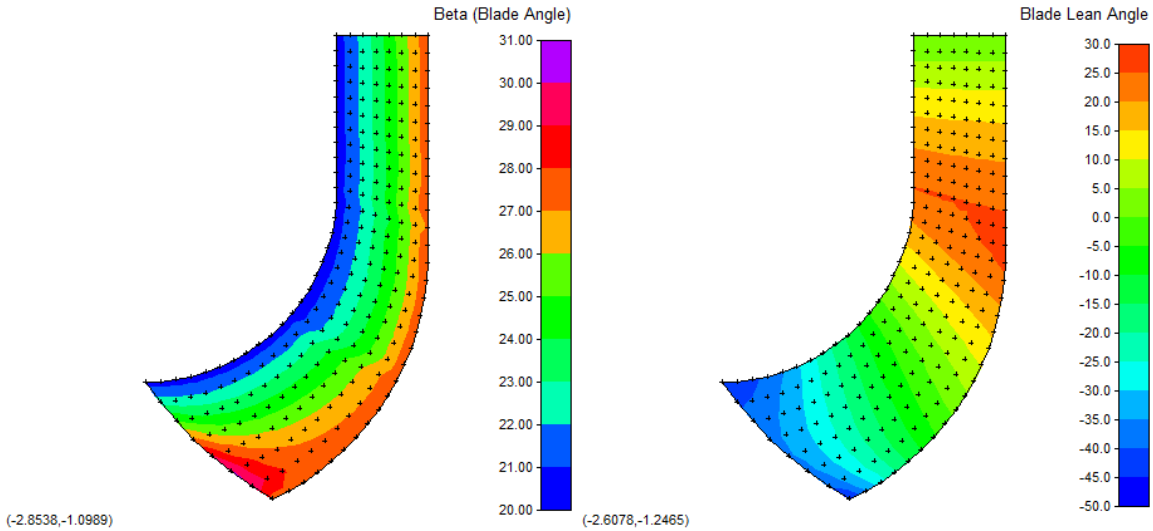

Figure 6.5: OEM Impeller Beta Spanwise Plot (Left) and Blade Lean Angle Plot (Right)

Negative lean angle at LE, the offset angle between the shroud and hub blade locations, can be seen from the lean angle distribution plot, Figure 6.5. Positive lead angle is observed midway between the LE and the TE.

6.2 Grid Generation and Convergences

The grid for the impeller is developed in specialized software called TurboGrid. TurboGrid is used specifically for turbomachinery. It enables the user to generate very high quality structured mesh. The topology for the OEM impeller is shown in Figure 6.6. The topology consists of H/J/C/L-grids with O-grids around the blade. J-grid and H-grid are used at LE and

TE of the blade. C-grid and L-grids are used at periodic mesh interfaces and in the shroud blade clearance.

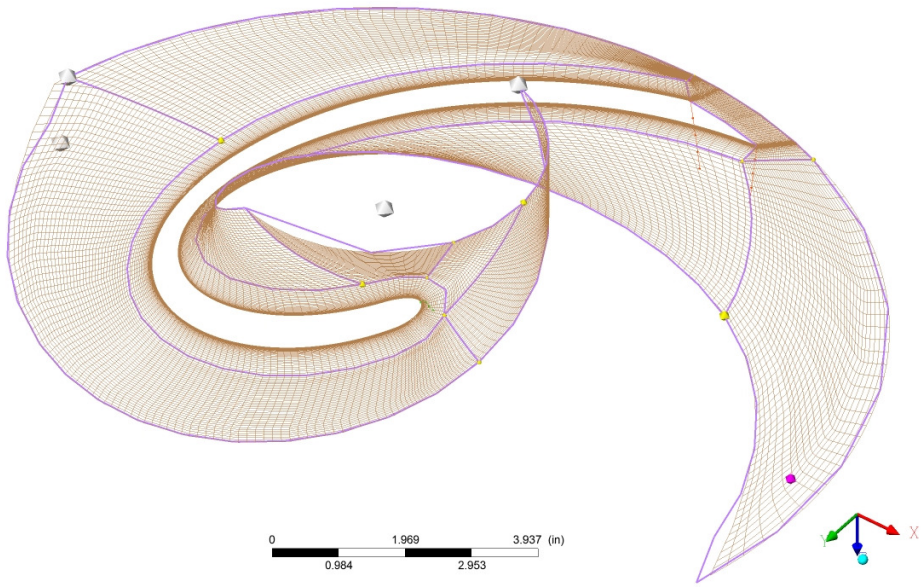

Figure 6.6: OEM Impeller Mesh Topology

Table 6.1 shows various mesh control parameters which are used to control the refinement of the mesh and the target numbers of nodes. Parameterization of the mesh allows the mesh to be used effectively in a mesh convergence study so that only areas which are essential to the precision of the calculation are refined rather the entire domain.

	No.4	**No.5**	**No.6**	**No.7**
O-grid width factor	1.2	1.22	1.24	1.26
O-grid number of elements	10	20	30	40
O-grid y+	5	10	12	10
Total spanwise blade element No.	20	40	65	80
Constant spanwise blade element No.	14	30	35	30
Span y+ for hub	5	7	8	9
Span y+ for hub	5	7	8	9
Target nodes	1,200,000	1,400,000	1,600,000	2,000,000
Actual No. of nodes	1,235,395	1,467,673	1,634,094	2,062,045

Table 6.1: Grid Parameter Data

Figure 6.7 shows pump head curves for mesh 1-7. Note that the mesh refinement increases with increasing mesh number, with mesh number 7 being the densest mesh. This figure is generated by varying the mass flow BC at the impeller outlet and calculating the total head using the post processing calculations which are described in Chapter 4.7. This calculation is performed for each mesh until mesh convergence is observed.

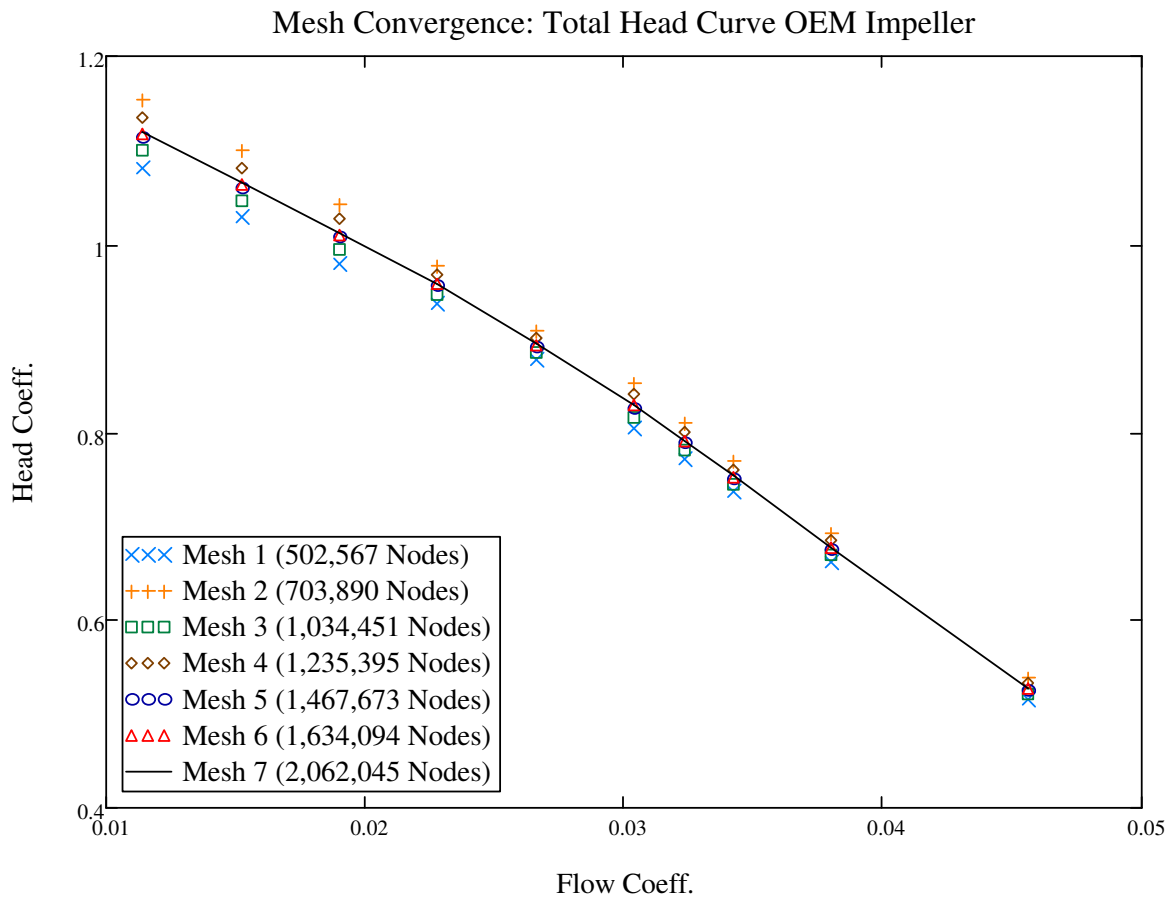

Figure 6.7: Mesh Convergence Graphs (Mech No. 1 to 7)

As it can be seen from Figure 6.7 all mesh converge onto mesh 7 which has 2,062,045 nodes. There seems to be no significant deviation from the result obtained from mesh number 6 and 7. For this reason and in order to reduce computational time, mesh 6 control parameters are used to evaluate all CFD calculations in this work.

Figure 6.8 shows the final OEM impeller mesh (with Mesh 6 control parameters). Note that this mesh is a 3D fluid domain and only the blade and hub surface meshes are show. As it can be seen from the figure, this mesh is very fine at the viscous sub-layer. Far field fluid is meshed with coarser mesh to reduce calculation computation time. Corse mesh is used to extend the inlet and outlet in order to accommodate the extension of recirculation zones into these regions at part load.

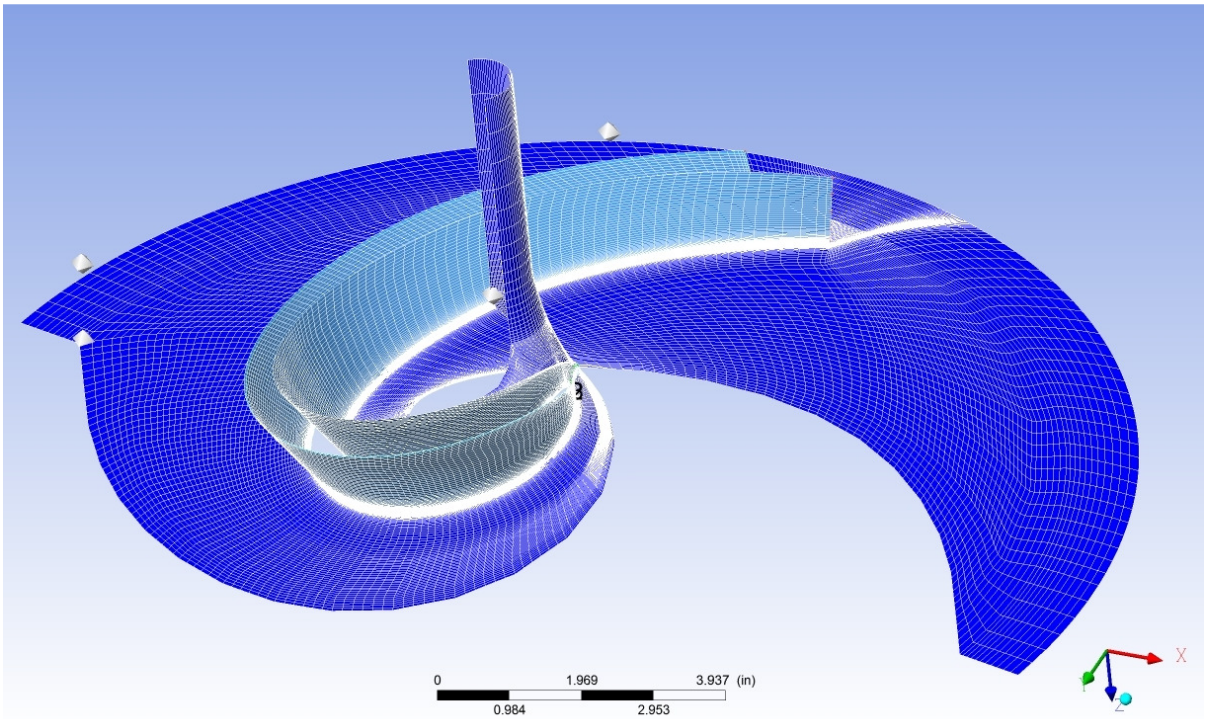

Figure 6.8: OEM Final Mesh (Mesh No. 6)

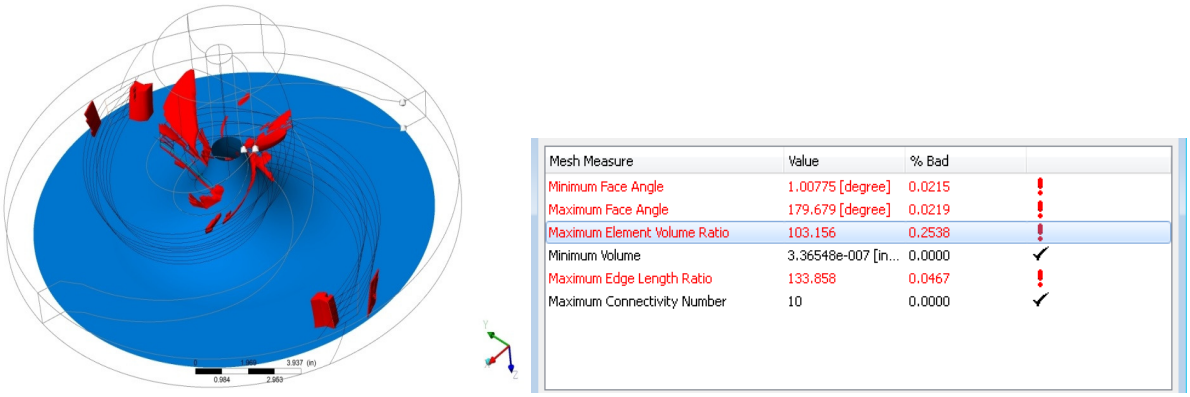

Mesh Measure	Value	% Bad	
Minimum Face Angle	1.00775 [degree]	0.0215	!
Maximum Face Angle	179.679 [degree]	0.0219	!
Maximum Element Volume Ratio	103.156	0.2538	!
Minimum Volume	3.36548e-007 [in...	0.0000	✓
Maximum Edge Length Ratio	133.858	0.0467	!
Maximum Connectivity Number	10	0.0000	✓

Figure 6.9: OEM Impeller Mesh Quality and Mesh Measurements

Figure 6.9 shows the 3d plot of impeller mesh with potential problems areas. The mesh is measured for minimum/maximum face angle, element volume ratio, minimum volume, and maximum edge length ratio. Because of relatively large wrap angle of the OEM blade the mesh displays potential problem areas where CFX solver would have problems with. However, despite the short falls of the relativity small number (<0.25%) of problem areas, this mesh is of very high quality and is acceptable for calculation.

6.3 Residual Sensitivity Study

Residual sensitivity study is used to predict the optimal convergence criteria for the CFD calculation. Table 6.2 shows the calculated output parameters such as efficiency, static head, mass flow and shaft power. Note that although the mass flow is an input parameter (outlet BC of the impeller), it can also be calculated by area average calculation described in Chapter 4.6.2. The sensitive study shows that there is relatively small difference between for convergence criteria with RMS residual of 1e-6 versus 1e-7. For this reason and in order to reduce the calculation time, RMS residual of 1e-6 is used as convergence criteria.

RMS Residuals	CPU Time per/Calc [s]	Calculated Static Efficiency	Calculated Static Head [ft]	Calculated Mass Flow [kg/s]	Shaft Power [kW]
1E-4	5.366E+02	63.554	73.102	25.191	8.661
1E-5	9.562E+03	63.955	73.002	25.185	8.587
1E-6	2.810E+04	64.286	72.906	25.186	8.538
1E-7	8.335E+05	64.289	72.910	25.186	8.538

Table 6.2: Residual Sensitivity Study

6.4 Component Calculation

This section demonstrates the component calculation for the OEM impeller. The results are compared with the OEM experimental data, Chapter 5.5.1.

6.4.1 Component Calculation Preprocessing

Figure 6.10 shows the post processing for the component calculation. Here only one fluid passageway will be analyzed by applying periodic BC mid pitch between the vanes. The inlet is set to a constant average static pressure of 0 atm. The calculation reference pressure is set to 1 atm. The domain is rotating at motor synchronous speed of 1150 RPM. The blade surfaces and the hub are stationary wall with no slip BC. The shroud, however, is rotating counter clockwise with no slip BC to simulate an open impeller. The outlet is set to a variable mass flow which varies from 150 gpm to 600 gpm.

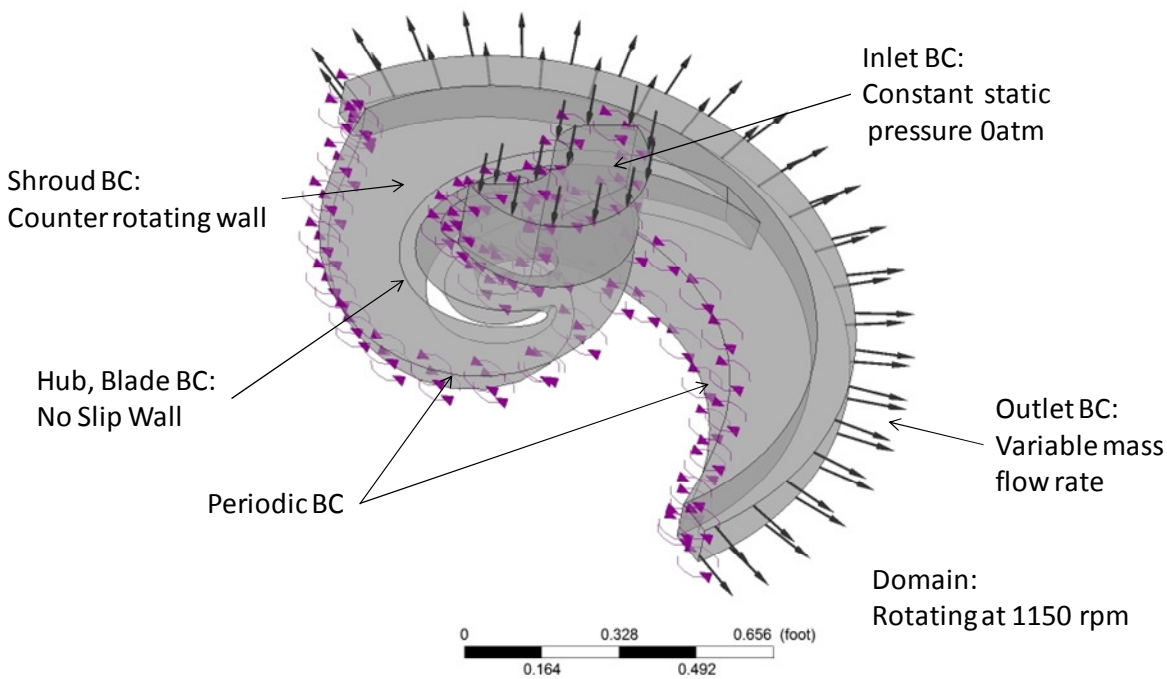

Figure 6.10: Component Calculation Boundary Conditions

6.4.2 Component Calculation Result

Figure 6.11 shows the static pressure distribution at 50% blade span. It can be seen from the figure the pressure inside passageways increases gradually from inlet to the outlet. However, because of the relatively large wrap angle, this causes large pressure variation over the blade. Also the pressure on the suction side (SS) of the blade is relatively constant (low variation from LE to midway point between the LE and TE). However, the pressure on the pressure

side (PS) of the blade varies dramatically from LE to the TE. This large pressure gradient causes substantial flow separation on the PS of the blade.

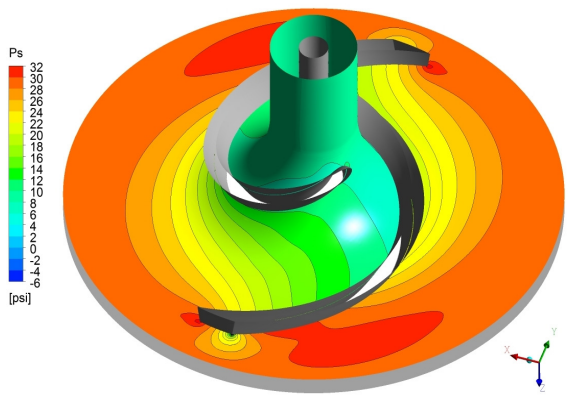

Figure 6.11: OEM Impeller Static Pressure Plot Spanwise Cut (Component Calculation)

Another important feature, blade loading pressure distribution, is seen in Figure 6.12,. The large blade thickness at the TE and large variation between the pressure on the SS and PS of the blade cause pressure surges at the TE.

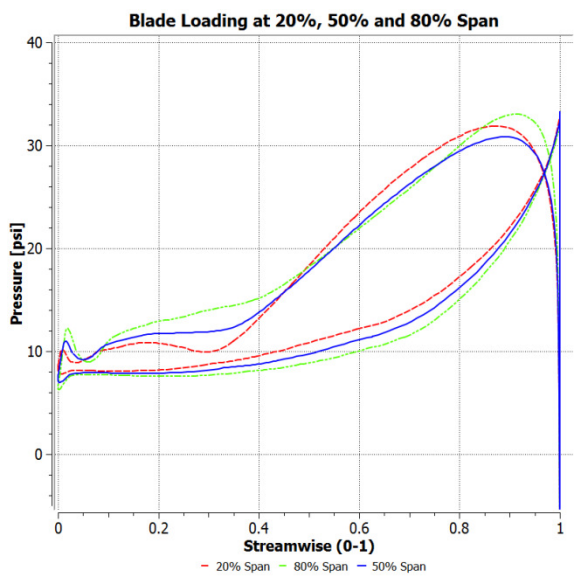

Figure 6.12: Blade-to-Blade Loading OEM Impeller

The result of these large pressure gradients over the blade is flow separation and zone of stalled fluid. This phenomenon can be seen in Figure 6.13, 3D streamline flow inside OEM

impeller. The result of flow separation can be seen even when operating at BEP because of relatively low number of vanes.

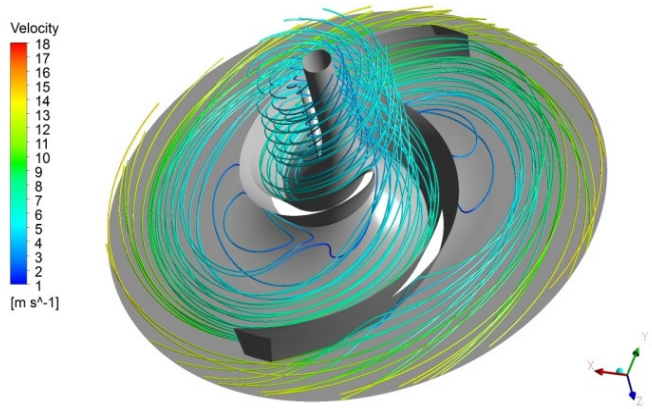

Figure 6.13: 3D Stream Line Flow inside OEM Impeller at BEP

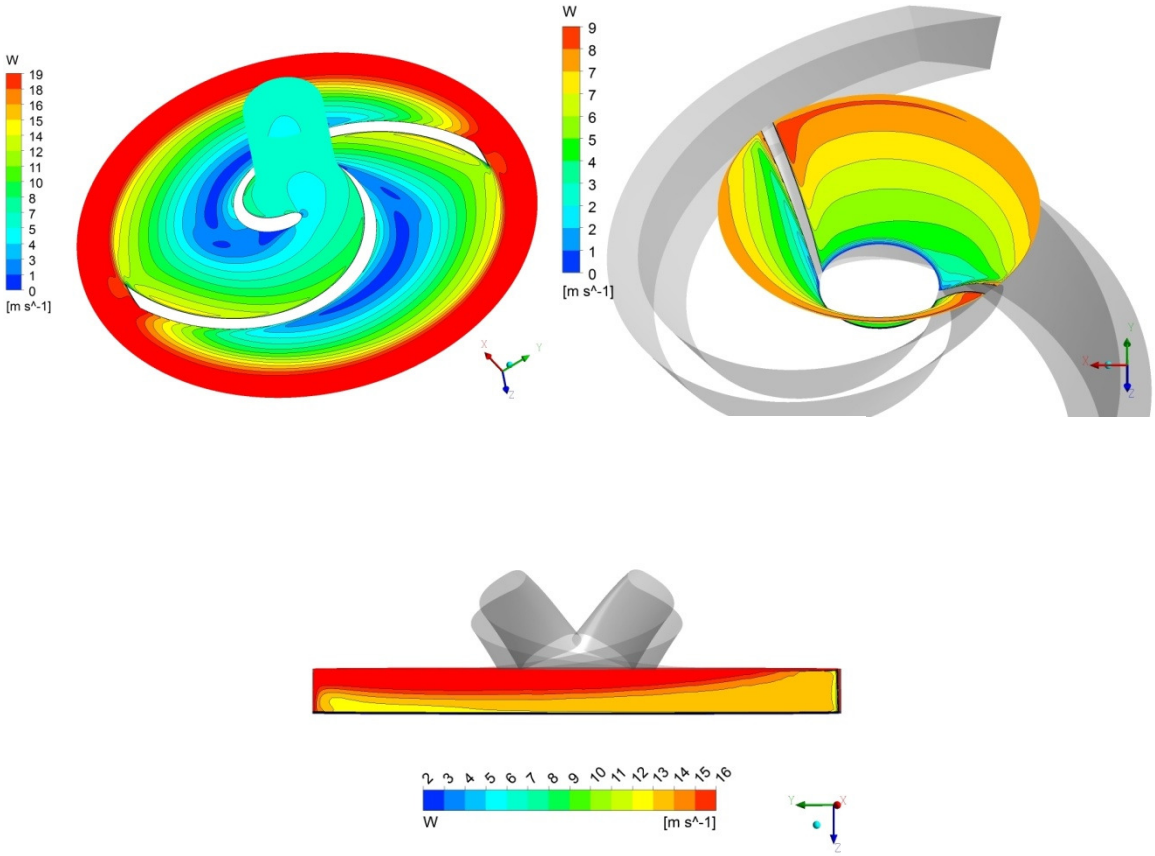

Figure 6.14: OEM Flow Visualization (Component Calculation)

Figure 6.14 shows various plots of the fluid flow inside the impeller. The flow at the LE can be seen from the top right figure. The relative velocity variation from the hub to shroud is substantial. This may be caused by the secondary flows which are discussed in Chapter 4.3. The figure on the top left show the zones of stall fluid which tend to partially block the fluid flow inside the impeller by reducing the available flow area. The figure on the bottom shows the variation in relative velocity at the outlet. These variations are the result of uneven pressure gradient between the SS and PS of the blade resulting from a low number of vanes.

With the results of flow visualization it is easy to see why this impeller exhibit low efficiency at peak performance. The low number of vanes does not guide the fluid well inside the impeller which results in complex fluid flow and velocity patterns. To compensate for the low number of vanes, the designers of this impeller had to increase the blade wrap angle which in turn causes the fluid to separate because of large uneven pressure gradient on the SS and PS. These large pressure gradients result in large blade loading which is essentially one of the factors that determines the impeller power consumption and hence efficiency.

Figure 6.15 shows impeller head curve for OEM impeller. The component calculation is shown in red and the pump loop experimental results are shown in blue. The CFD component calculation was able to predict the head performance at BEP and at full load. However, large deviation can be seen between the experimental data and the CFD calculation at partload. This is because as fluid flows through the impeller, it is restricted by the large outlet pressure, which causes recirculation inside the impeller. In this region the fluid flow is very complex and the turbulence model may not be appropriate for predicting the fluid flow accurately.

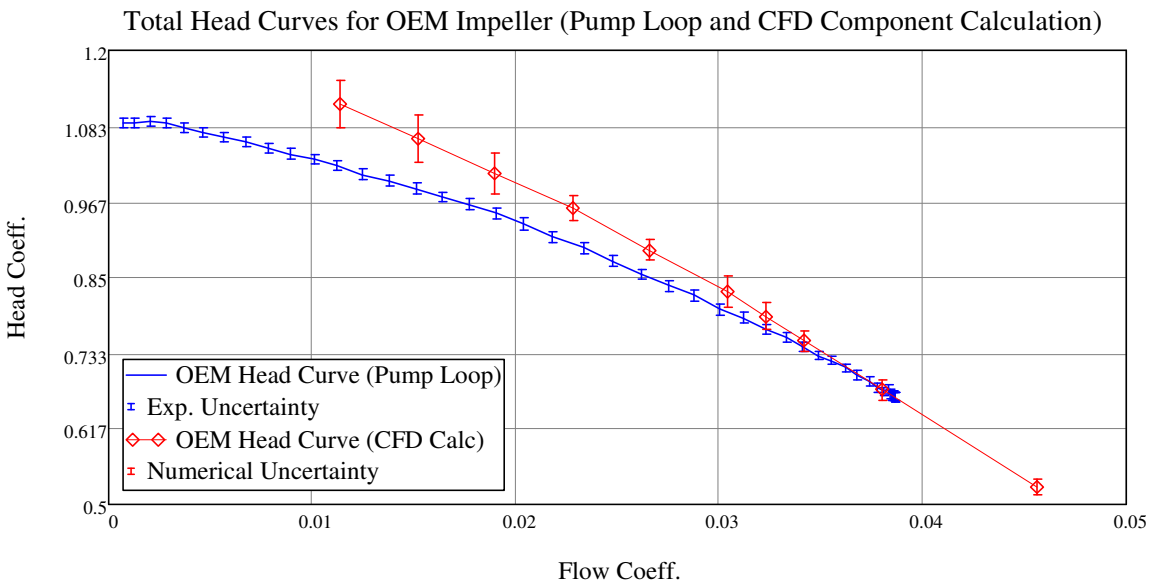

Figure 6.15: OEM Component Calculation Total Head Curve

The calculated efficiency curve for the OEM pump is compared with the experimental date in Figure 6.16. The CFD over-predicted the impellers performance at BEP by 7%. The performance at partload was under-predicted. This phenomenon is due to complex fluid flow inside the impeller at partload.

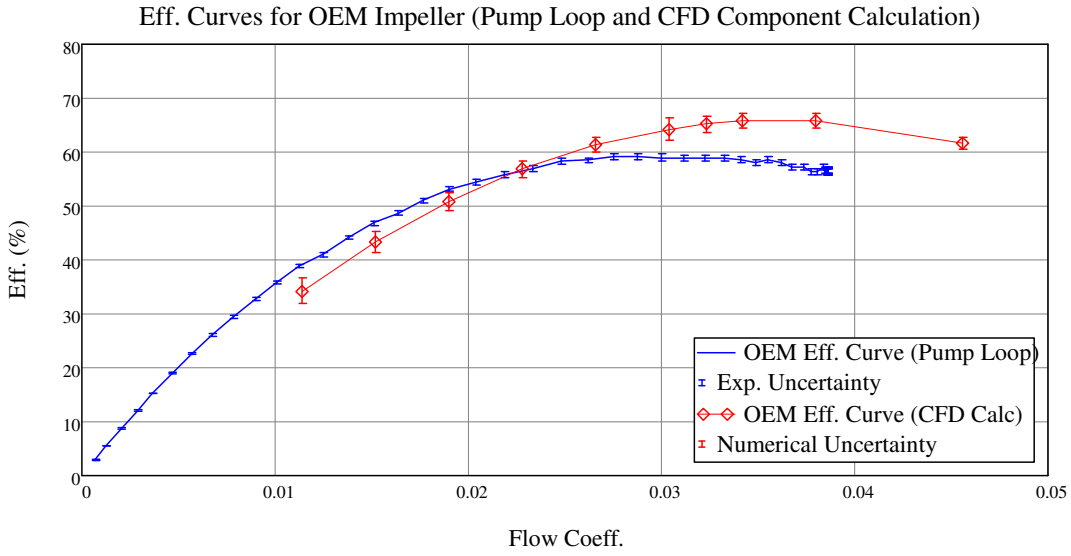

Figure 6.16: OEM Component Calculation Efficiency Curve

6.5 Stage Calculation

The component calculation is computationally inexpensive and it can be used to estimate the performance of an impeller at the BEP. However, in order to evaluate and compare performance of various impellers, a more precise calculation is required. As explained in pervious chapters, there is complex flow interaction between the impeller and the volute, especially at partload where the fluid tends to recirculate inside the impeller. For this reason a stage calculation (calculation of entire machine) is performed to validate the CFD process.

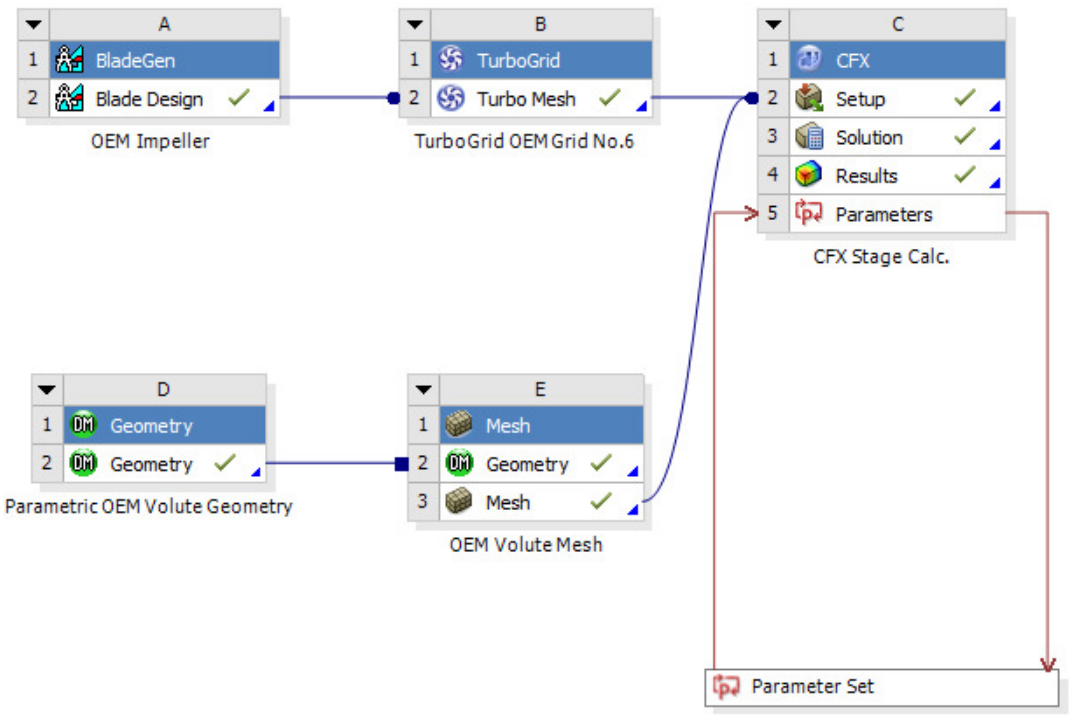

Figure 6.17: Stage Calculation ANSYS WorkBench Simulation Work Flow

Figure 6.17 shows the ANSYS Workbench CFD simulation. The volute domain is meshed using ANSYS Icem. The volute mesh is an unstructured mesh with mesh refinement at the walls to resolve the viscous sub-layer. The mesh is further refined at the volute cut water to resolve the fluid flow in this section. The nodes at interface between the impeller outlet and the volute inlet are aligned with the impeller nodes to reduce computation time associated with in-between-node interpolation.

6.5.1 Stage Calculation Pre-Processing

Figure 6.18 shows the pre-processing BC for the stage calculation. The calculation consists of two domains: impeller and the volute. The impeller domain is analyzed in the rotating frame of reference and therefore is rotating at pump motor synchronous speed, 1150 rpm. The volute is stationary domain with no slip BC at the wall surfaces. The fluid flows out from a rotating domain (impeller) into the stationary domain (volute). For this reason a domain interface is selected between the impeller outlet and the volute inlet. In this case a simple frozen rotor mixing model is utilized. Mixing models are discussed in more detail in Chapter 4.4.2. All other BCs are similar to the BCs described in Chapter 6.4.1, component calculation.

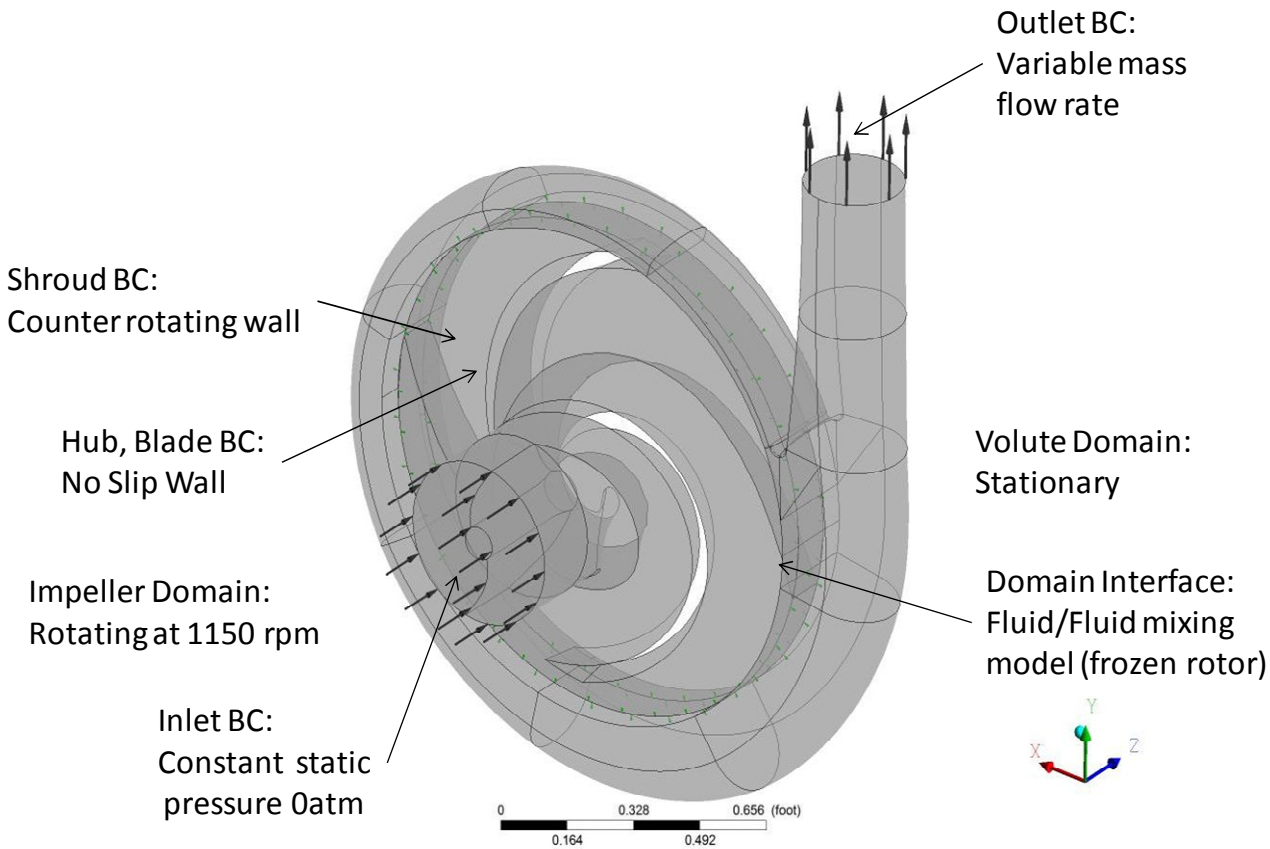

Figure 6.18: Stage Calculation Boundary Condition

6.5.2 Stage Calculation Result

The fluid flow inside the pump is none steady and pulsatile. For this reason the angular position of the impeller to the volute cut water determines the head which is generated by the pump. These variations in head are very difficult to observe in pump systems because the pressure fluctuations are dampened out by the piping arrangement and the tank level. Depending on the speed of the pump and the pressure transmitter sampling rate, the fluctuations may not be captured properly. In any case, in the experimental performance measurement, an average pressure reading is taken for efficiency calculation.

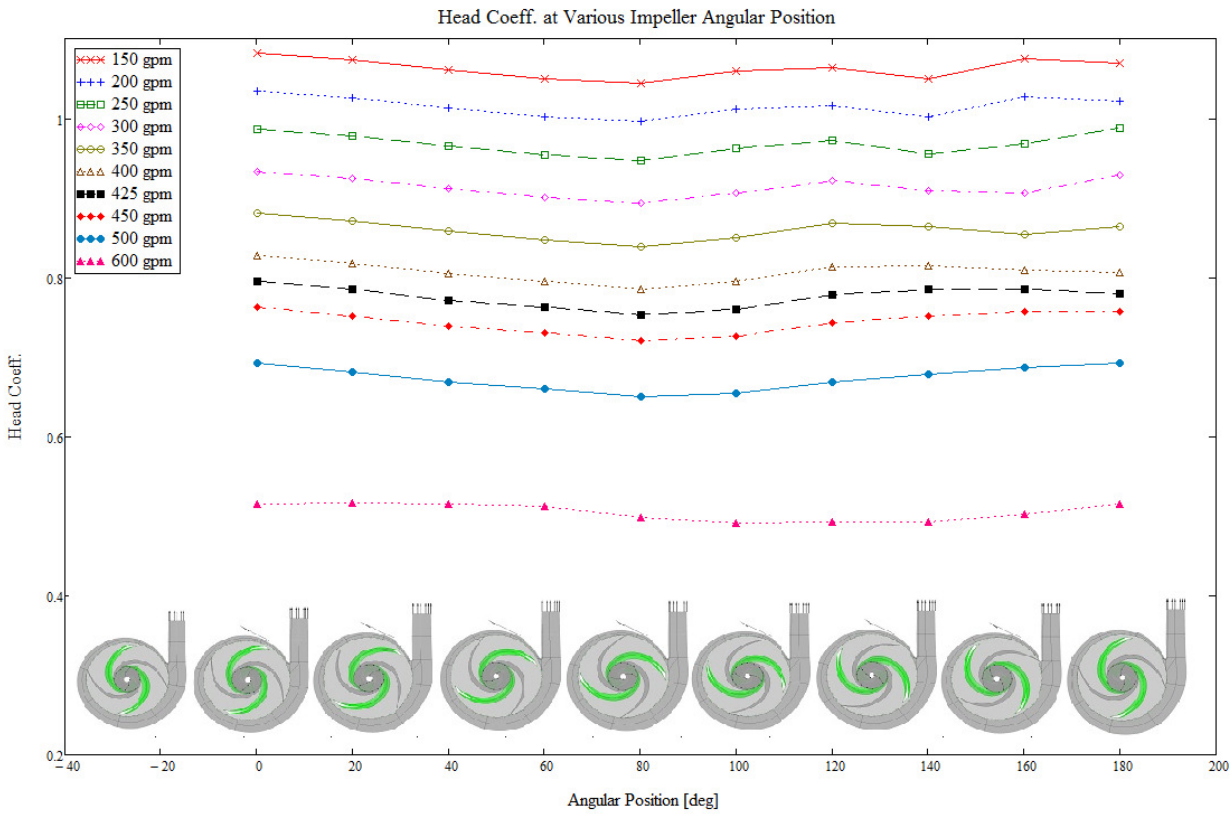

Figure 6.19: OEM Stage Calculation, Angular Position and Head Coeff.

Figure 6.19 shows the CFD stage calculation results for the OEM impeller. The head coefficient is plotted against the impeller angular position with respect to the cutwater. This plot is repeated for various operating points from 150-600 gpm. The mesh is moved (rotated) slightly for various outlet flow BCs. As can be seen from this figure, the flows though the pump is unsteady and the calculated head depends on the angular position of the impeller. In

order to generate a pump curve the values of head are averaged over one 1/z revolution. In the case of the OEM impeller the head coefficients are average from 0° to 180°.

$$\psi_{\Lambda} = \frac{1}{2\pi/z}\int_{0}^{2\pi/z} \psi(\theta)\, d\theta \tag{6.1}$$

Figure 6.20 shows the head curve for the stage calculation along with the associated plot of head pulsation with respect to the angular position (every 2°) for various flow operating points. The x-axis of the curves for individual operating points is in angular unit rads. The stage calculation predicts the pump's head performance accurately for various flow rates around the BEP (250gpm to 500gpm). At 150-250gpm range there are some slight variation between the experimental data and the calculated values. This may be caused by the complex flow behavior which is inherent at partload.

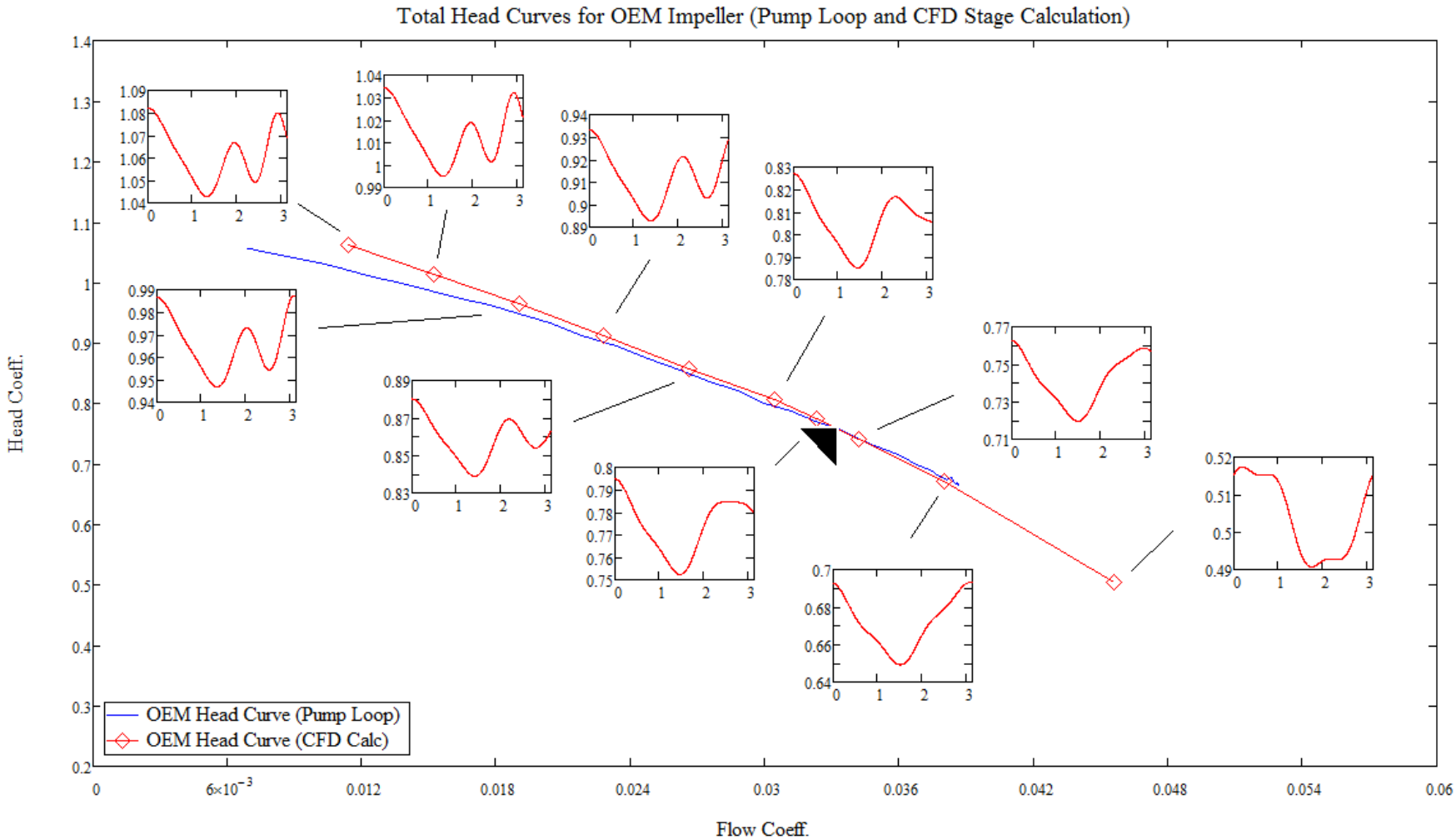

Figure 6.20: OEM Stage Head Curve

Figure 6.21 show the performance results (head and efficiency) for the CFD component and stage calculations as well as the experimental result for the OEM pump. As can be seen the stage calculation predicted the head performance with a higher degree of accuracy when compared to the component calculation. The efficiency was also predicted with a high degree of accuracy for the stage calculation when compared with the component calculations. At partload the stage calculation over predicted the efficiency performance.

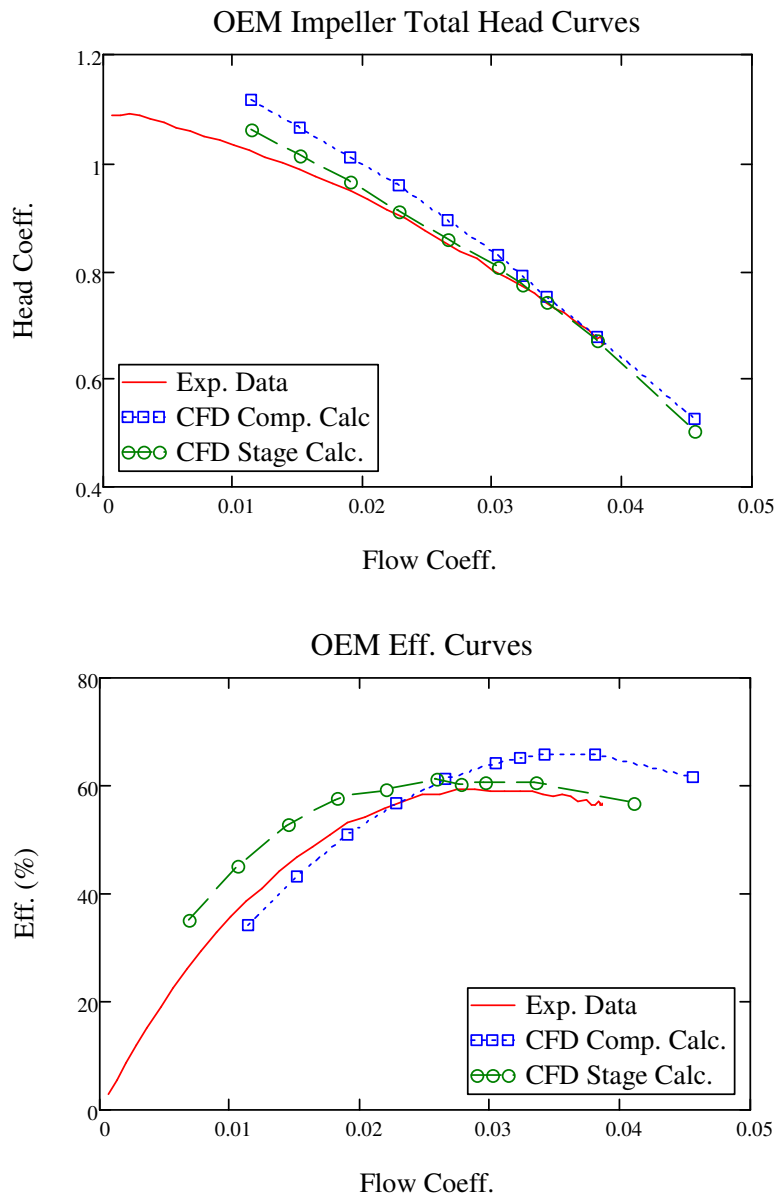

Figure 6.21 OEM Total Head (Left) and Efficiency (right) Curves for Experimental Data, Component and Stage Calculation

Chapter 7: Redesign of OEM Impeller

The goal of this chapter is to study a methodology for redesign of an existing product, the OEM impeller. This chapter presents a case study where the redesign process is tested on an existing industrial product, Allis Chalmers PWO Pump 6x3x14 (Paper, Pulp and Process Pump). The redesign model generates a series of optimal impeller designs which are then evaluated with the CFD process. The most efficient design is selected for prototyping and experimental validation.

7.1 Redesign Based on Geometrical Parameterization and Mathematical Model

Given a particular number of vanes, z, and inlet position, θ_x, the mean inlet and outlet blade angles can be optimized to produce an impeller geometry which exhibits minimum losses and optimal efficiency. This section describes the process by which the optimal mean blade angles are calculated. Appendix B contains a MathCAD script file which is used for calculation of mean blade angles.

7.1.1 Step I: Input Data

Figure 2.4 in Chapter 2 depicts the geometry of the parameterized centrifugal impeller. Input data is required for the design process. There are two sets of input data: design point and geometry. The existing process conditions can be entered as the design duty or the OEM design duty can be used. The geometric parameter, are fixed parameter associated with hub and shroud profiles.

Fixed Geometric Parameter		**Design Duty**	
Impeller Outlet Diameter	D_2	Machine Design Flow	Q
Hub Diameter	D_h	Machine Design Speed	n
Outlet Blade Width	b_2	Volumetric Efficiency	η_v
Impeller Eye Diameter	D_0		
Peripheral Radius Of Curvature	R_T		

Table 7.1: Fix Geometrical Parameters for Redesign Model

7.1.2 Step II: Hydraulic Parameters

Hydraulic parameters describe the flow magnitudes and are function of fixed geometrical parameters as well as z and β_{2B}. The flow coefficient can be calculated form:

$$\phi_2 = \frac{c'_{2m}}{u_2} = \frac{Q}{\eta_v A_2 u_2} \tag{7.1}$$

The head coefficient can then be calculated from:

$$\psi_2(\beta_{2B}) = \frac{c_{2u}}{u_2} = h_0 - \xi_2 \phi_2 \cot(\beta_{2B}) \tag{7.2}$$

As was described in Chapter 3.2.2, slip is a function of outlet angle and number of vanes.

$$h_0 = f(\beta_{2B}, z) \tag{7.3}$$

Blockage is also function of geometric parameters:

$$\xi_2 = f(D_2, t_2, \beta_{2B}, z) \tag{7.4}$$

To reduce the number of geometric parameters required to work with, the following condition will be imposed on the vane thickness. However, it should be noted that in order to minimize losses inside the impeller the blade thickness should be optimized to a minimum without compromising the structural integrity of the blade. Therefore the vane thickness is strictly governed by the pressures acting on the blade and the strength of material used for the blade.

$$t_x = 0.006 D_2 \tag{7.5}$$

$$t_2 = t_2 = 0.018 D_2 \tag{7.6}$$

7.1.3 Step III: Flow Direction at Mean Streamline Inlet

In order to obtain shockless entry at the impeller inlet the flow angle should be equal to the true blade angle. However, in order to obtain good performance over a wide range of flow rates (left and right side of BEP) a small positive incidence of flow against blade angle is desirable. Therefore the blade angle at the inlet can be calculated from:

$$\tan(\beta_{xB}) = 1.06 \cdot \tan(\beta_x) \tag{7.7}$$

The flow angle at inlet is function of number of blades and θ_x. Using the geometrical parameter x and y which were formulated in Chapter 2.3, the mean inlet flow angle can be calculated from Equation (7.8) [**1**].

$$\sin(\beta_x(\emptyset_x, z)) = \frac{c'_{xm}}{u_x} = \frac{Q/A_x}{u_x} = \frac{ax^2y + \phi_2(x^2y^2 + \phi_2^2 - a^2x^2)^{0.5}}{x^2y^2 + \phi_2^2} \quad \textbf{(7.8)}$$

Where x=f(θ_x) and y=f(θ_x) and

$$a = t_x z / D_2 \quad \textbf{(7.9)}$$

7.1.4 Step IV: The Average Flow Angle

Figure 7.1 shows the average relative velocity of the fluid, w_{avg}. The average meridional component of absolute velocity can be calculated as the mean of the meridional component of absolute velocity at the inlet and outlet.

$$c_{m,avg} = \frac{c_{2m} + c_{1m}}{2} \quad \textbf{(7.10)}$$

The average peripheral component of relative velocity is calculated from the mean of peripheral component of relative velocity at inlet and outlet.

$$w_{u,avg} = \frac{(u_2 - c_{u2}) + u_1}{2} \quad \textbf{(7.11)}$$

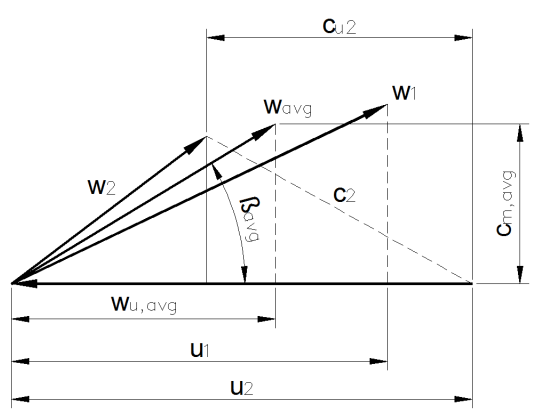

Figure 7.1: Flow Averaging (Vector Method)

Therefore the average flow angle can be calculated from the average peripheral component of relative velocity and average meridional component of absolute velocity [**1**].

$$\tan\left(\beta_{avg}(\theta_x, z, \beta_{2B})\right) = \frac{c_{2m} + c_{1m}}{(u_2 - c_{u2}) + u_1} = \frac{\phi_2(\xi_2 + \xi_1/(A_x/A_2))}{1 - h_0 + \phi_2\xi_2 \cot(\beta_{2B}) + D_x/D_2} \quad \textbf{(7.12)}$$

$$\tan\left(\beta_{avg}(\theta_x, z, \beta_{2B})\right) = \frac{\phi_2(\xi_2 + \xi_1/x)}{1 - h_0 + \phi_2\xi_2 \cot(\beta_{2B}) + y} \quad \textbf{(7.13)}$$

7.1.5 Step V: Airfoil Parameters

The chord angle is simply the mean of entry and exit true blade angles.

$$\beta_{CH}(\theta_x, z, \beta_{2B}) = \frac{\beta_{2B} + \beta_{xB}}{2} \quad \textbf{(7.14)}$$

The angle of attack for blade with NACA 65 camber line can be expressed as [**1**]:

$$\alpha(\theta_x, z, \beta_{2B}) = \Delta\alpha + (C_{LA0} - C_{Li})/0.098 \quad \textbf{(7.15)}$$

The flow incidence to the chord angle:

$$i(\theta_x, z, \beta_{2B}) = \beta_{CH} - \beta_{avg} \quad \textbf{(7.16)}$$

7.1.6 Step VI: Solving for Outlet Angle

Since incidence is a function of θ_x, z and β_{2B}, you can solve for exit angle by equating the incidence with vane angle of attack.

$$i(\theta_x, z, \beta_{2B}) - \alpha(\theta_x, z, \beta_{2B}) = Res \quad \textbf{(7.17)}$$

Where Res=±1e-6

In order have stall free operation at part load or at off design operating conditions, the range of lift coefficient will be limited by enforcing a limiting function.

$$C_{LA0} < 0.600 \quad \textbf{(7.18)}$$

As discussed in Chapter 3.2.3 rapidly decelerating flow is associated with substantial losses. One method for calculating the rate of diffusion is by calculating the average diffusion angle similar to that of a square diverging channel.

$$\frac{\alpha_D}{2} = \text{atan}\left[\frac{(A_2/\pi)^{0.5} - (A_1/\pi)^{0.5}}{h_{1-2}}\right] \quad \textbf{(7.19)}$$

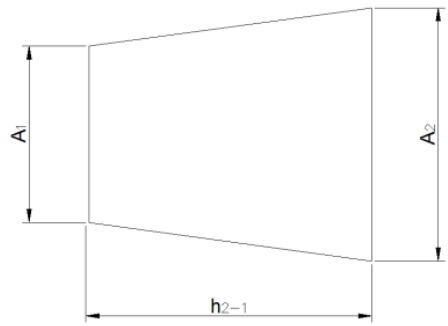

Figure 7.2: Diverging Channel

$$\frac{\alpha_D}{2} = \text{atan}\left[\frac{(1 - x^{0.5}) - \left(\frac{b_2}{D_2}\right)^{0.5}}{\frac{l}{D_2}}\right] < 6.0° \tag{7.20}$$

It is shown that local rapid deceleration and acceleration of relative velocity are associated with heavily chambered vanes. Therefore in order to reduce profile drag, flow acceleration and deceleration, the blade chamber is limited by enforcing a limiting function [**1**].

$$|\beta_{2B} - \beta_{xB}| < 8.0° \tag{7.21}$$

7.1.7 Mathematical Model Results

For detailed MathCAD calculation script file, refer to Appendix B . Table 7.2 tabulates the input parameters and machine design conditions.

Fixed Geometric Parameter		**Design Duty**	
D_2	14 [in]	Q	400 [gpm]
D_h	1.137 [in]	N	1150 [rpm]
b_2	1.19 [in]	η_v	95 [%]
D_0	4.942 [in]		
R_T	2.515 [in]		
t_x	0.25 [in]		

Table 7.2: OEM Pump Geometrical Parameter and Design Duty

Figure 7.3 shows the normalized geometry of mean streamline for θ_x=7.8° and 15°.

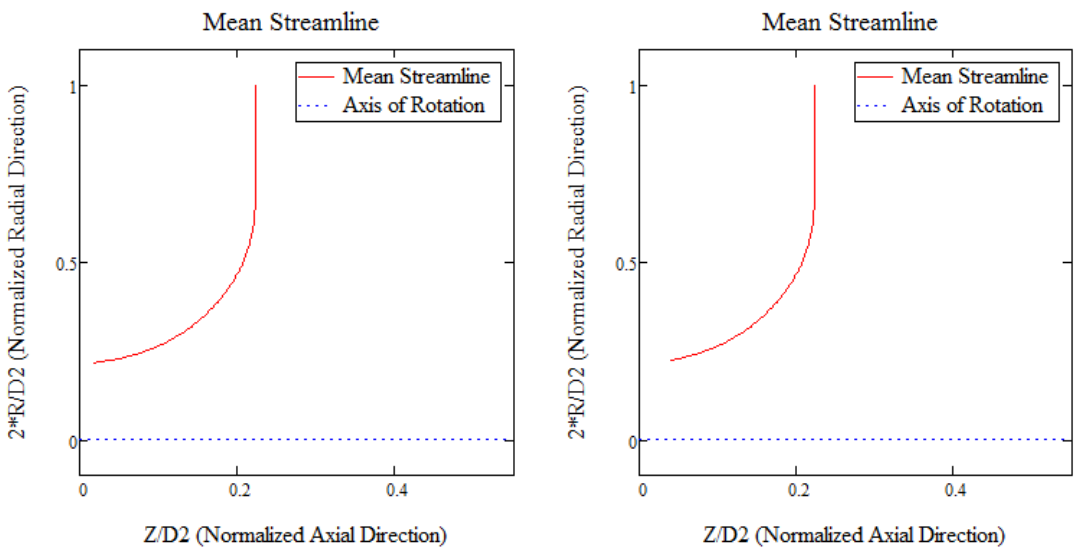

Figure 7.3: Mean Streamline for OEM Impeller θ_x=7.8° (Left) and θ_x=15° (Right)

Table 7.3, shows the calculated result for inlet and outlet blade angles corresponding to θ_x=7.8°. For z=2 and 3 the blade chamber is limited is not satisfied.

z	$\beta_{2B}(z)$	$\beta_{xB}(\theta_x,z)$	$\alpha_d(\theta_x,z, \beta_{2B}(z))/2$	$CL_A(\theta_x,z, \beta_{2B}(z))$	$\lvert \beta_{2B}(z)- \beta_{xB}(\theta_x,z)\rvert$	Res
2	10.2°	20.2°	1.671°	-0.111	9.987°	1E-6
3	12.7°	21.3°	1.866°	9.719E-3	8.612°	1E-8
4	16.0°	22.4°	2.098°	0.147	6.494°	1E-8
5	21.0°	23.6°	2.417°	0.325	2.623°	1E-8
6	29.9°	24.7°	2.921°	0.592	5.133°	1E-6

Table 7.3: Redesign Model Results for θ_x=7.8°

Table 7.4 show the blade length in θ-R plane ($l_{R,\theta}/D_2$), wrap angle in θ-R plane ($\varphi_{R,\theta}$), θ-R blade plot and mean streamline blade to blade plot corresponding to θ_x=7.8°.

z	$l_{R,\theta}/D_2$	$\varphi_{R,\theta}$ [°]	Radial Blade Plot (θ_x=7.8°)	Mean Blade-to-Blade Plot
2	1.466	273.9	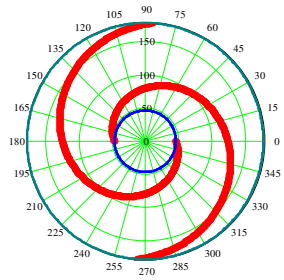	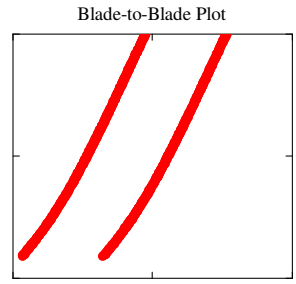
3	1.293	243.3	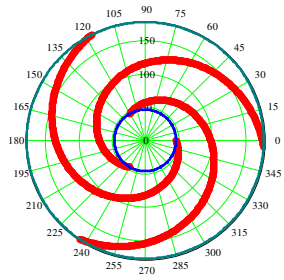	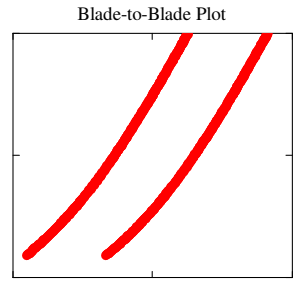
4	1.135	215.0	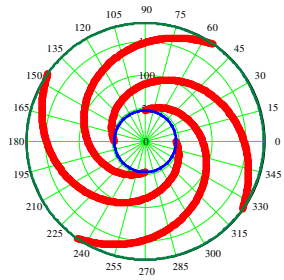	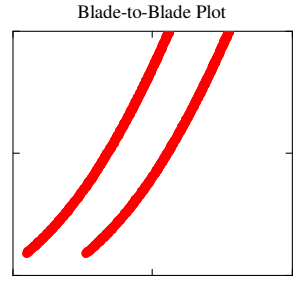
5	0.977	185.8	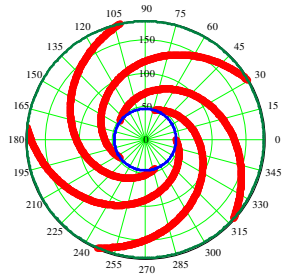	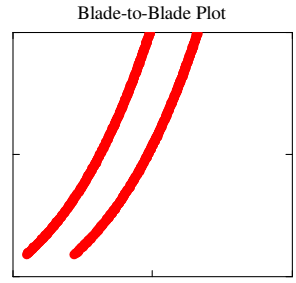
6	0.801	153.5	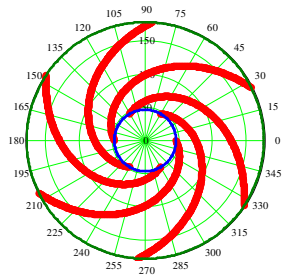	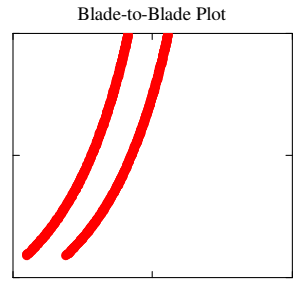

Table 7.4: Redesign Model Calculated Blade Characteristics θ_x=7.8°

Table 7.5 tabulates all possible optimal geometric parameters which are bounded by limitation of section 0 for θ_x=7.8°, 10°, 12° and 15°.

θ_x [°]	Impeller No.	z	β_{2B} [°]	β_{xB} [°]	$\alpha_D/2$ [°]	CL_A	$\lvert \beta_{2B} - \beta_{xB} \rvert$ [°]	$l_{R,\theta}/D_2$	$\varphi_{R,\theta}$ [°]
7.8	1	4	16.0	22.4	2.098	0.147	6.494	1.135	215.0
	2	5	21.0	23.6	2.417	0.325	2.623	0.977	185.8
	3	6	29.9	24.7	2.921	0.592	5.133	0.801	153.5
10.0	4	5	15.7	22.7	2.056	0.211	7.042	0.939	180.2
	5	6	19.3	23.9	2.297	0.351	4.596	0.826	165.2
12.0	6	5	14.6	18.9	2.026	0.276	4.330	0.667	131.5
	7	6	17.1	23.5	2.144	0.306	6.372	0.714	142.6
15.0	8	5	14.4	22.3	1.949	0.187	7.929	0.773	155.2

Table 7.5: Optimal Design Result of Redesign Model

Impeller 1, 4, 6 and 8 display minimum diffusion angles and it can be speculated that these impellers will have flow patterns with less rapid deceleration. However, there seems to be a tradeoff between minimization of decelerated flow and increase in blade camber which increases profile drag. Impeller 1, 2 and 4 also result in large wrap angles and hence large blade lengths. This means that friction losses are much greater for these impellers. Impeller 2, 5 and 6 display low camber angle and it can be speculated that these impellers display lower drag losses. Impeller No. 6 displays both low camber angle and low diffusion angle. As we will see in Chapter 7.2, impeller No. 6 is the most efficient impeller amongst the eight impellers which are generated by the Redesign model.

7.2 Numerical Assessment of Design

Using the CFD process which is described in Chapter 6.5, the series of impeller designs are evaluated for their performance. This is done by performing a stage calculation on each impeller design. Figure 7.4 shows the efficiency performance results for impeller number 1 to 8.

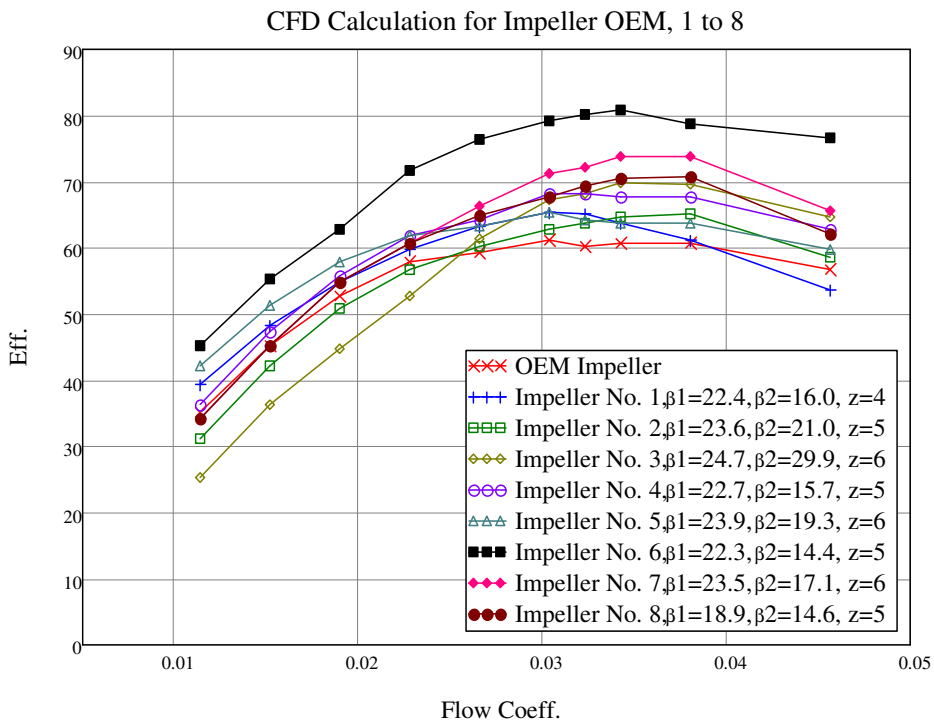

Figure 7.4: Efficiency Performance Results for Redesigned Impellers No. 1 to 8

As it was speculated in Chapter 0, impeller No. 6 displays higher efficiency amongst all impeller designs. This is due to its low diffusion and camber angle which reduces flow separation and reduces drag losses.

7.3 Redesigned Impeller

This section highlights the steps and procedures which are required to prepare the digitized 3D impeller model for prototyping and testing.

7.3.1 Impeller Prototyping

Figure 7.5 show a 3D model of the redesigned impeller. The impeller consists of a rapid prototyped thermoplastic and a machined stainless steel threaded insert. The metal insert is used to connect the impeller to the pump shaft and to prevent wearing of thermoplastic material on the pump shaft. The impeller is fixed to the threaded insert with four machine screws. Working drawing of the impeller insert can be found in Appendix C .

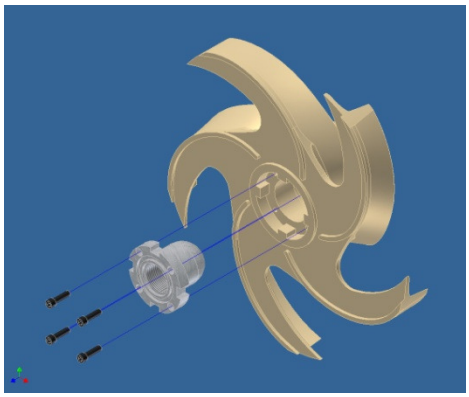

Figure 7.5: Prototype Impeller 3D Assembly Model

A number of features were added to the impeller to optimize its performance and maintain structural integrity during performance testing. To reduce pressure around the stuffing box pump-out vanes (POV) were added to the back of the impeller. These vanes reduce or prevent fluid leakage through the packing seal by maintaining a low pressure at the stuffing box. They also help maintain axial force balance on the impeller to prevent axial deflection at higher operating pressures (at partload or left of BEP). However, because the POV increase surface area of the impeller they cause increases in drag and disk friction losses which in turn affect the performance negatively. Higher energy pumps such as API pumps do not use POV for this reason. Nevertheless the thrust balance comes with a cost, as there is additional power required for the POV. Because the impeller is constructed from thermoplastic which has lower elastic modulus then conventional metals, addition of pump-out vanes will prevent large axial deflections which could cause the impeller to come in contact with the wear plate.

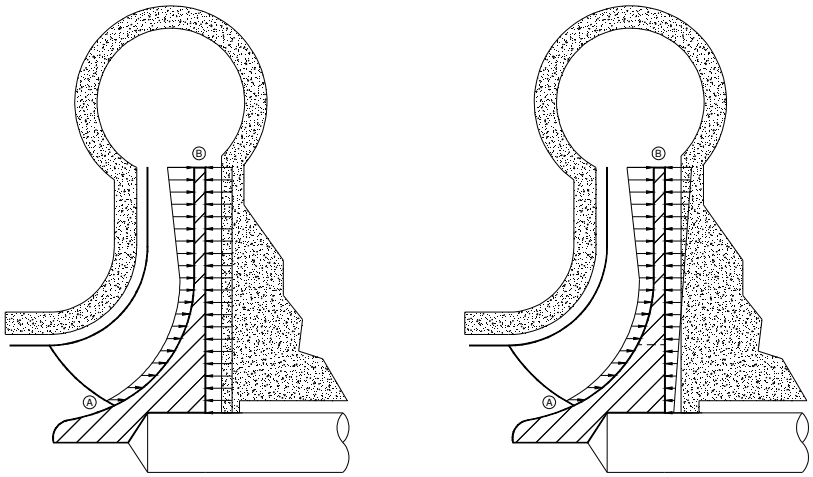

Figure 7.6: Impeller Pressure Distribution, Without POV (Left) and With POV (Right)

The impeller is designed to be a fully open impeller with hub cut sections which acts as balance hole to maintain axial load balance. Also the hub cut sections reduces surface area which helps maintain low disk friction. Figure 7.6 shows a cross section of the impeller and the thrust loading for a fully open and a semi-open impeller (impeller with no cut section through the hub). The pressure distribution can be seen on the front of the impeller hub from point A to B (where the pressure increases gradually). For semi-open impeller the pressure distribution on the back of the impeller is constant since there is no fluid flow to the back of the impeller. The net axial load on the impeller tents to push the impeller towards the wear plate and creates a trust force on the pump shaft. In a fully open impeller or a semi-open impeller with balance hole, the fluid pressure is equalized from front to back causing the impeller to be balanced. Of course the more material is removed the more axially balanced and less disk friction. However there is a tradeoff between maintain structural integrity of the vanes and maintaining low disk friction. For this reason some material is left on the hub to maintain structural strength.

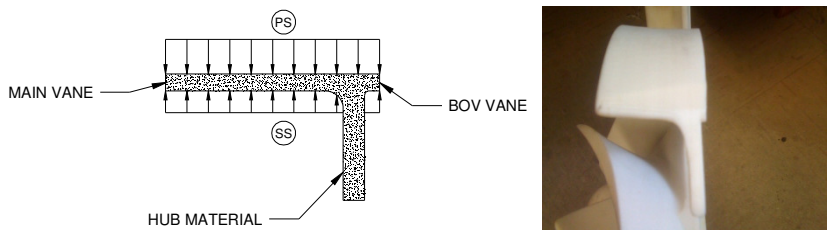

Figure 7.7: Impeller Blade Loading Profile (Left) and Impeller Cross Sectional Shape (Right)

Figure 7.7 shows a cross section of blade and the loading profile. The net average pressure distribution on the PS of the blade is larger than the SS. To strengthen the blade and reduce substantial deflection, a strip of hub material is left to increase the moment of inertia of the blade.

7.3.1.1 Material selection

Selection of impeller material is very important since tight clearances between the impeller and the wear plate may cause interference at high blade loading during pump's operation. For this reason a number of different thermoplastics were reviewed based on their strength, elongation and prototyping capabilities (slice thickness and tolerances).

	Materials									
	ABS	**ABSi**	**ABS-M30**	**ABS-M30i**	**ABS-EDS7**	**PC**	**PC-ISO**	**PC/ABS**	**ULTEM**	**PPSF**
Tensile Strength	3200 psi (22 MPa)	5400 psi (37 MPa)	5300 psi (36 MPa)	5300 psi (36 MPa)	5300 psi (36 MPa)	9800 psi (68 MPa)	8265 psi (57 MPa)	5900 psi (41 MPa)	10390 psi (72 MPa)	8000 psi (55 MPa)
Tensile Elongation	6.0%	4.4%	4.0%	4.0%	3.0%	4.8%	4.3%	6.0%	5.9%	3.0%
Flexural Stress	6000 psi (41 MPa)	8980 psi (62 Mpa)	5200 psi (36 MPa)	5200 psi (36 MPa)	8800 psi (61 MPa)	15100 psi (1041 MPa)	13089 psi (90 MPa)	9800 psi (68 MPa)	16700 psi (115.1 MPa)	15900 psi (110 MPa)
IZOD Impact Notched	2ft-lb/in (106.8 J/a)	1.8 ft-lb/in (96 J/a)	2.6 ft-lb/in (139 J/a)	2.6 ft-lb/in (139 J/a)	2.1 ft-lb/in (111 J/a)	1.0 ft-lb/in (53 J/a)	1.6 ft-lb/in (86 J/a)	3.7 ft-lb/in (196 J/a)	2.0 ft-lb/in (106 J/a)	1.1 ft-lb/in (58.7 J/a)
Machine Tolerances	+/- .005 in	+/- .0015 in	+/- .0015 in	+/- .0015 in	+/- .0015 in	+/- .0015 in	+/- .0015 in	+/- .0015 in	+/- .005 in	+/- .005 in
Slice Thickness	0.010 in	0.005 in	0.005in	0.005 in	0.007 in	0.007 in	0.007 in	0.007 in	0.010 in	0.010 in

Table 7.6: Prototyping Material Properties [37]

Table 7.6 shows different thermoplastic which are available for Fusion Deposit Modeling (FEM) [**37**]. Amongst these thermoplastics, Polycarbonate (PC) was selected for its high strength, low tensile elongation and high impact resistance [**38**]. Figure 7.8 shows some picture of the prototyped impeller which was built using a FDM machine with 0.007" slice layer.

Figure 7.8: Prototyped Impeller (Impeller No. 6)

7.3.2 Installation

Figure 7.9 shows the picture the original OEM impeller and the prototyped redesigned impeller side by side. The large wrap angle of original impeller can be seen in contrast with the redesigned impeller. This is one of the factors which contribute to low efficiency of this impeller. The blade thickness can also be seen from the Figure. The OEM impeller utilizes constant thick blades. The redesigned impeller is equipped with thin NACA 65 blade which is optimized for strength and has a lower drag characteristic.

Figure 7.9: OEM and Redesigned Impeller (Left), Installation of Resdigned Impeller (Right)

7.3.3 Redesigned Impeller Experimental Performance

Total head and efficiency curves for the redesigned impeller are shown in section 5.5.2. Figure 7.10 shows head curves for both OEM and redesigned impeller. Overall the redesigned impeller produces higher head for same volumetric flow.

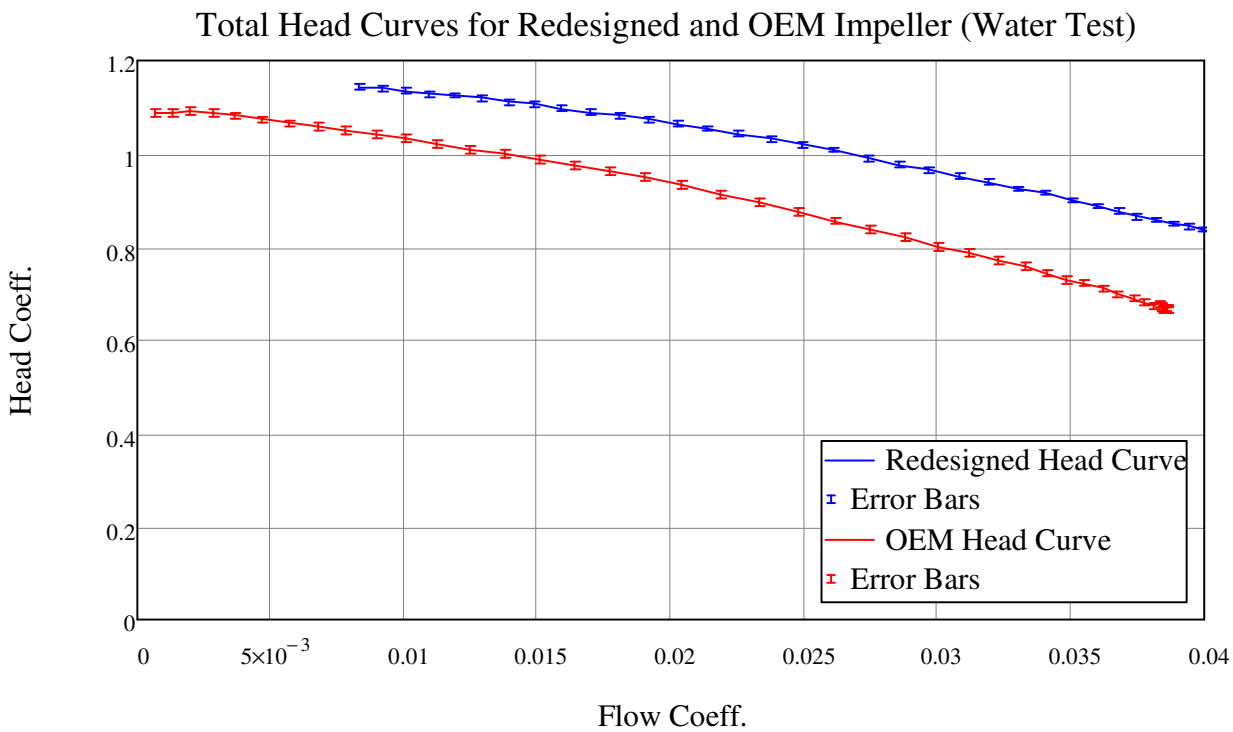

Figure 7.10: Head Curves for OEM (Red) and Redesigned Impeller (Blue)

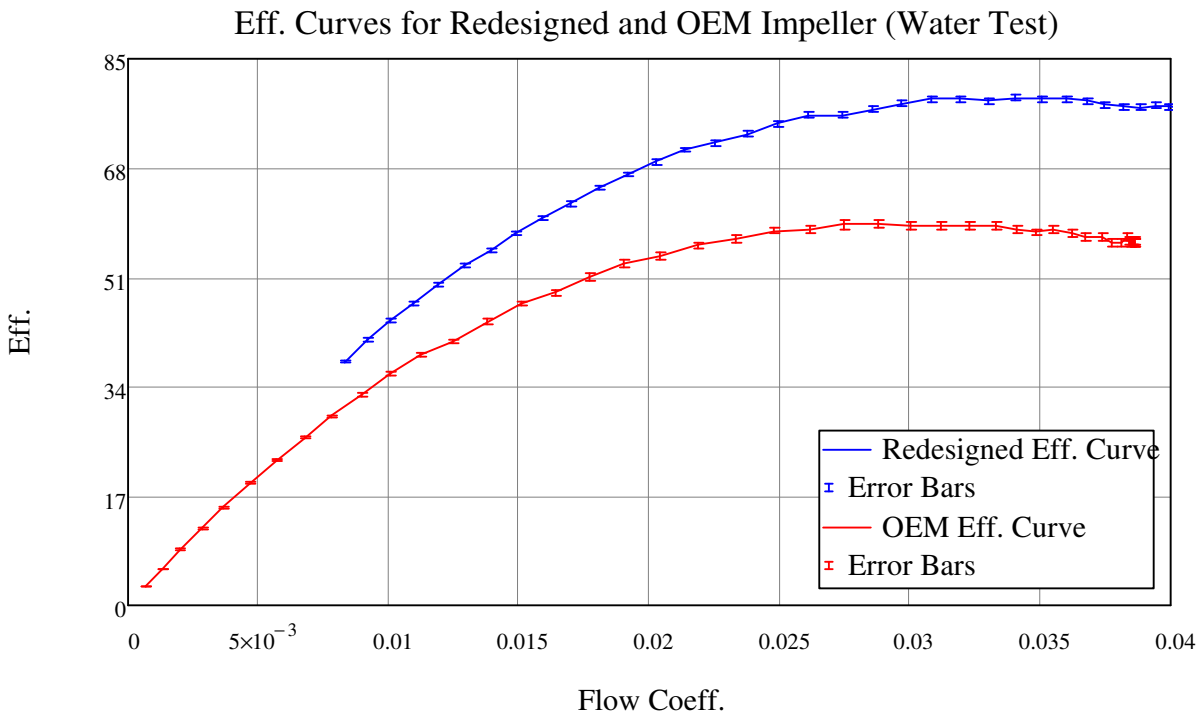

Figure 7.11: Efficiency Curves for OEM (Red) and Redesigned Impeller (Blue)

Figure 7.11 shows the efficiency curve for both OEM and redesigned impeller. Maximum efficiency obtained from the OEM impeller is 59.2%. The Redesigned impeller exhibits superior performance with BEP at 78.9%.

Chapter 8: Pulp Pump Efficiency Monitoring

This chapter examines the validity of the thermodynamic method in low consistency pulp service. The thermodynamic method is validated with the flow-meter base method for pulp consistencies of 0.5%, 1.0% and 1.5%.

8.1 Thermodynamic Method

The thermodynamic method can be explained by means of the one-dimensional steady flow energy equation. When a fluid is compressed in an isentropic process (ideal pump), its temperature rises to certain degree. However, in the real process the machine outlet temperature is slightly higher than the isentropic temperature rise (ΔT_i). This is due to increase in entropy. This difference in temperature between the ideal and the real case can only be contributed by inefficiencies of the pump.

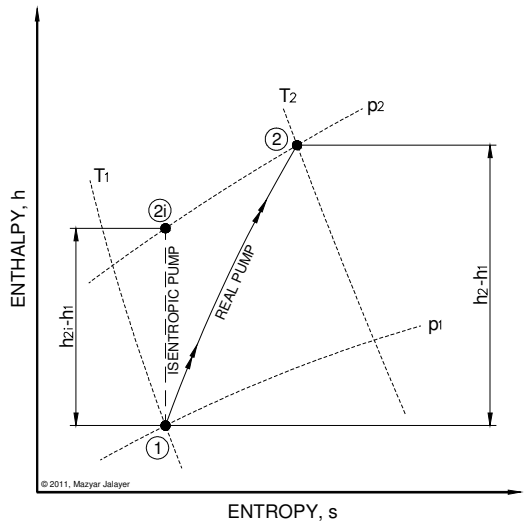

Figure 8.1: Enthalpy/Entropy Curves for Real and Ideal Pump

Figure 8.1 shows the Enthalpy (h)/Entropy(s) diagram for compressing a fluid from state 1 to state 2. In an ideal pump where all energy is converted into useful energy, fluid moves along the path 1 to 2i (isentropic, constant entropy). However, the losses inside the pump increase the entropy to stage 2 along the p_2 curve where the temperature rise is slightly higher than the stage 2i.

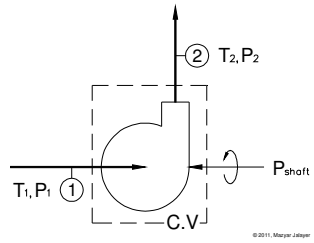

Figure 8.2: Pump Control Volume (Thermodynamic Method)

Figure 8.2 shows the control volume for the pump. Pump's efficiency can be obtained from total energy balance for real pump and ideal pump. Since the energy required to compress the fluid from p_1 to p_2 is lower for isentropic compression, the efficiency can be expressed by [**26**]:

$$\eta_{thermo} = \frac{h_{2i} - h_1 + \left[0.5\left({V_2}^2 - {V_1}^2\right) + g(EL_2 - EL_1)\right]}{h_2 - h_1 + \left[0.5\left({V_2}^2 - {V_1}^2\right) + g(EL_2 - EL_1)\right]} \quad \textbf{(8.1)}$$

This equation can also be represented by equating the inlet and outlet velocities to flow rate and suction/discharge inside pipe diameters.

$$\eta_{thermo} = \frac{h_{2i} - h_1 + \left[\frac{8 \cdot Q^2}{\pi^2}\left(\frac{1}{ID_2^4} - \frac{1}{ID_1^4}\right) + g(EL_2 - EL_1)\right]}{h_2 - h_1 + \left[\frac{8 \cdot Q^2}{\pi^2}\left(\frac{1}{ID_2^4} - \frac{1}{ID_1^4}\right) + g(EL_2 - EL_1)\right]} \quad \textbf{(8.2)}$$

If pump shaft power is known the volumetric flow rate (Q) can be directly calculated by equating the efficiency which is calculated via thermodynamic method with the conventional flow meter method.

$$\frac{\Delta H_{tot} \cdot Q \cdot \rho \cdot g}{\eta_{motor} \cdot P_{motor}} = \frac{h_{2i} - h_1 + \left[\frac{8 \cdot Q^2}{\pi^2}\left(\frac{1}{ID_2^4} - \frac{1}{ID_1^4}\right) + g(EL_2 - EL_1)\right]}{h_2 - h_1 + \left[\frac{8 \cdot Q^2}{\pi^2}\left(\frac{1}{ID_2^4} - \frac{1}{ID_1^4}\right) + g(EL_2 - EL_1)\right]} \quad \textbf{(8.3)}$$

Since the total differential head is a function of Q, the equation can be solved for the flow rate numerically. The inlet and outlet enthalpy can be easily be found from Peng Roberson state equations or from steam/water tables since enthalpy is function of both pressure and temperature. However the isentropic enthalpy, h_{2i}, cannot be determined easily since the isentropic temperature rise is not known. To find the isentropic enthalpy at state 2i, the

entropy at inlet (s_1) must be determined from inlet pressure and temperature and then the enthalpy at i2 can be found from s_1 and p_2.

8.2 Addition of Pulp Suspension

Assuming that pulp fibre does not increase in temperature under external pressure, efficiency can be represented for working fluid with consistency of x, where C_{pf} is heat capacity of cellulose wood fibre.

$$\eta_{thermo} = \frac{(1-x)(h_{2i}-h_1) + \left[\frac{8\cdot Q^2}{\pi^2}\left(\frac{1}{ID_2^4}-\frac{1}{ID_1^4}\right) + g(EL_2-EL_1)\right]}{(1-x)(h_2-h_1) + x\cdot C_{pf}(T_2-T_1) + \left[\frac{8\cdot Q^2}{\pi^2}\left(\frac{1}{ID_2^4}-\frac{1}{ID_1^4}\right) + g(EL_2-EL_1)\right]} \quad \textbf{(8.4)}$$

Since pulp consistency is equal to 0.015 maximum, it can be seen from the above equation that the error associated with calculating the efficiency for water only versus the suspension is negligible and in most cases less than 0.1%.

8.3 Experimental Technique

Figure 8.3 shows the process flow diagram (PFD) for the pump loop. The loop consist of two 4,000 L storage tanks (TK-001 and TK-002), suction and discharge pressure/temperature sensors (PT/TT-001 and PT/TT-002), an Allis Chalmers PWO Pump 6”x3”x14” Paper and Pulp Process Pump (P-001), a magnetic flow meter (FE-001) and a discharge motor operated valve (MOV-002). The pump is coupled to a TECO Westinghouse OPTIM He Plus motor and is powered via a variable frequency drive (VFD). The motor power is measured via a power meter that measures real power (P_{motor}), reactive power, complex power, apparent power, and the current phase. All measurements and control are done in Labview software.

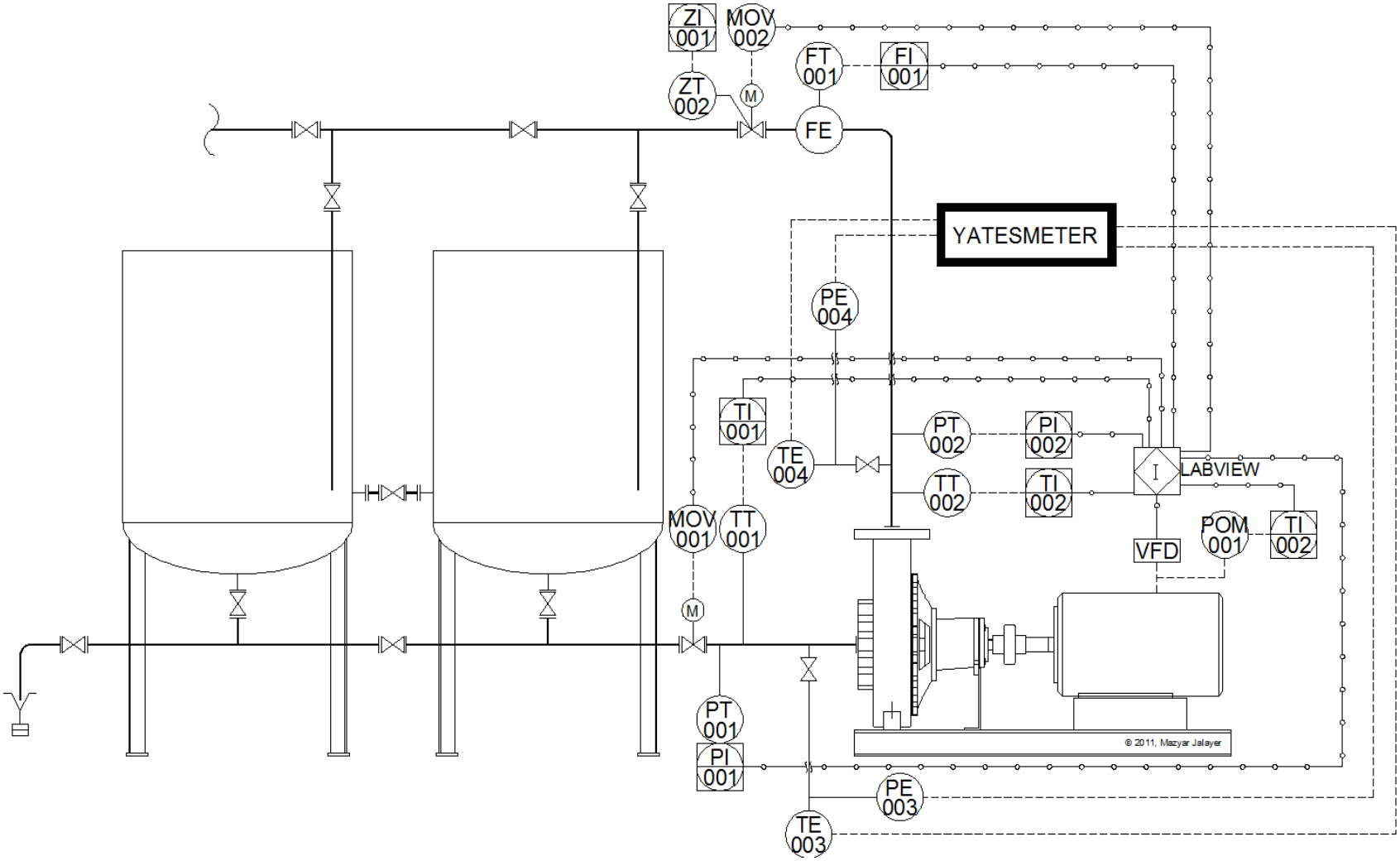

Figure 8.3: Experimental Setup (Thermodynamic Method)

An independent pressure/temperature measurement is collected with Yates Meter Pump Efficiency Monitor. This device measures and records suction and discharge pressure and temperatures. The device is able to measure the temperature to an accuracy of ±100µK. The power is manually recorded from the flow loop power meter to the Yates Meter device to calculate pump's total efficiency and flow rate. The flow rate, inlet and outlet temperature and pressure and motor power are recorded at multiple points along the pump curve by varying the flow via MOV-001. The machine speed is set at fix rotational speed of 1150±4 rpm (38.98 Hz). The tanks suction head is held at constant height (2.5m) for test trials with water and pulp suspension at 0.5%, 1.0% and 1.5% consistency. Northern Bleached Softwood Kraft (NBSK) pulp is utilized for trials with average fibre length of 2.486 mm. The consistency of prepared pulp stock is confirmed by taking four samples consistency test.

8.4 Results

The pump curves in Figure 8.4, 8.5, 8.6 captures the pump's performance for head and efficiency calculated from the conventional flow meter method and thermodynamic method (Yates Meter). The pumps performance is measure at BEP, off design and at partload.
The results from the thermodynamic method are consistent with that of the flow base method. Some discrepancy can be seen at partload. This may be due to the increase in amplitude of pulsating flow or the effect of recirculation that takes place at partload.
Since flow loop data sampling rate is not the same as Yates Meter device, the average discharge pressure measured from Yates Meter is slightly less than the flow loop data. There is some heat transferred from the pump to the ambient environment. This heat transfer is ignored in the thermodynamic calculation. Also at partload, there may not be sufficient mixing between the recirculating flow inside the impeller and the net flow through the impeller.

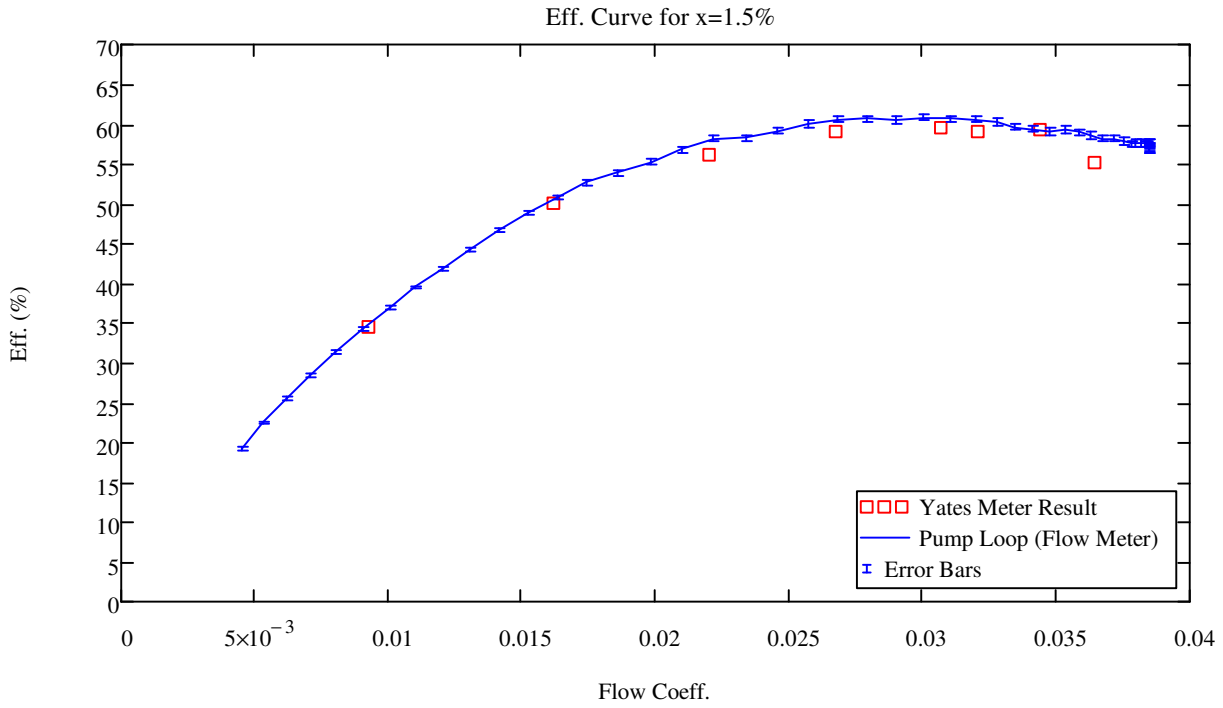

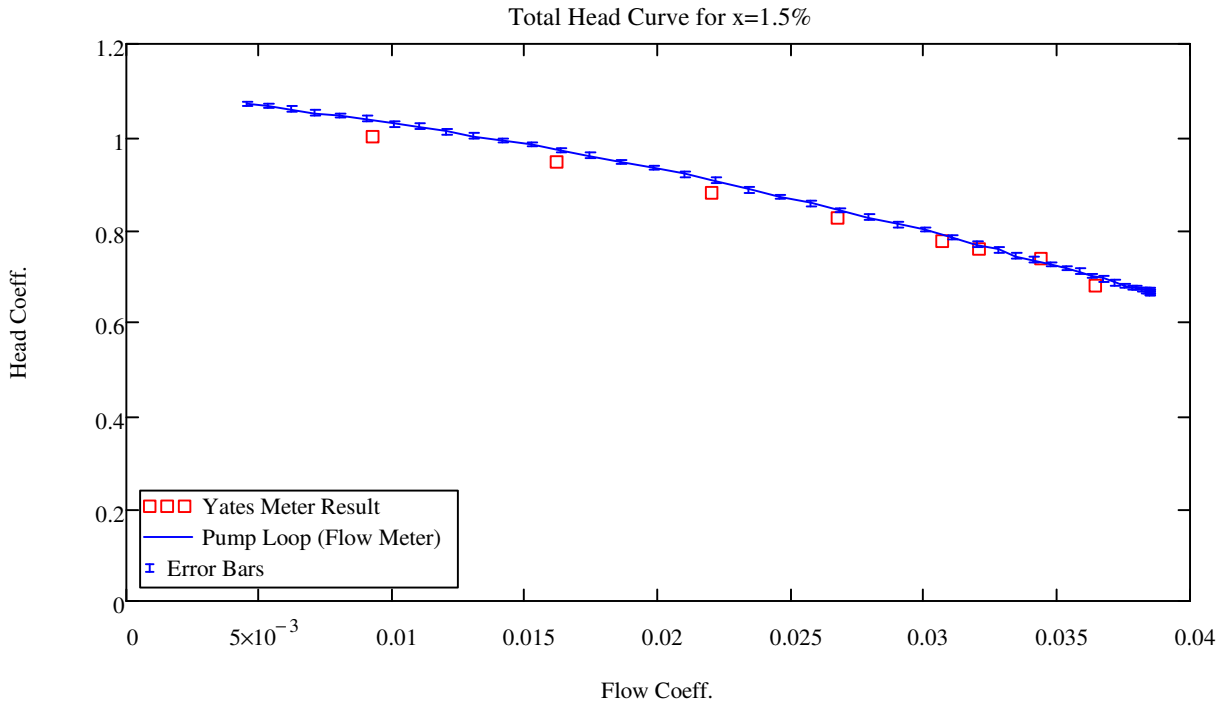

Figure 8.4: Head and Efficiency Curves for Pulp Consistency of 1.5%

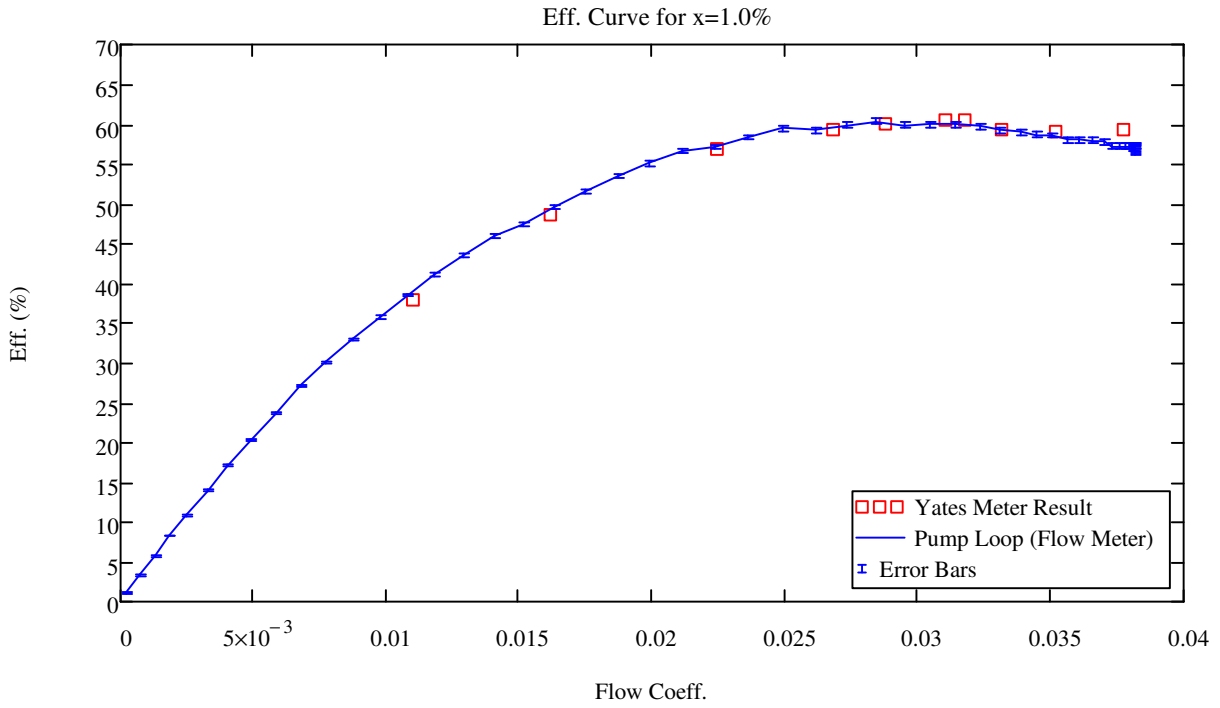

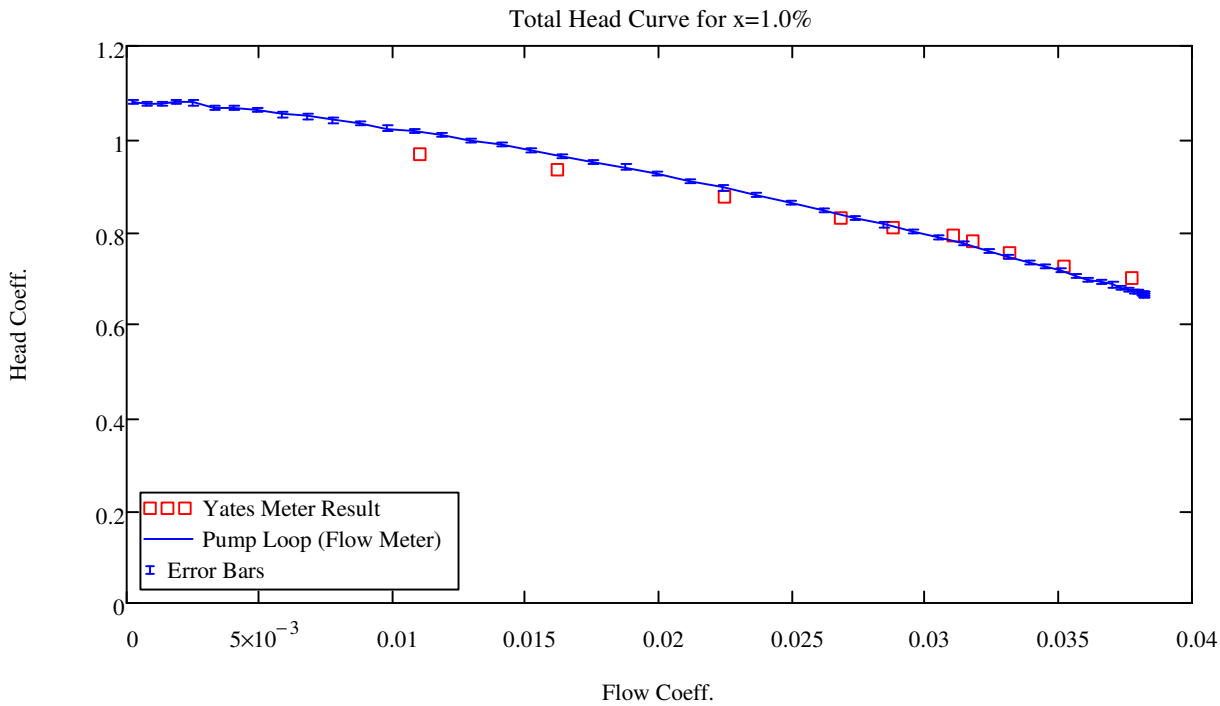

Figure 8.5: Head and Efficiency Curves for Pulp Consistency of 1.0%

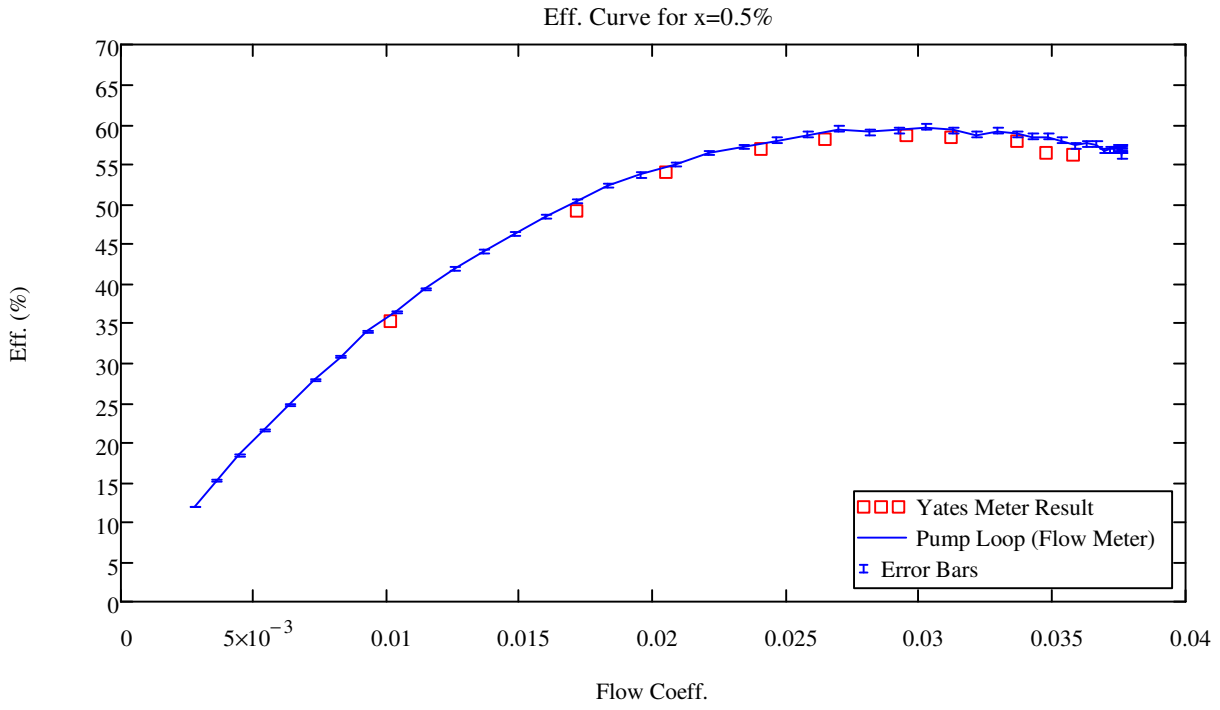

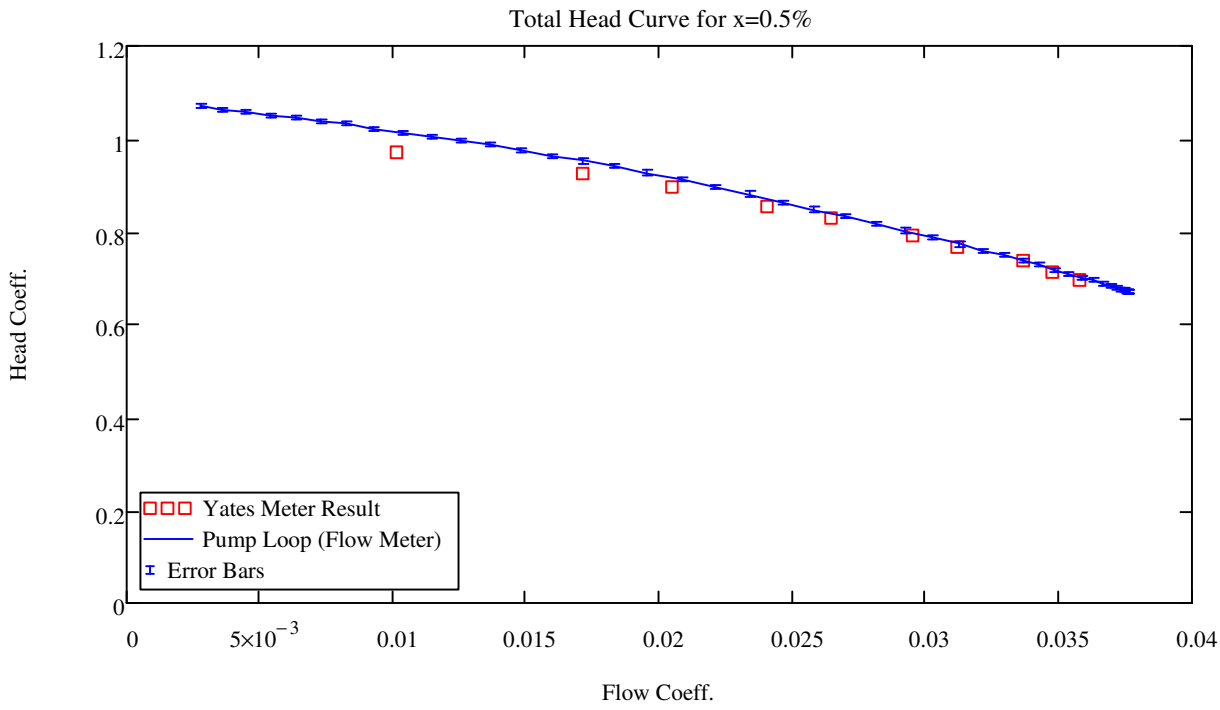

Figure 8.6: Head and Efficiency Curves for Pulp Consistency of 0.5%

Chapter 9: Conclusion

9.1 CFD Analysis of OEM impeller

Two types of CFD calculations were performed for the OEM impeller. The calculated head is consistent with the experimental data for both component and stage calculations. The component calculation over predicated the efficiency and performance of the pump. The stage calculation predicted both the head and efficiency with good accuracy at both design and off design conditions. Discrepancies between experimental result and the calculations were observed at partload. These discrepancies are due to the inherent complex flow behaviour at partload.

The CFD analysis reveals that flow inside the impeller is not guided well. Due to large wrap angle, the fluid inside the passage separates. This is partial due to large uneven pressure gradient on the SS and PS of the blade. The separation causes zones of stall fluid which decreases the available flow area. Large dynamic losses are observed as result of a 'jet' like flow in the vicinity of the recirculation zone. Large pressure and velocity gradients result in large blade loading which increase power consumption and reduce efficiency.

9.2 Redesign Model

A case study on Allis Chalmers PWO 6"x3"x14" pump showed that an efficiency increase of 19.7% can be achieved with the redesign methodology. Initial hypothesis revealed that impeller number 6 would outperform all other impeller designs which were generated by the redesign model. The validated CFD process revealed that this hypothesis is true because impeller number 6 has both low camber and diffusion angles.

9.3 Performance Monitoring (Thermodynamic Method)

It is found that the thermodynamic method can be utilized in low consistency pulp suspension service with consistency of up to 1.5%. Pump curves can be generated with as low as 30ft of head. It is found that the thermodynamic method is most accurate while the pump is operating at the BEP. Some discrepancy is realized at part-load (left of the curve). This may be due to inadequate heat transfer between recirculating fluid inside the pump and net flow through the pump at partload.

References

[1] B Neumann, *The Interaction Between Geometry and Performance of a Centrifugal Pump*. London: Mechanical Engineering Publications Limited, 1991.

[2] USDOE, "Pulp and Paper Mills: Profiting from Efficient Motor System Use," Washington, DC, 10099-547, 1999.

[3] Ducker Worldwide, "Market Research Report, Energy Efficiency within the Pulp and Paper, Water andWastewater and Irrigation Markets in the Pacific Northwest," Portland, Oregon, 00-067, 2000.

[4] R A Van den Braembussche, "Optimization of Radial Impeller Geometry," Rhode-Saint-Genèse, Belgium, RTO-EN-AVT-143, 2006.

[5] Sven Baumgarten and Thomas Muller, "Computer Aided Impeller Optimisation," *World Pumps*, pp. 28 - 31, March 2000.

[6] M Nataraj and V P Arunachalam, "Optimizing Impeller Geometry for Performance Enhancement of a Centrifugal Pump using the Taguchi Quality Concept," *Proc. IMech*, pp. 765 - 549, 2006.

[7] Berge Djebedjian, "Theoratical Model to Predict the Performance of Centrifugal Pump Equipped with Splitter Blade," *Mansoura Engineering Journal*, vol. 34, no. 2, pp. 50 - 70, June 2009.

[8] Johann Friedrich Gülich, *Centrifugal Pumps*. Berlin: Springer, 2008.

[9] ANSYS, *ANSYS BladeGen User's Guide*.: ANSYS, 2010.

[10] Paresh Girdhar and Octo Moniz, *Practical Centrifugal Pumps (Design, Operation and Maintenance)*. Burlington, MA: IDC Technologies, 2005.

[11] Nzumbe-Mesape Ntoko and Kamdem Djidjou, "A Basis for Teaching Centrifugal Pump Characteristics in an Undergraduate Course in Turbomachinery," *International Journal of Mechanical Engineering Education*, pp. 283 - 293.

[12] Cui Boaling, Zhu Zuchao, Zhang Jianci, and Chen Ying, "The Flow Simulation and Experimental Study of Low-Specific-Speed High-Speed Complex Centrifugal Impellers," *Chines J. Chem. Eng.*, pp. 435 - 441, 2006.

[13] J Bouillard, B Alban, P Jacques, and C Xuereb, "Liquid Flow Velocity Measurments in Stirred Tanks by Ultra-Sound Doppler Velocimetry," *Chemical Engineering Science* , pp. 747 - 754, 2001.

[14] Shuliang Cao and Guoyi Peng, "Hydrodynamic Design of Rotodynamic Pump Impeller for Multiphase Pumping by Combined Approach of Inverse Design and CFD Analysis," *ASME Journal of Fluid Engineering*, pp. 330 - 337, 2005.

[15] K W Cheah and T S Lee, "Numerical Flow Simulation in a Centrifugal Pump at Design and Off-Design Conditions," *International Journal of Rotating Machinery*, pp. 1 - 8, 2007.

[16] Jose Gonzalez and Joaquin Fernandez, "Numerical Simulation of the Dynamic Effects Due to Impeller-Volute Interaction in a Centrifugal Pump," *Journal of Fluids Engineering*, pp. 348 - 355, 2002.

[17] Akira Goto and Motohiko Nohmi, "Hydrodynamic Design System for Pumps Based on 3-D CAD, CFD, and Inverse Design," *Journal of Fluids Engineering*, pp. 329 - 473, 2002.

[18] M K Guleren and A Pinarbasi, "Numerical Simulation of Stalled Flow Within a Vaned Centrifugal Pump," *Proc. Instn Mech. Engrs*, vol. 218, pp. 425 - 435, 2004.

[19] M El Hajem, A Akhras, and J Y Champagne, "Rotor-Stator Interaction in a Centrifugal Pump Equipped with a vaned diffuser," *Proceedings of the Institution of Mechanical Engineers, Part A: Journal of Power and Energy*, vol. 215, pp. 809 - 817, 2001.

[20] Xian-hua Li, Shu-jia Zhang, Bao-lin Zhu, and Qing-bo Hu, "The Study of the k-ε Turbulence Model for Numerical Simulation of Centrifugal Pump," *Computer-Aided Industrial Design and Conceptual Design*, pp. 1 - 5, 2006.

[21] F Shi and H Tsukamoto, "Numerical Study of Pressure Fluctuations Caused by Impeller-Diffuser Interaction in a Diffuser Pump Stage," *Journal of FLuid Engineering*, vol. 123, pp. 466 - 474, 2001.

[22] G Poirson, Houille Blanche, and G Willm, "Efficiency measurements for hydraulic turbines by the Poirson thermometric method," 1954.

[23] P F Colon, "British Standards Institution BS 5860 1980 Method for measuring the

efficiency of hydraulic turbines, storage pumps and pump turbines (thermodynamic method)," Glasgow, 421 , 1969.

[24] Peta Maddy and Ross Routley, "Pump Efficiency Monitoring and Management at Melbourne Water," , Bendigo, 2005.

[25] Austin Whiller, "Pump Efficiency Determination in Chemical Plant from Temperature Measurements".

[26] M T Merry, "Evaluation of a thermodynamic method for efficiency measurements on a low pressure pump in water and mercury," 1983.

[27] Routley Ross and Ken Baxter, "Pump Efficiency Monitoring and Management at Melbourne Water," , Bendigo, 2005.

[28] André Bakker. http://www.bakker.org. [Online]. http://www.bakker.org/dartmouth06/engs150/11-bl.pdf

[29] Val S Lobanoff and Robert R Ross, *Centrifugal Pumps Design and Application 2nd Edition*. Houston, TX: Gulf Publishing Company, 1992.

[30] J F Gulich, "Effect of Reynolds Number and Surface Roughness on the Efficiency of Centrifugal Pumps," vol. 125, 2003.

[31] William Xia, "Polymer Coating of Pumps Boosts Efficiency, Performance," *Water World*, 2002.

[32] G F Wislecenus, *Fluid Mechanics of Turbomachinery*. New York: Dover Publivations, 1965.

[33] M Zangeneh, "Advanced Design Software for Pumps," *Wold Pumps*, pp. 28 - 31, June 2007.

[34] Nicholas Pedersen and Poul S Larsen, "Flow in a Centrifugal Pump Impeller at Design and Off-Design Conditions - Part I: Particle Image Velocimetry (PIV) and Laser Doppler Velocimetry (LDV) Measurments," *Jounal of Fluid Engineering*, vol. 125, pp. 61 - 72, 2003.

[35] A Fatsis, A Panoutsopoulou, and N Vlachakis, "Numerical Modelling of a Turbocharger Splitter-Vaned Centrifugal Impeller at off-Design Conditions, Part I: Impeller Flow Field," *Jordan Journal of Mechanical and Industrial Engineering*, vol. 4, no. 1995-

6665, pp. 553 - 566, 2010.

[36] Byskov k Rikke and Nicholas Pendersen, "Flow in a Centrifugal Pump Impeller at Design and Off-Design Conditions-Part II: Large Eddy Simulations," *Journal of Fluid Engineering*, vol. 125, pp. 73 - 83, 2003.

[37] Earl Logan and Ramendra Roy, *Handbook of Turbomachinery*. New York: Marcel Dekker Inc., 2003.

[38] Xinwei Song, Wood G Houston, Steven W Day, and Don B Olsen, "Studies of Turbulence Models in a Computational Fluid Dynamics Model of a Blood Pump," *Artificial Organs*, vol. 27, no. 10, pp. 935 - 937, Oct 2003.

[39] J N. N Counsil and Goni K Boulama, "Validating the URANS shear stress transport $\gamma - Re\theta$ model for low-Reynolds-number external aerodynamics," *International Journal for Numerical Methods in Fluids*, Jul 2011.

[40] ANSYS, "CFX-5 Best Practices Guide for Turbomachinery," 2001.

[41] Lamloumi Hedi and Kanfoudi Hatem, "Numerical Flow Simulation in a Centrifugal Pump," in *International Renewable Energy Congress*, Sousse, Tunisia, 2010, pp. 300 - 304.

[42] Ulrik Ullum, Jennifer Wright, Oruz Dayi, and Ali Ecder, "Prediction of Rotating Stall Within an Impeller of a Centrifugal Pump Based on Spectral Analysis of Pressure and Velocity Data," *Journal of Physics: Conference Series 52*, pp. 36 - 45, 2006.

[43] Ismail B Celik and Urmila Ghia, "Procedure for Estimation and Reporting of Uncertainty Due to Discretization in CFD Applications," *Journal of Fluids Engineering*, vol. 130, 2008.

[44] (2011) RedEye on Demand. [Online]. http://www.redeyeondemand.com/downloads/chart-horizontal.pdf

[45] (2010) RedEye on Demand. [Online]. http://www.redeyeondemand.com/downloads/MaterialPropertiesReport-PC.pdf

[46] Stan Shiels, "When Trimming a Centrifugal Pump Impeller can Save Energy and Increase Flow Rate," *World Pumps*, pp. 37 - 40, Nov 1999.

[47] Shujia Zhang, Baolin Zhu, Qingbo Hu, and Xianhua Li, "Virtual Performance

Experiment of a Centrifugal Pump," *Artificial Reality and Telexistence--Workshops, 2006. ICAT '06. 16th International Conference on*, pp. 205 - 208, 2006.

[48] Mike Pemberton, "Strategies for Optimizing Pump Efficiency and LCC Performance," *PaperAge*, pp. 28 - 32, June 2003.

[49] V. V. Malyushenko, S. M. Aspidov, and V. Yu. Andryushchenko, "Selection of Optimal Thickness of Centrifugal-Pump Impeller Vanes," *Chemical and Petroleum Engineering*, pp. 987 - 989, 1977.

[50] A E Risk, "Selecting Paper Stock Pumps,".

[51] Luthi Et Al, "Pulp Centrifugal Pump," 4,770,604, 1988.

[52] Larry Bachus and Angel Custodio, *Know and Understand Centrifugal Pumps*. Kidlington, Oxford: Elsevier Advanced Technology, 2003.

[53] Mustafa Golcu and Yasar Pancar, "Investigation of Performance Characteristics in a Pump Impeller with Low Blade Discharge Angle," *World Pump*, pp. 32 - 39, Sept 2005.

[54] Wen-Guang Li, "Effect of Viscosity of Fluid on Centrifugal Pump Performance and Flow Pattern in the Impeller," *International Journal of Heat and Fluid Flow*, pp. 207 - 212, 1999.

[55] B V Ukhin, "Effect of the Quantity and Shap of Impeller Blades on Dredge Pump Perameters," *Power Technology and Engineering* , pp. 168 - 172, 2002.

[56] B K Gandhi, S N Singh, and V Seshadri, "Effect of Speed on the Performance Characteristics of a Centrifugal Slurry Pump," *Journal of Hydraulic Engineering*, pp. 225 - 233, 2002.

[57] A N Sherstyuk and R A Erofeev, "Determination of the Theoretical Head of a Centrifugal Pump or Compressor Stage," *Chemical and Petroleum Engineering*, vol. 37, pp. 154 - 157, 2001.

[58] Reijo Karvinen, Reijo Koivikko, and Sami Virtanen, "Design Procedure for Hight-Efficiency Pumps," Dusseldorf, 2008.

[59] Khin Cho Thin, Mya Mya Khaing, and Khin Maung Aye, "Design and Performance Analysis of Centrifugal Pump," *World Academy of Science, Engineering and Thechnology* , no. 46, pp. 422 - 429, 2008.

[60] Khin Maung Htwe, "Design and Construction of Single Stage Centrifugal Pump (Impeller)," in *International Conference on Sustainable Development: Issues and Prospects for the GMS*, 2008, pp. 1 - 7.

[61] Xuelin Tang and Fujun Wang, "An Improved Large Eddy Simulation of Two-phase Flows in a Pump Impeller," *Acta Mech Sin*, pp. 635 - 643, 2007.

[62] Timperi Et al, 4,877,368, 1989.

[63] Austin Whillier, "Pump Efficiency Determintion from Temperture Measurments," 1967.

[64] D Rajenthirakumar and K A Jagadeesh, "Analysis of Interaction Between Geometry and Efficiency of Impeller Pump using Rapid Prototyping," *Int J Adv Manuf Technol*, pp. 890 - 899, 2009.

Appendices

Appendix A (Blade Generator Program)

Blade Generator Program: Parabolic β Distribution

Mean LE Blade Angle: $\beta_1 := 80$ deg

Mean TE Blade Angle: $\beta_2 := 60$ deg

Inlet Radius: $r_1 := 50$ mm

Outlet Radius: $r_2 := 178$ mm

Mid Blade Angle:

$\beta_m :=$ 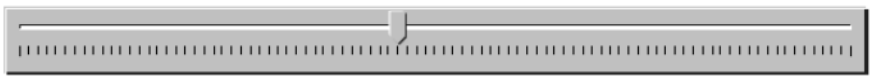 $\beta_m = 41$

Location of Mid Blade Angle % between r1 and r2:

$r\% :=$  $r\% = 60$

$$r_m := \frac{r_2 - r_1}{100}\cdot(r\%) + r_1 \qquad r_m = 126.8$$

Given $\quad a := 1 \quad b := 1 \quad c := 1$

$$\beta_1 = a\cdot r_1^{\,2} + b\cdot r_1 + c \qquad \beta_2 = a\cdot r_2^{\,2} + b\cdot r_2 + c \qquad \beta_m = a\cdot r_m^{\,2} + b\cdot r_m + c$$

$$\begin{pmatrix} a \\ b \\ c \end{pmatrix} := \mathrm{Find}(a,b,c) = \begin{pmatrix} 6.866\times 10^{-3} \\ -1.722 \\ 148.924 \end{pmatrix} \qquad \beta(r) := \left(a\cdot r^2 + b\cdot r + c\right)\cdot \mathrm{deg}$$

$$x := r_1, (r_1 + 0.5) .. r_2 \qquad \phi := 0, \frac{\pi}{180} .. 2\pi$$

$$\theta(r) := -1\cdot\left(\int_{r_1}^{r} \frac{1}{r\cdot\tan(\beta(r))}\,dr\right)$$

Wrap Angle: $-\theta(r_2) = 55.45\cdot\mathrm{deg}$

$$\mathrm{leng} := \int_{r_1}^{r_2} \left[1 + \left[r\cdot\frac{d}{dr}(\theta(r))\right]^2\right]^{0.5} dr$$

Blade Length: $\mathrm{leng} = 169.423$ mm

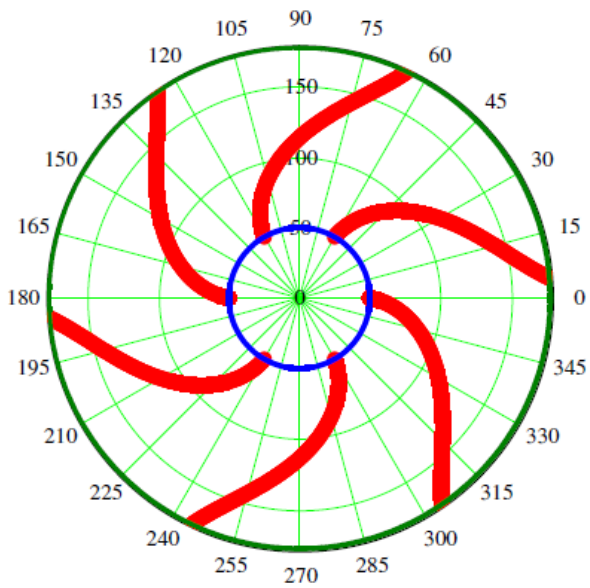

$\beta_1 = 80$ $\beta_2 = 60$ $\beta_m = 41$

$\theta(r_2) = -55.45\,\text{deg}$ leng = 169.423 mm

Blade-to-Blade Plot

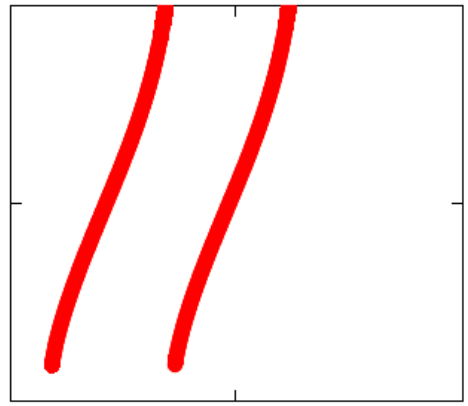

Blade Angle Plot

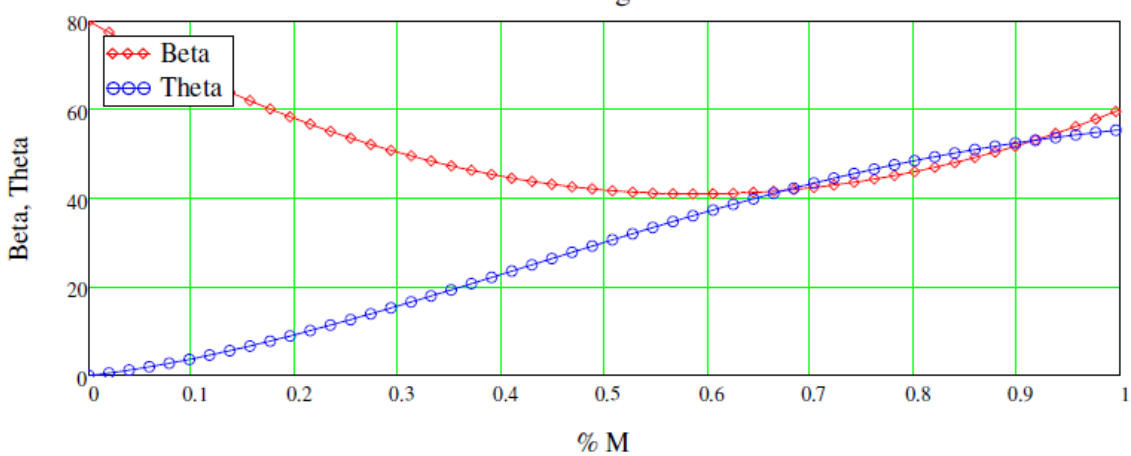

Appendix B (Redesign Model Program)

Redesign Impeller Model

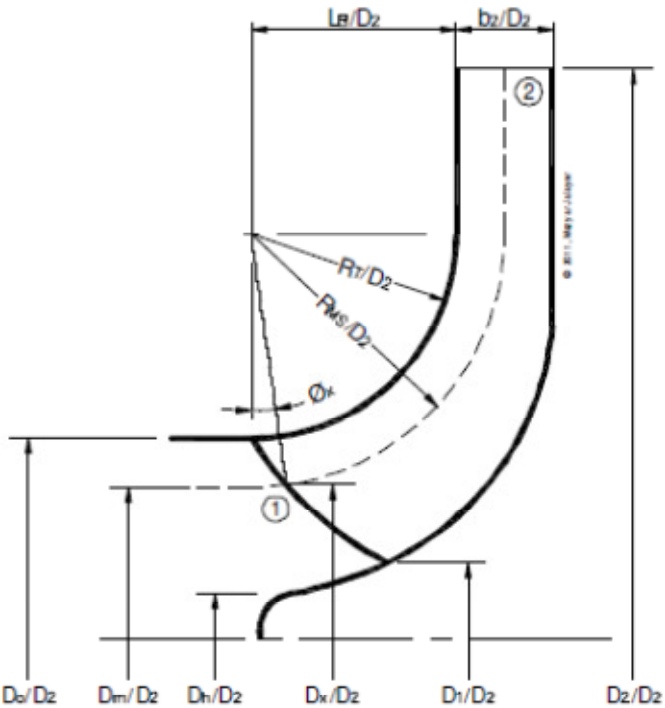

Fixed Geometric Parameters	
Impeller Outlet Diameter	D_2
Hub Diameter	D_h
Outlet Blade Width	b_2
Impeller Eye Diameter	D_0
Peripheral Radius Of Curvature	R_T
Design Duty	
Machine Design Flow	Q
Machine Design Speed	n
Volumetric Efficiency	η_v

Hub Diameter: $D_h := 1.137in$

Impeller eye diameter: $D_0 := 4.942in$

Impeller outlet diameter: $D_2 := 14in$

Impeller inlet diameter: $D_1 := 1.893in$

Mean diameter: $D_m := \frac{D_0 + D_h}{2} = 3.04 \cdot in$

Outlet blade width: $b_2 := 1.19in$

Peripheral section radius of curvature: $R_T := 2.515in$

Radius of curvature of the mean streamline: $R_{MS} := 0.5b_2 + R_T \quad R_{MS} = 3.11 \cdot in$

Hub to tip ratio: $r := \frac{D_h}{D_0} = 0.23$

Edge of mean Streamline (location of LE): $\theta_x := 7.8deg$

Hub/shroud out let angle (90 deg = radial Impeller) $\theta := 90deg$

Machine design capacity: $Q := 400\frac{gal}{min}$

Machine speed: $n := 1150rpm$

Outlet Peripheral velocity: $u_2 := \frac{n \cdot D_2}{2} = 21.412\frac{m}{s}$

Assumed volumetric efficiency: $\eta_v := 95\%$

Outlet area: $A_2 := \pi \cdot b_2 \cdot D_2$

Impeller eye area: $A_0 := \frac{\pi \cdot D_0^2}{4}\left[1 - \left(\frac{D_h}{D_0}\right)^2\right]$

Outlet flow coefficient: $\phi_2 := \frac{Q}{\eta_v \cdot A_2 \cdot u_2} = 0.037$

Streamline Plot Function:

$$x := \frac{-D_2}{2}, \frac{-D_2}{2} + 1mm .. -R_{MS} \cdot \sin(\theta_x)$$

$$f_1(x) := \sqrt{R_{MS}^2 - \left(x + R_{MS} + \frac{D_m}{2}\right)^2}$$

$$aa := -\frac{1}{\tan(\theta)}$$

$$bb := aa \cdot \left(R_{MS} + \frac{D_m}{2} - R_{MS} \cdot \cos(\theta)\right) + R_{MS} \cdot \sin(\theta)$$

$$f_2(x) := aa \cdot x + bb$$

$$rm(x) := if\left[x < \frac{D_m}{2} \wedge x > \left(R_{MS} \cdot \cos(\theta) - \frac{D_m}{2} - R_{MS}\right), f_1(x), f_2(x)\right]$$

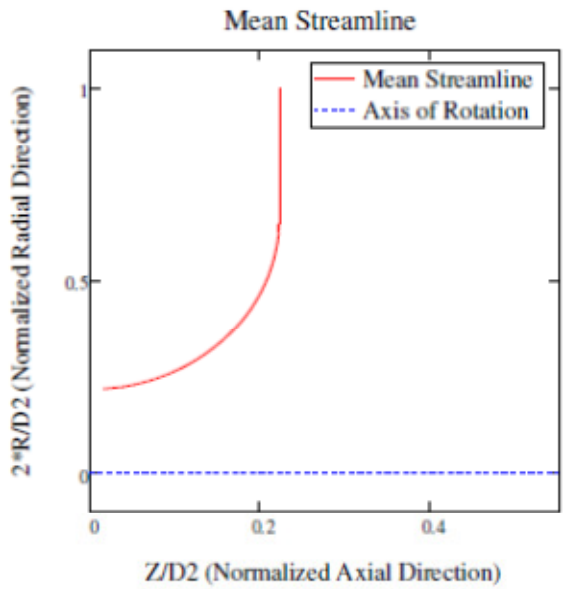

Leading edge dimensionless diameter:

$$y(\theta_x) := \left[\frac{2\cdot R_{MS}}{D_2} + \sqrt{2\cdot\frac{b_2\cdot A_0\cdot\left(1+r^2\right)}{D_2\cdot A_2\cdot\left(1-r^2\right)}} - 2\cdot\frac{R_{MS}}{D_2}\cdot\cos(\theta_x)\right]$$

Variable area ratio:

$$x(\theta_x) := \frac{A_0}{A_2} + \frac{\left(1-\frac{A_0}{A_2}\right)\left(\frac{R_T}{D_2}+\frac{D_2}{2\cdot D_2}\right)\cdot\theta_x}{\frac{0.5}{\sin(\theta)} - \frac{0.5}{\sin(\theta)}\cdot\sqrt{2\cdot\frac{b_2\cdot A_0\cdot\left(1+r^2\right)}{D_2\cdot A_2\cdot\left(1-r^2\right)}} + \left(\frac{R_T}{D_2}+\frac{b_2}{2\cdot D_2}\right)\cdot(\theta+1-\cos(\theta))}$$

Blade thickness (dependent of structural integrity of the material)

$$t_x := 0.25in$$

Number of blades

$$z := 2..6$$

$$a(z) := \frac{t_x\cdot z}{\pi\cdot D_2}$$

Flow Entry Angle:

$$\beta_{xf}(\theta_x, z) := \operatorname{asin}\left(\frac{a(z)\cdot x(\theta_x)^2\cdot y(\theta_x) + \phi_2\cdot\sqrt{x(\theta_x)^2\cdot y(\theta_x)^2 + \phi_2^{\,2} - a(z)^2\cdot x(\theta_x)^2}}{x(\theta_x)^2\cdot y(\theta_x)^2 + \phi_2^{\,2}}\right)$$

$\beta_{xf}(\theta_x, z) =$

21.319
22.504
23.691
24.88
26.071

$\cdot deg$

Blade Entry Angle: $\beta_{xB}(\theta_x, z) := \operatorname{atan}\left(\frac{\tan(\beta_{xf}(\theta_x, z))}{1.06}\right)$

$\beta_{xB}(\theta_x, z) =$

20.212
21.348
22.487
23.63
24.777

$\cdot deg$

Blockage factor at entry: $\xi_1(\theta_x, z) := \frac{\sin(\beta_{xB}(\theta_x, z))}{\sin(\beta_{xB}(\theta_x, z)) - 3\,a(z)}$

Blockage factor at exit: $\xi_2(\beta_{2B}, z) := \frac{\sin(\beta_{2B})}{\sin(\beta_{2B}) - 3\,a(z)}$

Busemann Data: Busemann :=
...\Busemanns Slip.xls

Busemann Slip Coefficient: $h_o(\beta_{2B}, z) := \text{vlookup}\left(\frac{\beta_{2B}}{deg}, \text{Busemann}, z - 1\right)_{0,0}$ Model 1.

$h_o(\beta_{2B}, z) := 1 - \frac{\sin(\beta_{2B})^{0.5}}{z^{0.7}}$ Model 2.

Slip factor: $k(\beta_{2B}, z) := \frac{h_o(\beta_{2B}, z) - \xi_2(\beta_{2B}, z)\cdot\phi_2\cdot\cot(\beta_{2B})}{1 - \xi_2(\beta_{2B}, z)\cdot\phi_2\cdot\cot(\beta_{2B})}$

Average Relative Flow Direction: $\beta_{avg}(\theta_x, \beta_{2B}, z) := \operatorname{atan}\left[\frac{\phi_2\cdot\left(\xi_2(\beta_{2B}, z) + \frac{\xi_1(\theta_x, z)}{x(\theta_x)}\right)}{1 - h_o(\beta_{2B}, z) + \phi_2\cdot\xi_2(\beta_{2B}, z)\cdot\cot(\beta_{2B}) + y(\theta_x)}\right]$

Variable Length of Radial Plane: $h_x(\theta_x) := \left[\frac{0.5}{\sin(\theta)} + \left(\frac{R_T}{D_2} + \frac{b_2}{2D_2}\right)\left(\theta - \theta_x - \frac{1 - \cos(\theta)}{\sin(\theta)}\right) - \frac{0.5}{\sin(\theta)}\cdot\sqrt{2\cdot\frac{b_2\cdot A_0\cdot(1 + r^2)}{D_2\cdot A_2\cdot(1 - r^2)}}\right]\cdot D_2$

Blade Chord Angle: $\beta_{CH}(\theta_x, z, \beta_{2B}) := \frac{\beta_{2B} + \beta_{xB}(\theta_x, z)}{2}$

Vane Length: $leng(\theta_x, z, \beta_{2B}) := h_x(\theta_x)\cdot\frac{1}{\sin(\beta_{CH}(\theta_x, z, \beta_{2B}))}$

Mean vane pitch:

$$t_m(\theta_x, z) := D_2 \cdot \frac{(1 + y(\theta_x))}{2 \cdot z}$$

$t_m(\theta_x, z) =$

4.411
2.941
2.205
1.764
1.47

$\cdot in$

Solidity Factor:

$$\sigma(\theta_x, z, \beta_{2B}) := \frac{leng(\theta_x, z, \beta_{2B})}{t_m(\theta_x, z)}$$

Weinig's Correction Factor:

$$AA(\theta_x, z, \beta_{2B}) := \frac{2}{\pi} \cdot \frac{1}{\sigma(\theta_x, z, \beta_{2B})} \cdot \frac{1}{\sin(\beta_{CH}(\theta_x, z, \beta_{2B}))}$$

Lift Coefficient:

$$C_{LA}(\theta_x, z, \beta_{2B}) := \frac{4\pi}{\frac{leng(\theta_x, z, \beta_{2B})}{D_2} \cdot 2 \cdot AA(\theta_x, z, \beta_{2B})} \cdot \sin(\beta_{CH}(\theta_x, z, \beta_{2B})) \cdot k(\beta_{2B}, z) \cdot \frac{y(\theta_x) - \xi_2(\theta_x, z) \cdot \phi_2 \cdot \cot(\beta_{2B})}{\phi_2 \cdot \left(\frac{\xi_1(\theta_x, z)}{x(\theta_x)} + \xi_2(\theta_x, z)\right)}$$

Zero Lift:

$$C_{Li}(\theta_x, z, \beta_{2B}) := \frac{25}{8} \cdot \tan\left(\frac{\beta_{2B} - \beta_{xB}(\theta_x, z)}{2}\right)$$

Angle of Attack Isolated Foil:

$$\alpha_{o.}(\theta_x, z, \beta_{2B}) := \frac{(C_{Li}(\theta_x, z, \beta_{2B}) - C_{LA}(\theta_x, z, \beta_{2B}))}{0.098}$$

Thickness Correction Factor:

$$\Delta\alpha(\theta_x, z, \beta_{2B}) := 3.9 \cdot a(z) \cdot \frac{180}{\pi}\left(\frac{1}{1 + x(\theta_x)}\right)\cos(\beta_{CH}(\theta_x, z, \beta_{2B}))$$

Angle of Attack Required:

$$\alpha(\theta_x, z, \beta_{2B}) := \alpha_{o.}(\theta_x, z, \beta_{2B}) + \Delta\alpha(\theta_x, z, \beta_{2B})$$

Incidence Angle:

$$i(\theta_x, z, \beta_{2B}) := (\beta_{CH}(\theta_x, z, \beta_{2B}) - \beta_{avg}(\theta_x, \beta_{2B}, z))$$

Diffusion Angle:

$$\alpha_d(\theta_x, z, \beta_{2B}) := \operatorname{atan}\left[\frac{\left(1 - x(\theta_x)^{0.5}\right)\left(\frac{b_2}{D_2}\right)^{0.5}}{\frac{leng(\theta_x, z, \beta_{2B})}{D_2}}\right]$$

Redesign Model Solver Parameters and Limiting Conditions:

Given

Assume $\beta_{2B} := 20deg \qquad \theta_x := 8deg$

Residual: $i(\theta_x, z, \beta_{2B}) - \alpha(\theta_x, z, \beta_{2B}) = |0.000001|$

Hydrodynamic lift limit: $C_{LA}(\theta_x, z, \beta_{2B}) \le 0.600$

Diffusion Angle limit: $\dfrac{\alpha_d(\theta_x, z, \beta_{2B})}{2} \le 6deg$

Blade Camber Limit $\left|\beta_{2B} - \beta_{xB}(\theta_x, z)\right| \le 8$

$\beta_{2B}(z) := \mathrm{Find}(\beta_{2B})$

$z =$	$\beta_{2B}(z) =$	$\beta_{xB}(\theta_x, z) =$	$\dfrac{\alpha_d(\theta_x, z, \beta_{2B}(z))}{2}$	$C_{LA}(\theta_x, z, \beta_{2B}(z))$	$\lvert\beta_{2B}(z) - \beta_{xB}(\theta_x, z)\rvert$	$= i(\theta_x, z, \beta_{2B}(z)) - \alpha(\theta_x, z, \beta_{2B}(z))$
2	10.1 ·deg	20.1 ·deg	1.665 ·deg	-0.111	9.993 ·deg	$10 \cdot 10^{-7}$
3	12.6	21.3	1.857	$8.145 \cdot 10^{-3}$	8.67	$10 \cdot 10^{-7}$
4	15.8	22.4	2.083	0.143	6.649	$10 \cdot 10^{-7}$
5	20.6	23.5	2.392	0.316	2.983	$10 \cdot 10^{-7}$
6	29	24.7	2.871	0.571	4.267	$1 \cdot 10^{-6}$

Hydraulic Diameter At Leading Edge:

$$D_{H1}(z) := \frac{\dfrac{2b_2}{D_2} \cdot x(\theta_x)\, y(\theta_x) \sin\left(\beta_{xB}(\theta_x, z) - a(z)\right)}{\dfrac{b_2}{\pi \cdot D_2}\, a(z) \cdot x(\theta_x) z + y(\theta_x)^2 \sin\left(\beta_{xB}(\theta_x, z) - a(z) \cdot y(\theta_x)\right)} \cdot D_2$$

Hydraulic Diameter At Trailing Edge:

$$D_{H2}(z) := \frac{\dfrac{2b_2}{D_2} \sin\left(\beta_{2B}(z) - 3\,a(z)\right)}{\dfrac{b_2 \cdot z}{D_2 \cdot \pi} + \sin\left(\beta_{2B}(z)\right) - 3\,a(z)} \cdot D_2$$

Mean Value of Hydraulic Diameter:

$$D_{Havg}(z) := \left(\frac{\pi \dfrac{b_2}{D_2}}{2z}\right)^{0.5} \left[\frac{x(\theta_x)}{y(\theta_x)}\left(y(\theta_x) \cdot \sin\left(\beta_{xB}(\theta_x, z)\right) - a(z)\right) + \sin\left(\beta_{2B}(z)\right) - 3\,a(z)\right]^{-0.5} \cdot D_2$$

Equivalent Hydraulic Diameter of Flow Passage:

$$D_{HEQ}(z) := \frac{D_{H1}(z) + D_{H2}(z) + 2\,D_{Havg}(z)}{4}$$

Average Relative Velocity:

$$w_{avg}(z) := \left[\frac{\phi_2}{4}\left(\frac{\xi_1(\theta_x, z)}{x(\theta_x)} + \xi_2(\beta_{2B}(z), z)\right)^2 + \frac{\left(\xi_2(\beta_{2B}(z), z) \cdot \phi_2 \cdot \cot\left(\beta_{2B}(z)\right) + 1 - h_o(\beta_{2B}(z), z) + y(\theta_x)\right)}{4}\right]^{0.5} \cdot u_2$$

$$\nu := 1\cdot 10^{-6}\frac{m^2}{s}$$

Flow Reynolds Number: $$Re(z) := \frac{w_{avg}(z)\cdot D_{HEQ}(z)}{\nu}$$

Passage Roughness: $$\Delta\varepsilon(z) := \frac{0.00005m}{D_{HEQ}(z)}$$

Friction Factor: $$f(z) := 0.25\left(\log\left(\frac{4.52}{Re(z)}\log\left(\frac{Re(z)}{7}\right) + \frac{\Delta\varepsilon(z)}{3.7}\right)\right)^{-2}$$

Outlet head coefficient: $$\psi_2(z) := h_o\left(\beta_{2B}(z), z\right) - \xi_2\left(\beta_{2B}(z), z\right)\cdot\phi_2\cdot\cot\left(\beta_{2B}(z)\right)$$

Friction loss Impeller: $$h_{impf}(z) := \frac{f(z)\cdot leng\left(\theta_x, z, \beta_{2B}(z)\right)}{2\cdot\psi_2(z)\cdot D_{HEQ}(z)}\left(\frac{w_{avg}(z)}{u_2}\right)^2$$

Jet- Wake Losses: $$h_{dw}(z) := 0.5\frac{\left[\left(\xi_2\left(\beta_{2B}(z), z\right) - 1\right)\cdot\xi_2\left(\beta_{2B}(z), z\right)\cdot\phi_2\right]^2}{\psi_2(z)}$$

Blade Camber: $$mp(z) := \frac{1}{4}\tan\left(\beta_{2B}(z) - \beta_{CH}\left(\theta_x, z, \beta_{2B}(z)\right)\right)$$

Position of Max Camber: $$p_c := 0.5$$

Imperial Data for NACA 65:

$d_2 := 0.127$ $\quad d_3(z) := 0.2\,mp(z)$ $\quad d_4 := 0.0086$ $\quad C_{Lmax} := 1.1$

$$C_{Lopt}(z) := mp(z)\cdot(109 - 14.1\log(Re(z)))\left(1 - 4\cdot\frac{t_x}{leng\left(\theta_x, z, \beta_{2B}(z)\right)}\right)$$

$$X(z) := \frac{C_{LA}\left(\theta_x, z, \beta_{2B}(z)\right) - C_{Lopt}(z)}{C_{Lmax} - C_{Lopt}(z)}$$

$$C_{Dmin}(z) := \left[0.0052 + 0.023\cdot mp(z)\left(1 + mp(z)^2\right) + 0.07\left(\frac{t_x}{leng\left(\theta_x, z, \beta_{2B}(z)\right)}\right)^2 + 1.67\,mp(z)^2\cdot p_c^3\right]\left(\frac{5\cdot 10^6}{Re(z)}\right)^{0.11}$$

Drag Coefficient:

$$C_d(z) := C_{Dmin}(z) + d_2\cdot X(z)^2 + d_3(z)\cdot X(z)^3 + d_4\cdot X(z)^4$$

Drag Losses: $$h_{dD}(z) := C_d(z)\cdot\sigma\left(\theta_x, z, \beta_{2B}(z)\right)\left(\frac{w_{avg}(z)}{u_2}\right)^2\frac{1}{\beta_{avg}\left(\theta_x, \beta_{2B}(z), z\right)}\cdot\frac{1}{2\cdot\psi_2(z)}$$

Impeller Hydraulic Losses: $$\eta_h(z) := 1 - \left(h_{impf}(z) + h_{dw}(z) + h_{dD}(z)\right)$$

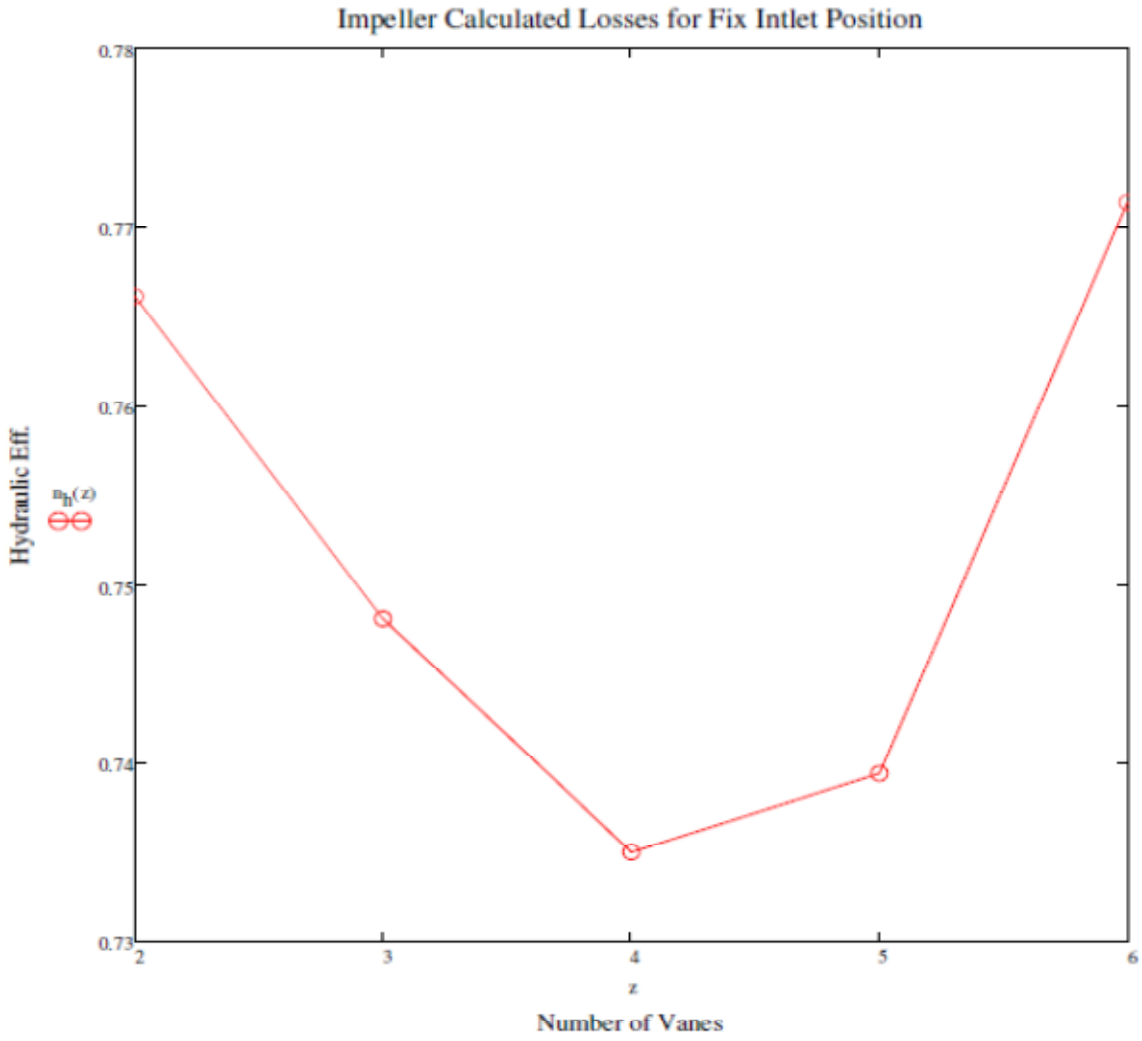
Impeller Calculated Losses for Fix Intlet Position
0.78
0.77
0.76
0.75
0.74
0.73
Hydraulic Eff.
$\eta_h(z)$
2
3
4
5
6
z
Number of Vanes

$z := 2$

$\beta_1 := \beta_{xB}(\theta_x, z) = 20.131 \cdot deg$

$\beta_2 := \beta_{2B}(z) = 10.138 \cdot deg$

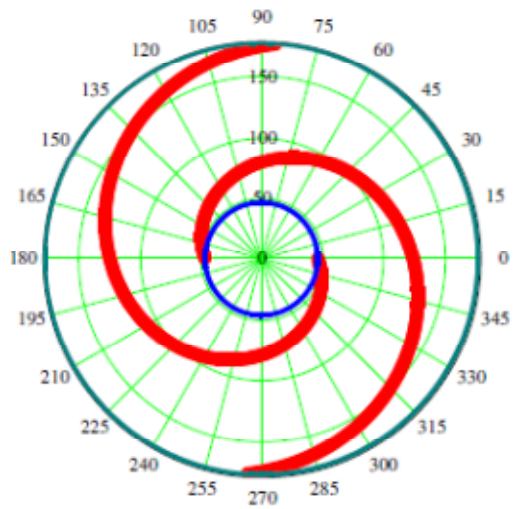

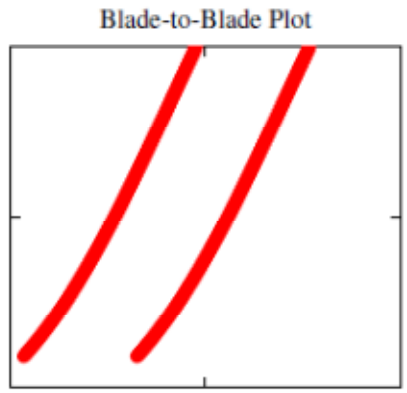

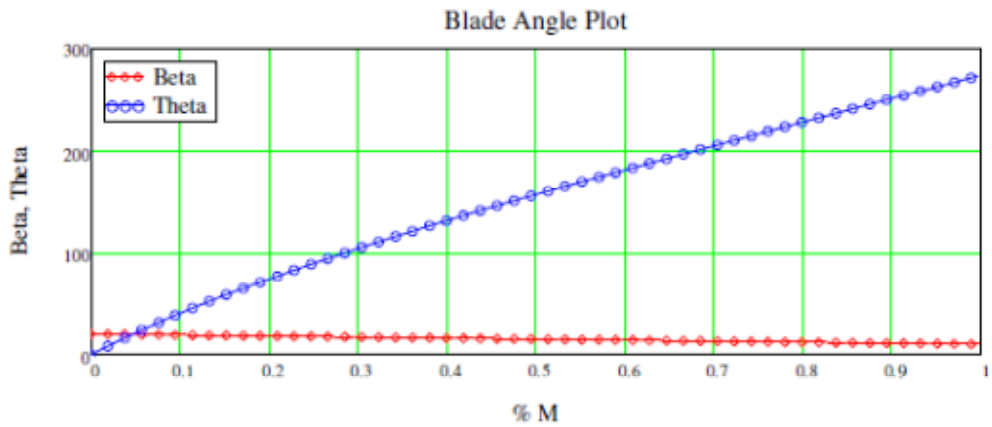

$z := 3$

$\beta_1 := \beta_{xB}(\theta_x, z) = 21.266 \cdot deg$

$\beta_2 := \beta_{2B}(z) = 12.596 \cdot deg$

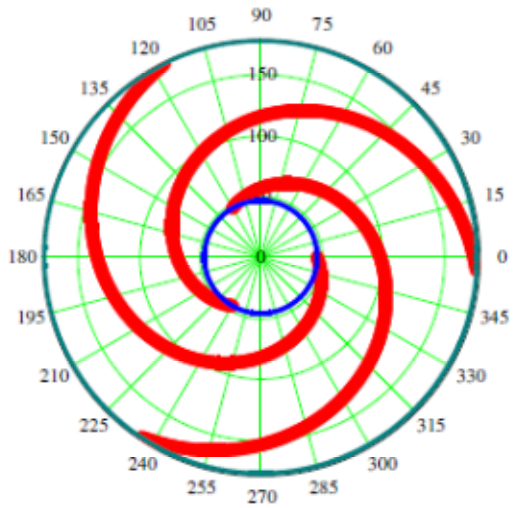

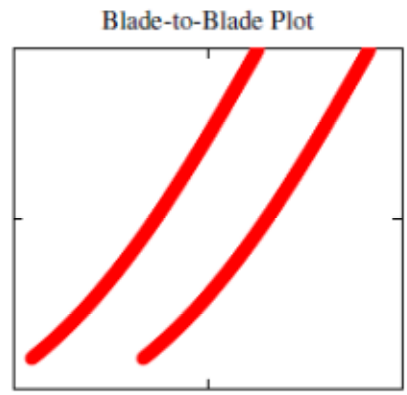

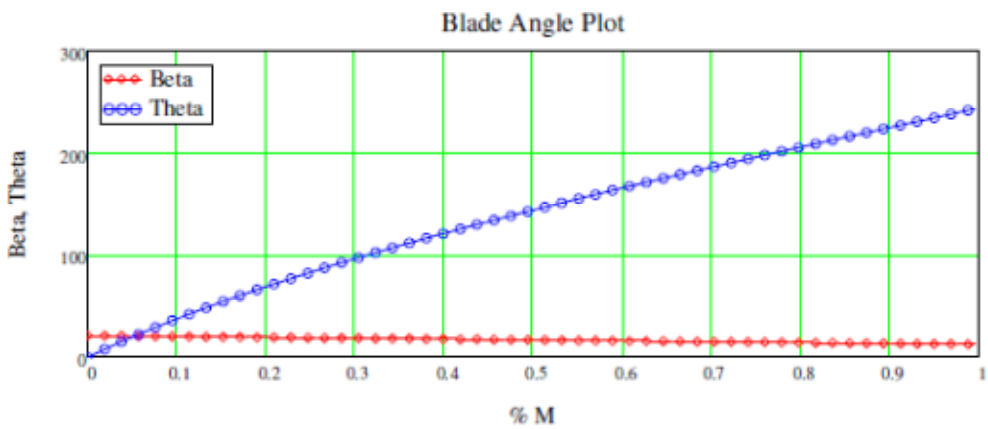

$z := 4$

$\beta_1 := \beta_{xB}(\theta_x, z) = 22.404 \cdot deg$

$\beta_2 := \beta_{2B}(z) = 15.756 \cdot deg$

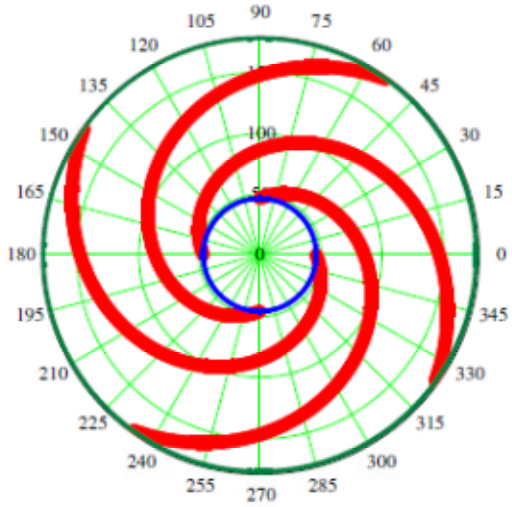

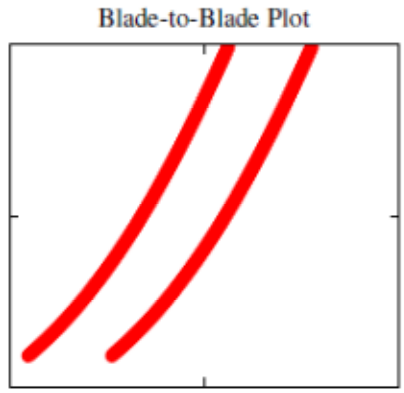

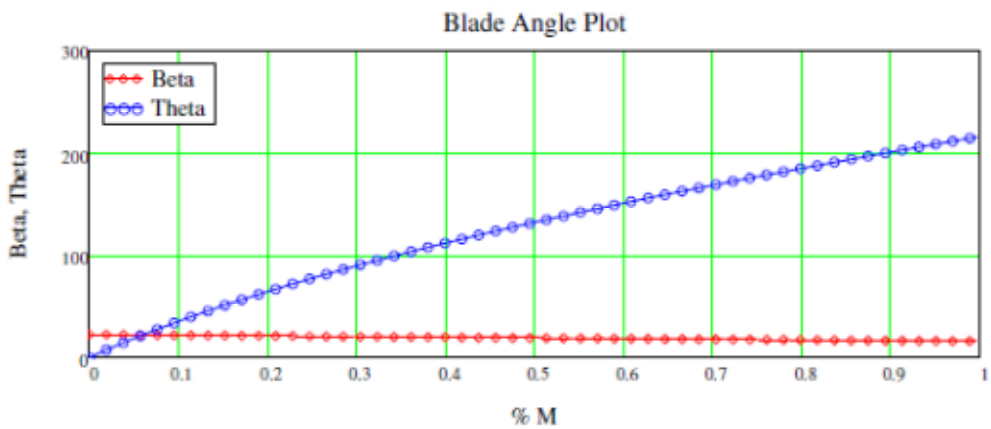

$z := 5$

$\beta_1 := \beta_{xB}(\theta_x, z) = 23.547 \cdot deg$

$\beta_2 := \beta_{2B}(z) = 20.564 \cdot deg$

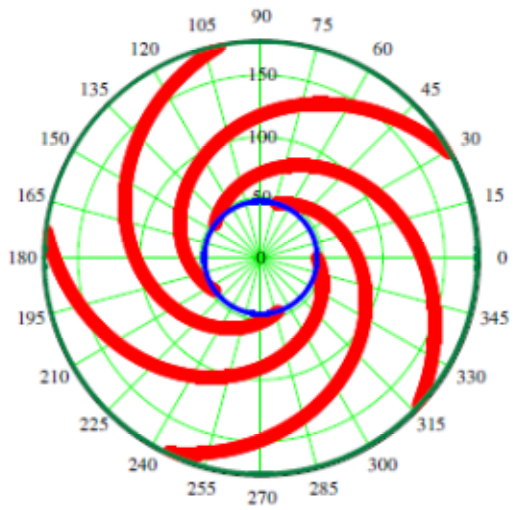

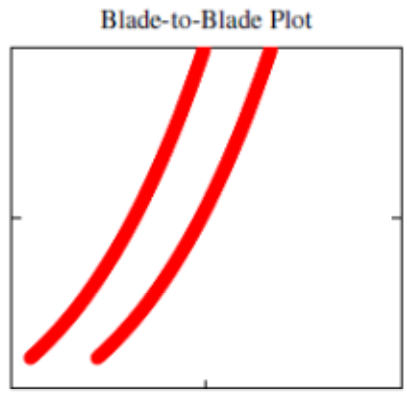

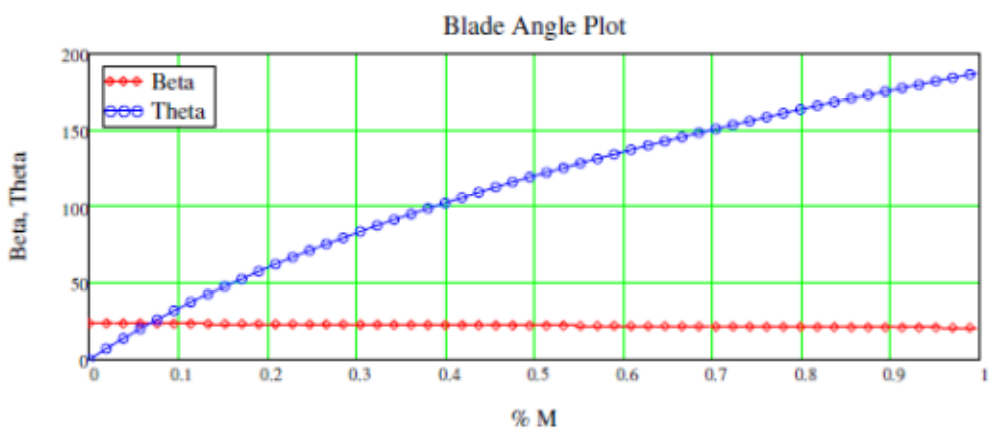

$z := 6$

$\beta_1 := \beta_{xB}(\theta_x, z) = 24.693 \cdot deg$

$\beta_2 := \beta_{2B}(z) = 28.96 \cdot deg$

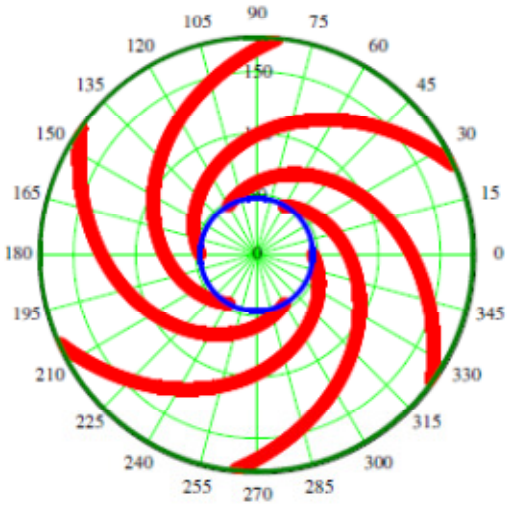

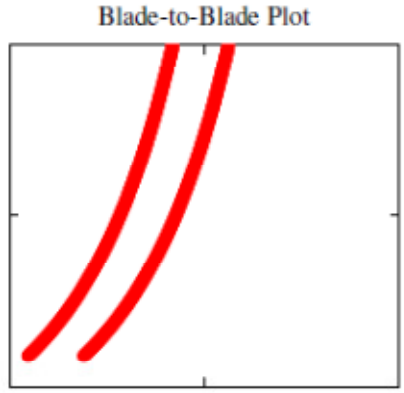

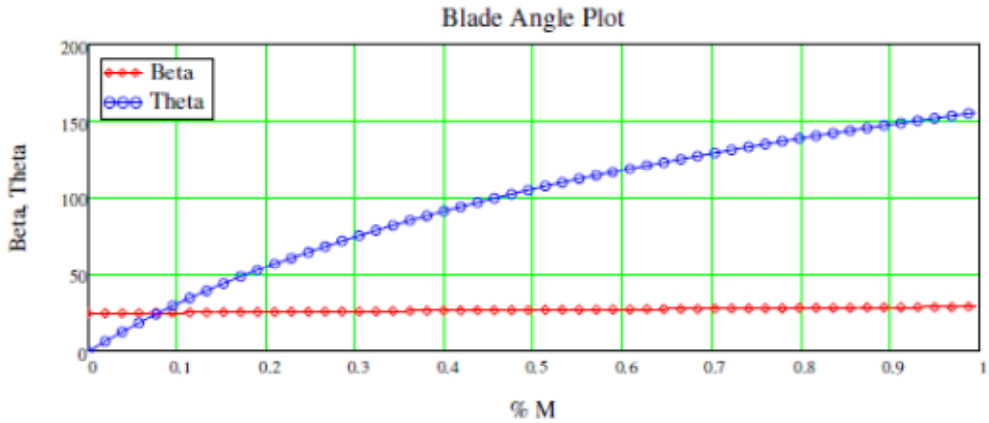

Appendix C (Impeller Insert Prototyping Drawing)

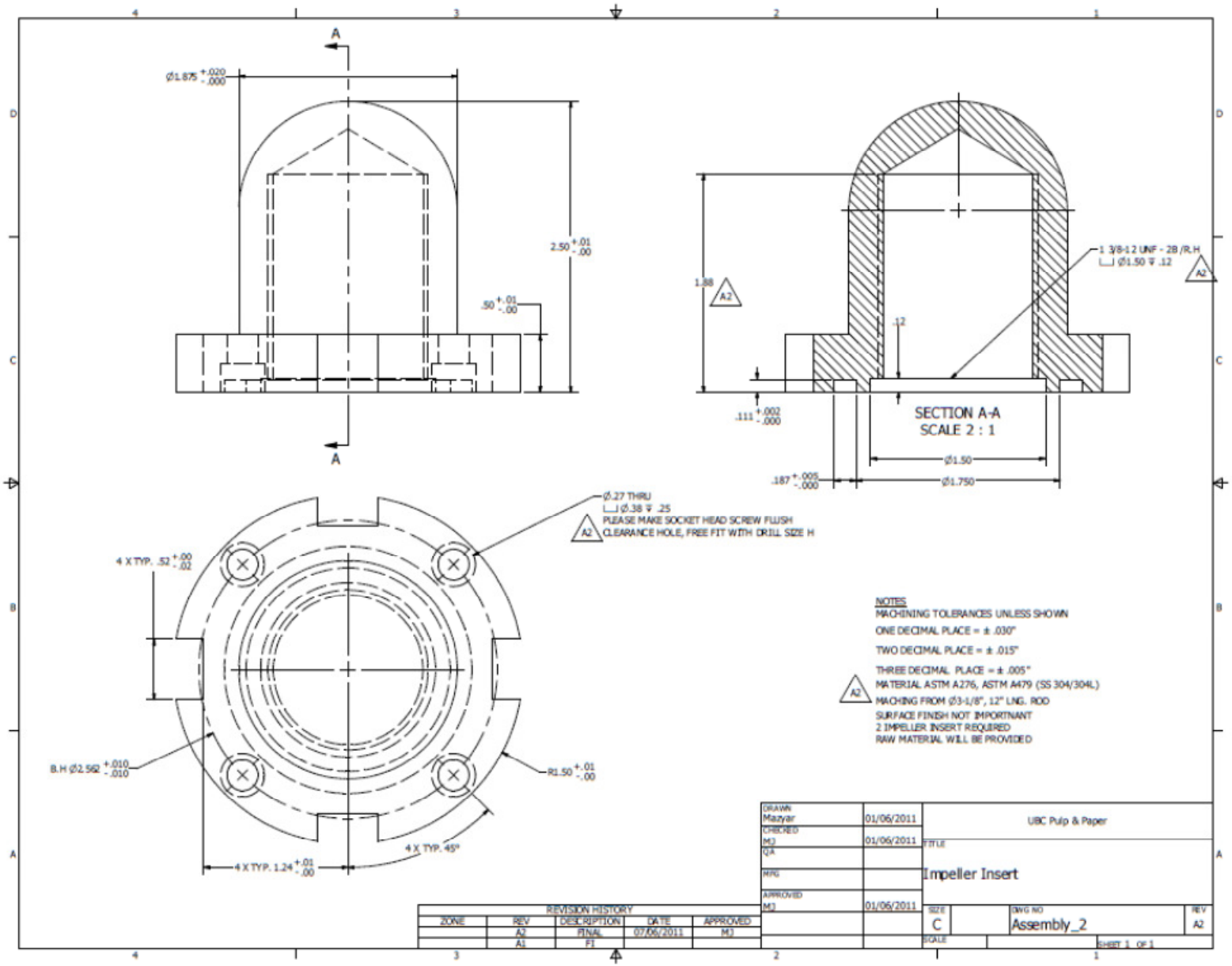

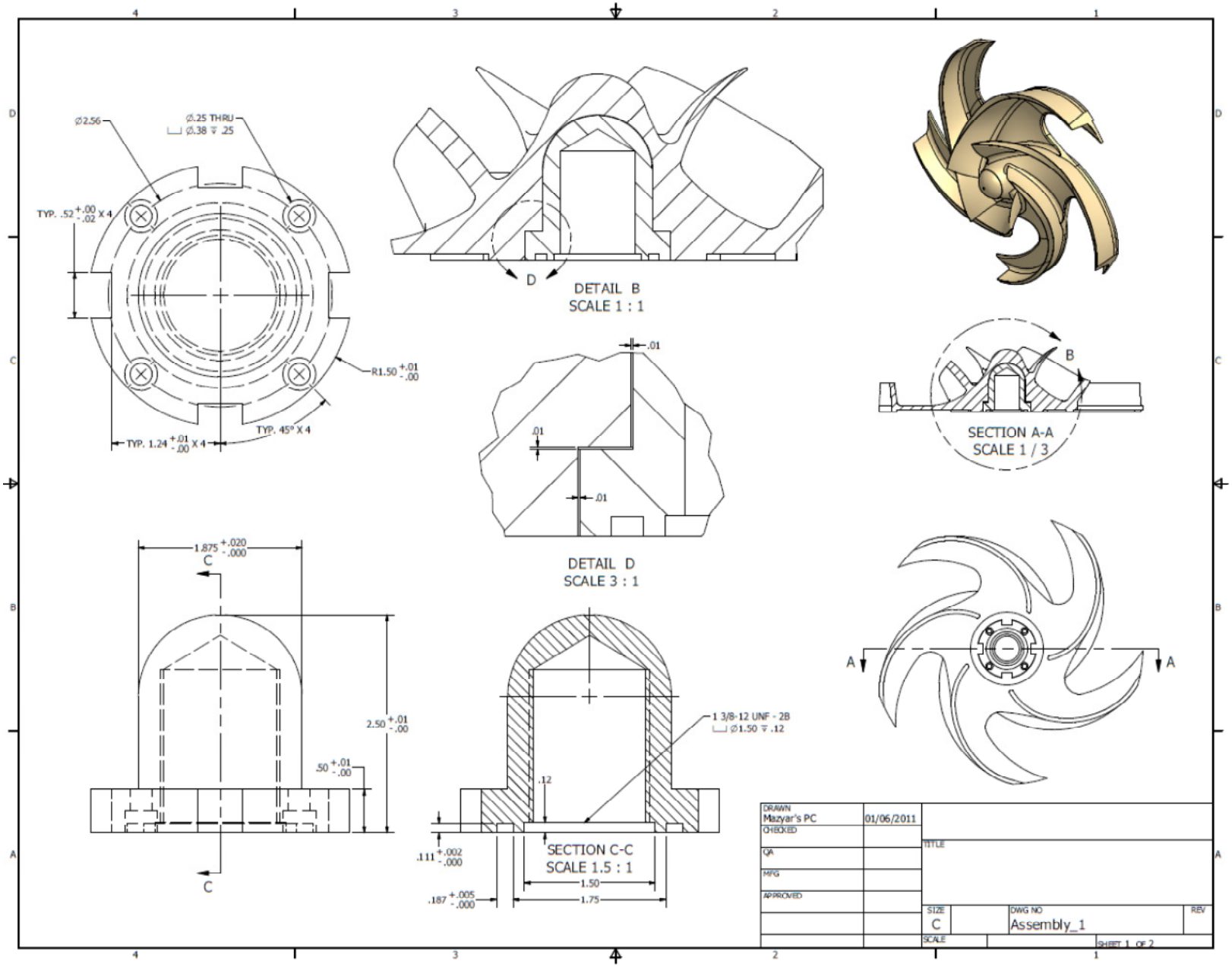
Ø2.56
Ø.25 THRU
Ø.38 ↧ .25
TYP. .52 +.00 -.02 X 4
R1.50 +.01 -.00
TYP. 45° X 4
TYP. 1.24 +.01 -.00 X 4
DETAIL B
SCALE 1 : 1
D
.01
.01
.01
DETAIL D
SCALE 3 : 1
B
SECTION A-A
SCALE 1 / 3
A
A
1.875 +.020 -.000
C
C
2.50 +.01 -.00
.50 +.01 -.00
1 3/8-12 UNF - 2B
Ø1.50 ↧ .12
.12
.111 +.002 -.000
.187 +.005 -.000
SECTION C-C
SCALE 1.5 : 1
1.50
1.75
DRAWN
Mazyar's PC
01/06/2011
CHECKED
QA
MFG
APPROVED
TITLE
SIZE
C
DWG NO
Assembly_1
REV
SCALE
SHEET 1 OF 2

Appendix D (Pipe Spool for Yatesmeter Trial)